Universidade de Aveiro Departamento de Física
2011

Carlos Davide da Rocha Azevedo

Hole-type gaseous detectors for medical imaging and HEP experiments

Universidade de Aveiro Departamento de Física
2011

Carlos Davide da Rocha Azevedo

Hole-type gaseous detectors for medical imaging and HEP experiments

Dissertação apresentada à Universidade de Aveiro para cumprimento dos requisitos necessários à obtenção do grau de Doutor em Engenharia Física, realizada sob a orientação científica do Doutor João Filipe Calapez de Albuquerque Veloso, Professor Auxiliar do Departamento de Física da Universidade de Aveiro

Apoio financeiro da FCT e do FSE no âmbito do III Quadro Comunitário de Apoio (Bolsa de Doutoramento SFRH/BD/35979/2007)

Gostaria de dedicar este trabalho a todos aqueles que me acompanharam nesta etapa que agora termina. Porém vou destacar alguns daqueles que mais me marcaram neste período da minha vida.
Começo, obviamente por dedicar este trabalho ao Afonso Davide, ao Eduardo e à Patrícia: é em relação a vocês que mais dificuldades tenho em escrever a dedicatória, pois efectivamente não encontro palavras que reflictam o meu apreço.
De seguida gostaria de dedicar este trabalho a duas mulheres que admiro imenso pela enorme coragem e pela forma como enfrentam a vida: a minha mãe e a minha irmã.
Faço uma dedicatória especial para o meu pai.
Dedico também aos meus sobrinhos: Ana Rita, Ricardo Jorge e Ana Carolina, não esquecendo o meu cunhado, Jorge.
Dedico a toda a minha família, com uma atenção especial aos meus avós.
Finalmente dedico este trabalho a todos os meus amigos.

o júri

presidente

Prof. Doutor Artur Manuel Soares da Silva
professor catedrático do Departamento de Química da Universidade de Aveiro

Prof. Doutor Joaquim Marques Ferreira dos Santos
professor catedrático da Faculdade deCiências e Tecnologia da Universidade de Coimbra

Prof. Doutora Maria da Conceição Abreu e Silva
professora catedrática aposentada da Universidade do Algarve

Prof. Doutora Maria Luísa Carvalho Leonardo
professora associada da Faculdade de Ciências da Universidade de Lisboa

Prof. Doutor João Filipe Calapez de Albuquerque Veloso
professor auxiliar do Departamento de Física da Universidade de Aveiro

Doutor Daniel dos Santos Covita
Investigador do I3N, Aveiro

agradecimentos

Gostaria de enviar um agradecimento especial ao meu orientador: Prof João Veloso. Sem a sua ajuda e orientação este trabalho não teria sido possível. Um grande obrigado por esta oportunidade e pela sua dedicação na minha formação.

Quero agradecer à Fundação para a Ciência e a Tecnologia pela Bolsa de Doutoramento que me atribuiu e à Universidade de Aveiro, nomeadamente ao Departamento de Física, pela condições que me proporcionou.

Um obrigado especial aos meus colegas de laboratório carinhosamente apelidados: DRIM-team. São eles, por ordem alfabética: Ana Luísa, Andrêa Gouvêa, Carlos Oliveira, Carlos Santos, Daniel Covita, Fábio Pereira, Filipe Castro, Hugo da Luz, Lara Carramate, Luís Moutinho, Marco Peres e Tiago Neves. Convosco a palavra trabalho adquiriu novos significados. Obrigado pela vossa camaradagem e constante boa disposição.

Um agradecimento aos meus companheiros de viagem ao Weizmann Institute: Artur Coimbra, Fernando Amaro, Hugo Luz e José Escada.

The second part of this work was performed at the Weizmann Institute of Science, to which i would like to thank, especially to Prof Amos Breskin and his group, particularly to Marco Cortesi, Alexey Lyashenko, Moshe Klin and Lior Arazi. I am sincerely grateful to Prof Amos Breskin for the opportunity to work in his group and acquired knowledge.

Um obrigado ao Filipe Castro pela revisão linguística.

palavras-chave

Detectores gasosos de radiação, MHSP, THGEM, THCOBRA, Cintigrafia, Electroluminescência, GSPC, Imagiologia Médica, detectores RICH, Refluxo de iões, Fotocátodo de CsI.

resumo

Este trabalho apresenta os resultados do desenvolvimento de um detector de alta pressão de Xe, tendo em vista a sua aplicação em imagiologia médica. O detector usa dois foto-sensores UVV posicionados face-a-face baseados na CsI-MHSP, com discriminação em posição. O conhecido efeito da diminuição do ganho em carga com a pressão é compensado através de um ganho em luz usando o processo de electroluminescência. São apresentados estudos da amplitude do sinal e das resoluções em energia e posição.

Na segunda parte, são estudados detectores baseados em THGEM de modo a corresponder às necessidades, actuais e de futuro, das experiências de física de altas energias. O trabalho foca-se na aplicação das THGEM em elementos RICH, sendo sugerido um detector triplo-THGEM com um fotocátodo de CsI em misturas de Ne.

O refluxo de iões para o fotocátodo continua a ser um objecto de preocupação e uma limitação. A aplicação de uma nova estrutura é sugerida: THCOBRA. Resultados preliminares mostram boa perspectivas do sucesso da aplicação da THCOBRA na eliminação do refluxo de iões.

Ao longo deste trabalho são apresentados vários métodos e medidas do comportamento dos fotocátodos de CsI em detectores gasosos de radiação. É apresentada também uma longa discussão acerca dos seus problemas e possíveis soluções.

keywords

Radiation gaseous detectors, MHSP, THGEM, THCOBRA, Scintigraphy, electroluminescence, GSPC, Medical Imaging, RICH detectors, Ion Back-flow, CsI photocathode.

abstract

This work presents the results on the development of a high pressure Xe gaseous detector envisaging medical imaging. The detector uses two VUV photosensors operating face-to-face, based on the CsI-MHSP with position discrimination capability. The known effect of the charge gain decrease with the gas pressure is compensated with a light gain using the electroluminescence process. Studies of signal amplitude, energy and position resolution are presented.

On the second part, gaseous detectors based on THGEM where studied in order to fulfill the requirements of present and future high energy physics experiments. The work is focused on the application of THGEM in RICH detectors elements: a triple THGEM detector using CsI photocathodes in Ne mixtures was suggested.

The ion backflow to the photocathode remains a concern and a limitation; to minimize it, the application of a new hole-structure, THCOBRA, was suggested. Preliminary results foresee good perspectives for the successful application of THCOBRA in ion back-flow suppression.

This work contains several methods and measurements of the CsI photocathodes behaviour in radiation gaseous detectors. A long discussion on its issues and possible solutions are presented.

Universidade de Aveiro Departamento de Física
2011

Carlos Davide da Rocha Azevedo

Hole-type gaseous detectors for medical imaging and HEP experiments

Universidade de Aveiro Departamento de Física
2011

Carlos Davide da Rocha Azevedo

Hole-type gaseous detectors for medical imaging and HEP experiments

Dissertação apresentada à Universidade de Aveiro para cumprimento dos requisitos necessários à obtenção do grau de Doutor em Engenharia Física, realizada sob a orientação científica do Doutor João Filipe Calapez de Albuquerque Veloso, Professor Auxiliar do Departamento de Física da Universidade de Aveiro

Apoio financeiro da FCT e do FSE no âmbito do III Quadro Comunitário de Apoio (Bolsa de Doutoramento SFRH/BD/35979/2007)

Gostaria de dedicar este trabalho a todos aqueles que me acompanharam nesta etapa que agora termina. Porém vou destacar alguns daqueles que mais me marcaram neste período da minha vida.
Começo, obviamente por dedicar este trabalho ao Afonso Davide, ao Eduardo e à Patrícia: é em relação a vocês que mais dificuldades tenho em escrever a dedicatória, pois efectivamente não encontro palavras que reflictam o meu apreço.
De seguida gostaria de dedicar este trabalho a duas mulheres que admiro imenso pela enorme coragem e pela forma como enfrentam a vida: a minha mãe e a minha irmã.
Faço uma dedicatória especial para o meu pai.
Dedico também aos meus sobrinhos: Ana Rita, Ricardo Jorge e Ana Carolina, não esquecendo o meu cunhado, Jorge.
Dedico a toda a minha família, com uma atenção especial aos meus avós.
Finalmente dedico este trabalho a todos os meus amigos.

o júri

presidente

Prof. Doutor Artur Manuel Soares da Silva
professor catedrático do Departamento de Química da Universidade de Aveiro

Prof. Doutor Joaquim Marques Ferreira dos Santos
professor catedrático da Faculdade deCiências e Tecnologia da Universidade de Coimbra

Prof. Doutora Maria da Conceição Abreu e Silva
professora catedrática aposentada da Universidade do Algarve

Prof. Doutora Maria Luísa Carvalho Leonardo
professora associada da Faculdade de Ciências da Universidade de Lisboa

Prof. Doutor João Filipe Calapez de Albuquerque Veloso
professor auxiliar do Departamento de Física da Universidade de Aveiro

Doutor Daniel dos Santos Covita
Investigador do I3N, Aveiro

agradecimentos

Gostaria de enviar um agradecimento especial ao meu orientador: Prof João Veloso. Sem a sua ajuda e orientação este trabalho não teria sido possível. Um grande obrigado por esta oportunidade e pela sua dedicação na minha formação.

Quero agradecer à Fundação para a Ciência e a Tecnologia pela Bolsa de Doutoramento que me atribuiu e à Universidade de Aveiro, nomeadamente ao Departamento de Física, pela condições que me proporcionou.

Um obrigado especial aos meus colegas de laboratório carinhosamente apelidados: DRIM-team. São eles, por ordem alfabética: Ana Luísa, Andrêa Gouvêa, Carlos Oliveira, Carlos Santos, Daniel Covita, Fábio Pereira, Filipe Castro, Hugo da Luz, Lara Carramate, Luís Moutinho, Marco Peres e Tiago Neves. Convosco a palavra trabalho adquiriu novos significados. Obrigado pela vossa camaradagem e constante boa disposição.

Um agradecimento aos meus companheiros de viagem ao Weizmann Institute: Artur Coimbra, Fernando Amaro, Hugo Luz e José Escada.

The second part of this work was performed at the Weizmann Institute of Science, to which i would like to thank, especially to Prof Amos Breskin and his group, particularly to Marco Cortesi, Alexey Lyashenko, Moshe Klin and Lior Arazi. I am sincerely grateful to Prof Amos Breskin for the opportunity to work in his group and acquired knowledge.

Um obrigado ao Filipe Castro pela revisão linguística.

palavras-chave

Detectores gasosos de radiação, MHSP, THGEM, THCOBRA, Cintigrafia, Electroluminescência, GSPC, Imagiologia Médica, detectores RICH, Refluxo de iões, Fotocátodo de CsI.

resumo

Este trabalho apresenta os resultados do desenvolvimento de um detector de alta pressão de Xe, tendo em vista a sua aplicação em imagiologia médica. O detector usa dois foto-sensores UVV posicionados face-a-face baseados na CsI-MHSP, com discriminação em posição. O conhecido efeito da diminuição do ganho em carga com a pressão é compensado através de um ganho em luz usando o processo de electroluminescência. São apresentados estudos da amplitude do sinal e das resoluções em energia e posição.

Na segunda parte, são estudados detectores baseados em THGEM de modo a corresponder às necessidades, actuais e de futuro, das experiências de física de altas energias. O trabalho foca-se na aplicação das THGEM em elementos RICH, sendo sugerido um detector triplo-THGEM com um fotocátodo de CsI em misturas de Ne.

O refluxo de iões para o fotocátodo continua a ser um objecto de preocupação e uma limitação. A aplicação de uma nova estrutura é sugerida: THCOBRA. Resultados preliminares mostram boa perspectivas do sucesso da aplicação da THCOBRA na eliminação do refluxo de iões.

Ao longo deste trabalho são apresentados vários métodos e medidas do comportamento dos fotocátodos de CsI em detectores gasosos de radiação. É apresentada também uma longa discussão acerca dos seus problemas e possíveis soluções.

keywords

Radiation gaseous detectors, MHSP, THGEM, THCOBRA, Scintigraphy, electroluminescence, GSPC, Medical Imaging, RICH detectors, Ion Back-flow, CsI photocathode.

abstract

This work presents the results on the development of a high pressure Xe gaseous detector envisaging medical imaging. The detector uses two VUV photosensors operating face-to-face, based on the CsI-MHSP with position discrimination capability. The known effect of the charge gain decrease with the gas pressure is compensated with a light gain using the electroluminescence process. Studies of signal amplitude, energy and position resolution are presented.

On the second part, gaseous detectors based on THGEM where studied in order to fulfill the requirements of present and future high energy physics experiments. The work is focused on the application of THGEM in RICH detectors elements: a triple THGEM detector using CsI photocathodes in Ne mixtures was suggested.

The ion backflow to the photocathode remains a concern and a limitation; to minimize it, the application of a new hole-structure, THCOBRA, was suggested. Preliminary results foresee good perspectives for the successful application of THCOBRA in ion back-flow suppression.

This work contains several methods and measurements of the CsI photocathodes behaviour in radiation gaseous detectors. A long discussion on its issues and possible solutions are presented.

This work Publications

Papers in international scientific periodicals with referees

1. **C. D. R. Azevedo**, Carlos A. B. Oliveira, Hugo Natal da Luz, L. F. Carramate, A.L. Ferreira and J. M. F. dos Santos, J. F. C. A. Veloso, *Gas VUV Photosensors Operating Face-to-Face*, Nucl Instrum Meth A, Vol. 610, pp. 238-241, 2009

2. **C. D. R. Azevedo**, M. Cortesi, A.V. Lyashenko, A. Breskin, R. Chechik, J. Miyamoto, V. Peskov, J. Escada, J.F.C.A. Veloso and J.M.F. dos Santos, *Towards THGEM Uv photon detectors for RICH: on single-photon detection efficiency in Ne/CH4 and Ne/CF4*, 2010 JINST 5 P01002

3. A. Breskin, V. Peskov, M. Cortesi, R. Budnik, R. Chechik, S. Duval, D. Thers, A. Coimbra, J.M.F. dos Santos, **C. D. R. Azevedo** and J.F.C.A. Veloso, *CsI-THGEM gaseous photomultipliers for RICH and noble-liquid detectors*, Nucl Instrum Meth A, Vol. 639, pp. 117-120, 2011

4. **C. D. R. Azevedo**, A. L. M. Silva, A. L. Ferreira, H. Natal da Luz,

L. M. Moutinho, J. M. F. dos Santos and J. F. C. A. Veloso, *2D-Sensitive HpXe Gas Proportional Scintillation Counter Concept for Nuclear Medical Imaging Purposes*, 2011 JINST 6 C01067

5. D. S. Covita, **C. D. R. Azevedo**, C. C. Caldas and J. F. C. A. Veloso, *Photoelectron extraction efficiency from Cesium Iodide photocathodes in a pressurized atmosphere of Argon and Xenon up to 10 bar* - Physics Letters B, Vol. 701, pp. 151 - 154, 2011

Papers in conference proceedings

1. **C.D.R. Azevedo**, C.A.B. Oliveira, H. Natal da Luz, A.L. Ferreira, J.M.F. dos Santos and J.F.C.A. Veloso, *HpXe Gas VUV Photosensors Operating Face-to-Face*, IEEE NSS Conf Rec 2008, pp. 960-964, 2008

2. **C.D.R. Azevedo**, A.L. Gouvêa, A.L.M. Silva, J.M.F. dos Santos and J.F.C.A. Veloso, *2D-Sensitive HpXe Gas Proportional Scintillation Counter*, IEEE NSS Conf Rec (NSS/MIC) 2009, pp. 741-744, 2009

Oral communications

1. **C.D.R. Azevedo**, J.F.C.A. Veloso, C.A. Santos, and J.M.F. dos Santos, *Gas VUV Photosensors Operating Face-to-Face at HpXe*- Communication presented to "MAP-FIS PhD RESEARCH CONFERENCE 2008/2009", Science School Auditorium, University of Minho, Portugal, 16-17 January 2009

2. **C.D.R. Azevedo**, *MicroHole & Strip Plate Base Photosensor Operating at HpXe*- Communication presented to "MPDG2009 - 1st International Conference on Micro Pattern Gaseous Detectors", Kolympari, Crete, Greece, 12-15 June 2009

3. **C.D.R. Azevedo**, C.A. Santos, F. D. Amaro, A. Breskin, R. Chechik, J.M.F. dos Santos and J.F.C.A. Veloso, *TH-COBRA, a thick-hole structure for IBF reduction* - Communication presented to "4th RD51 Collaboration Meeting", CERN, Geneve, Switzerland, 23-25 November 2009

4. **C.D.R. Azevedo**, M. Cortesi, A.V. Lyashenko, A. Breskin, R. Chechik, J. Miyamoto, V. Peskov, J. Escada, J.F.C.A. Veloso and J.M.F. dos Santos, *Photoelectron extraction and collection efficiency studies in CsI-THGEM for Ne based mixtures* - Communication presented to "4th RD51 Collaboration Meeting", CERN, Geneve, Switzerland, 23-25 November 2009

Posters in conferences

1. J. F. C. A. Veloso, **Carlos D. R. Azevedo**, Carlos A. B. Oliveira, Hugo Natal da Luz, A.L. Ferreira and J. M. F. dos Santos; *Gas VUV Photosensors Operating Face-to-Face* - Communication presented to the 5th International Conference on New Developments In Photodetection 2008, Aix-les-Bains, France, 15-20 de June 2008

2. **C.D.R. Azevedo**, C.A.B. Oliveira, H. Natal da Luz, A.L. Ferreira, J.M.F. dos Santos and J.F.C.A. Veloso, *Gas VUV Photosensors Operating Face-to-Face at HpXe* - Communication presented to the "2008 IEEE Nuclear Science Symposium and Medical Imaging", Dresden, Germany, October 19-25, 2008

3. **C.D.R. Azevedo**, A.L. Gouvêa, A.L.M. Silva, J.M.F. dos Santos and J.F.C.A. Veloso, *2D-Sensitive HpXe Gas Proportional Scintillation Counter* - Communication presented to the "2009 IEEE Nuclear Science Symposium and Medical Imaging", Orlando, USA, October 25-31, 2009

4. **C.D.R. Azevedo**, C.C. Caldas, A.L. Gouvêa, C. A. Santos, J.M.F. dos Santos and J.F.C.A. Veloso, *CsI Photoelectron Extraction Efficiency in HpXe medium* - Communication presented to the "2009 IEEE Nuclear Science Symposium and Medical Imaging", Orlando, USA, October 25-31, 2009

5. **C.D.R. Azevedo**, A.L.M. Silva, A.L. Ferreira, J.M.F. dos Santos and J.F.C.A. Veloso, *First Results on a 2D-Sensitive HpXe Gas Proportional Scintillation Counter for Imaging* - Communication presented to the "12th International Workshop on Radiation Imaging Detector (iWoRiD)", Cambridge, United Kingdom, 11-15 July 2010

Trainne Grants and Excellence Schools

1. “Trainee Grant” given by “The 2008 IEEE NSS/MIC/RTSD Conference Committee”
2. “Trainee Grant” given by “The 2009 IEEE NSS/MIC/RTSD Conference Committee”
3. “GEM & Micromegas detector design & assembly training”, 17-20 February 2009, CERN, Geneve, Switzerland
4. “Physics and Design of Detectors for SPECT and PET”, 25 October 2009, Orlando, USA
5. “EDIT 2011 - Excellence in Detectors and Instrumentation Technologies”, 31 January-10 February 2011, CERN, Geneve, Switzerland

Contents

List of Abbreviations and Symbols

2D-MHSP	Micro-Hole & Strip Plate with position discrimination capability
$\boldsymbol{A_{eff}}$	Photocathode effective area
ALICE	A Large Ion Collider Experiment
CdZnTe	Cadmium Zinc Telluride
COMPASS	COmmon Muon Proton Apparatus for Structure and Spectroscopy
CsI	Caesium Iodide
CsI-2D-MHSP	Photosensor composed by a CsI photocathode and a 2D-MHSP
CsI(Tl)	Caesium Iodide doped with Thallium
CT	Computed Tomography
CZT	Cadmium Zinc Telluride
ESF	Edge Spread Function
E/p	Reduced Electric Field
$\boldsymbol{E_{drift}}$	Electric field in the photoelectron drift region
$\boldsymbol{E_{trans}}$	Electric field in the transfer region
F2F	Face-to-Face
FOV	Field Of View

FR-THCOBRA	Flipped Reversed-bias THCOBRA
FWHM	Full Width at Half Maximum
GEM	Gas Electron Multiplier
G_{VIS}	Visible Gain
GPM	Gaseous Photomultiplier
HADES	High Acceptance Di-Electron Spectrometer
HEP	High Energy Physics
HMPID	High Momentum Particle IDentification
HV	High Voltage
IBF	Ion Back-flow Fraction
I_{gas}	Photoelectron current in gas
I_{PC0}	Initial photocathode current
I_{vacuum}	Photoelectron current in vacuum
LHC	Large Hadron Collider
LSF	Line Spread Function
MIP	Minimum Ionizing Particle
MPGD	Micro-pattern Gaseous Detector
MRI	Magnetic Resonance Imaging
MSGC	Micro-Strip Gas Counter
MTF	Modulation Transfer Function
MWPC	Multi-Wire Proportional Chamber
NaI(Tl)	Sodium Iodide doped with Thallium
PACEM	Photon-Assisted Cascaded Electron Multiplier
PCB	Printed Circuit Board
PET	Positron Emission Tomography
PHENIX	Pioneering High Energy Nuclear Interaction eXperiment
PID	Particle Identification
PMT	Photomultiplier Tube
PSF	Point Spread Function
QE	Quantum Efficiency

RHIC	Relativistic Heavy Ion Collider
RICH	Ring Imaging Cherenkov
ROI	Region Of Interest
R&D	Research and Development
R-THCOBRA	Reversed-bias THCOBRA
SEE	Secondary Electron Emission
SNR	Signal-to-Noise Ratio
SPECT	Single Photon Emission Computed Tomography
STAR	Solenoidal Tracker at RHIC
TPC	Time Projection Chamber
THCOBRA	THick COBRA
THGEM	THick GEM
$\mathbf{V_A}$	Anode Voltage
$\mathbf{V_{AC}}$	Voltage difference between the strips (V_A-V_C)
$\mathbf{V_C}$	Cathode Voltage
$\mathbf{V_{CA}}$	Voltage difference between the strips (V_C-V_A)
$\mathbf{V_{CT}}$	Voltage difference between the cathode strips and the top electrode(V_C-V_T)
$\mathbf{V_{hole}}$	Voltage difference between the anode strips and the top electrode(V_A-V_T)
$\mathbf{V_T}$	Top electrode Voltage
VUV	Vacuum Ultra Violet
YAP:CE	Cerium-doped Yttrium Aluminium Perovskite
ε_{coll}	Single-electron collection efficiency
ε_{effph}	Effective photon detection efficiency
ε_{extr}	Photoelectron extraction efficiency
ε_{hole}	Photoelectron hole-focusing and multiplication efficiency
ε_{photon}	Absolute single-photon detection efficiency
ε_{trans}	Avalanche fraction transfer efficiency
ϵ_{UV}	Average energy of a Xe scintillation photon

List of Figures

List of Equations

Part I

Study and development of UV position sensitive photosensors coupled to detectors envisaging medical imaging

1 Introduction

The term "medical imaging" covers different modalities: Radiology, Nuclear Medicine Imaging, Magnetic Resonance Imaging (MRI) and Ultrasound Imaging. From the medical perspective, each modality has its own applications depending on the required information or detail level needed. From the physics point of view the modalities differ in the physical processes used to obtain the images.

In ultrasound imaging, a high frequency sound pulse generated by a transducer will be reflected by internal structures in the body generating echoes. The echo, when returning to the transducer will be computed in order to generate the ultrasonic image.

MRI makes use of a magnetic field and a pulse of radio waves to produce the images. The protons (hydrogen atom nuclei) in the patient absorb the radio waves, and re-emit them after a period of time that depends on the very localized magnetic properties of the surrounding tissue.

Both Radiology and Nuclear Medicine Imaging make use of radiation to produce images. In Radiology, the energy source (X-ray tube) is positioned outside the patient while the detector is positioned on the patient opposite side, generating transmission images. Radiology can be split in different modalities as radiography, mammography, fluoroscopy and computed tomography (CT). Again each modality has its own applications retrieving different medical information [1–3].

1.1 Scintigraphy SPECT and PET

Nuclear Medicine Imaging can be distinguished in three sub-modalities: planar imaging (scintigraphy), Single Photon Emission Computed Tomography (SPECT) and Positron Emission Tomography (PET). In Nuclear Medicine Imaging a compound containing a radioactive isotope is administrated to the patient. Once the compound has distributed itself according to the physiologic status of the patient, a position sensitive radiation detector is used to make projection images of the X- and/or γ- rays emitted during radioactive decay of the agent. Thus, by measuring the energies of the emitted photons, a unique identification of the radiotracer can be made, while determination of the origin of their emission provides information about this radiotracer distribution, and signal intensity (number of recorded photons) relates to the amount of the radiotracer at any given location.

Because the radioisotopes emit their energy from inside the patient the generated images are known as emission images[1–3].

1.1.1 The Anger Camera (Gamma Camera)

The most spread detector in Nuclear Medical Imaging is the Anger Camera, proposed by Hal Anger in the late 1950s [4, 5]. The schematic of a conventional Anger Camera, or Gamma Camera is presented in Figure 1.1. The detector itself, consists of a large single Sodium Iodide doped with Tallium (NaI(Tl)) crystal, typically 50 cm in diameter, optically coupled to an array of photomultiplier tubes (usually 50-90).

The interaction of a γ-ray with the crystal results in a burst of isotropically emitted scintillation photons partially detected by the photomultipliers. Two coordinates of the photon interaction position are obtained from the amplitude distribution of the PMT signals using Anger logic and the energy is obtained from their sum. Both the position and energy resolutions are strongly determined by the number of detected scintillation photons per interacting γ-ray [4].

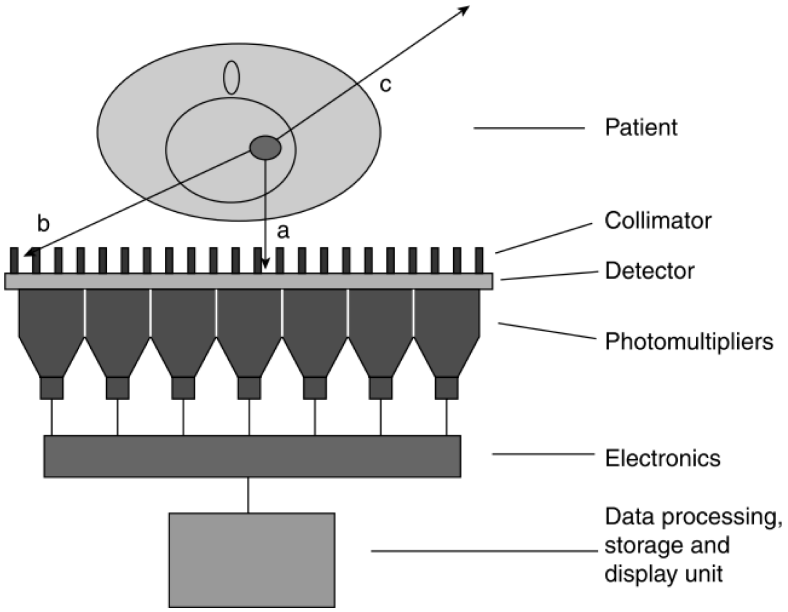

Figure 1.1: The simplified schematic of a gamma camera. Three photons originating from a tumour in a patient head are shown. Photon a is parallel to the collimator septa and is therefore transmitted through it and recorded by the detector. Photon b is absorbed by the collimator and photon c completely misses the camera. Adapted from [5].

In order to determine the exact direction from which the detected photons arrive, a thick lead collimator is placed in front to the Anger Camera. For most clinical applications, parallel hole collimators are used; however, several other collimator types are being used (fan-beam, cone-beam, pin-hole) depending on the different applications and optimized for each one [5].

Single-photon imaging studies make use of Anger cameras, with one, two, or even three large-area detectors, operating in event counting mode [4], attached to a gantry. Since practically all currently available Anger cameras are able to perform rotations and reconstruct tomographic SPECT images, these systems are often referred to as "SPECT cameras" [5].

Even though SPECT uses a wide range of radioisotopes, their emission photons energy is within the 70 to 360 keV range, ^{99m}Tc being the most popular imaging isotope, which emits 140 keV gamma photons; energy to which the majority of SPECT systems are optimized [5].

	NaI(Tl)	CsI(Tl)	YAP:CE
Emission peak (nm)	410	565	360
Light yield (ph/kev)	38	65	18
Density (g/cm^3)	3.7	4.5	5.4
$1/\mu$ (mm) at 140 keV	4.1	2.8	7

Table 1.1: Some characteristics of the most used crystals in radioisotope medical imaging detectors. Adapted from [4] and[6].

1.1.2 State-of-art of SPECT detectors

As mentioned the most popular detector in SPECT/scintigraphy scanners is the Anger Camera, composed by a scintillation crystal with PMT light readout. Sodium iodide doped with Thallium, NaI(Tl), is certainly the most used crystal in the Anger cameras [4, 5]. Recently other crystals have been considered as for example CsI(Tl) and YAP:Ce, Caesium iodide doped with Thallium and cerium-doped yttrium aluminium perovskite, respectively. These crystals have been investigated intensively due to their scintillation properties and γ-rays attenuation properties (see Table 1.1) as well as their suitable physical and mechanical characteristics such as the absence of cleavage planes, giving the possibility to build Anger Cameras with segmented crystals instead of a single one, what in principle could increase the position resolution [4]. This technique could not be used with a NaI(Tl) crystal as it suffers from a fast degradation due to its high hygroscopicity, imposing the need for an air-tight container in order to keep the crystal properties [6].

Focusing on the light yield value, CsI(Tl) seems to be the best choice for SPECT application. However, CsI(Tl) emission is peaked at 565 nm, a poorly matched combination with the PMT response, namely the ones using S-11 or bi-alkali photocathodes. For that reason, the photosensor output is often quoted as being substantially lower with CsI(Tl) [6].

Although NaI(Tl) crystals are highly efficient in detecting radionuclide emission photons and converting its absorbed energy into light photons (a 1 cm thickness NaI(Tl) crystal provides 80-90% detection efficiency for 140 keV

photons), the amount of light produced is still quite small [5], justifying the constant R&D in scintillation crystals.

An hexagonal PMT array is often used to cover the crystal and convert the scintillation light signal into an electric signal in order to calculate the event position interaction and energy. To determine this location an Anger logic is used: the event spatial interaction position is determined by combining the electrical signal from each photomultiplier tube in a logic circuit that weights the signals in an appropriate way [5].

The sensitivity of SPECT imaging, besides the crystal material and PMT photocathode sensitivity to the scintillation photons also depends on the collimator acceptance angle, and on the solid angle which is subtended by the detecting system. Each collimator hole presents an acceptance angle, i.e., in theory, only photons parallel to the collimator septa should pass through the holes and reach the detector, in practice the collimator accepts all photons within a small cone. This means that the spatial resolution of the camera (Full Width at Half Maximum, FWHM, of the Point Spread Function, PSF) depends on the distance between the source and the collimator, deteriorating as the distance increases [2, 5, 7, 8], and given by:

$$\text{FWHM} \approx D + d(\frac{D}{L}) \tag{1.1}$$

where D is the hole diameter, d is the collimator-object distance and L is the hole length [7, 8].

Additionally, since only very few photons are emitted within the collimator acceptance angle, the efficiency of the detection process is very low, usually on the order of 10^{-4} [2, 5]. The sensitivity g does not depend on the collimator-object distance but is strongly dependent on the hole diameter D:

$$g \approx (\frac{D}{L})^2(\frac{D^2}{(D+h)^2}) \tag{1.2}$$

where h is the thickness of septum between holes [7, 8].

By comparing Eq. 1.1 and Eq. 1.2 we can notice that in order to achieve

higher position resolution a collimator with small holes should be used, but, opposingly, the sensitivity will decrease. Of course, if a high sensitivity is desired, a collimator with large holes should be used, at the cost of a degradation of the position resolution.

Other collimator types, like converging collimators, improve sensitivity and resolution of the study, but distort imaging geometry. Therefore special algorithms are required for image reconstruction [5].

The Anger cameras, or improved variants, still present some limitations. They exhibit degradation of the position resolution towards the camera edge, non-uniformity and various forms of image distortion. Also, improvement of their energy resolution is mandatory for a better γ-ray discrimination. Better energy resolution will improve the rejection of scattered photons in the body increasing the image contrast [4].

Summarizing, typical Anger cameras present a counting rate capability of 10^5 cps with intrinsic spatial resolution of 3-5 mm (FWHM) [2, 4] and energy resolution of 9-11% for 140 keV γ-rays by using a NaI(Tl) scintillator. As the attenuation length of 140 keV photons in NaI(Tl) is 4 mm, a 12 mm thick crystal assures more than 95% of interaction efficiency, defining the intrinsic detection efficiency of the system [4].

A promising alternative to scintillation crystals for gamma cameras, extensively studied, are the semiconductor detectors, with the first commercial systems becoming available recently [5] . The most attractive one, Cadmium Zinc Telluride (CdZnTe or CZT), has interesting properties for SPECT applications: very good absorption characteristics due to its high effective atomic number (near 50) and density (5.8 g/cm^3) and an attenuation length ($1/\mu$) for 140 keV photons of only 3 mm. It has a good charge yield (the 140 keV full absorption produces approximately 3×10^4 electrons) on the basis of which an excellent intrinsic energy resolution is expecte [4, 9]. Also it presents high resistivity ($10^{11}\,\Omega$cm), due to the wide band gap (1.57 eV), resulting in low leakage current, and, consequently, low noise characteristics. CZT has good electron transport properties resulting in a relatively fast and a efficient

electron collection [4, 7, 10].

However, CZT intrinsic energy resolution is dependent on the semiconductor thickness: CZT presents poor charge transport characteristic for holes and a large hole trapping probability. It means there are significant charge losses during the drift under a bias electric-field. In a simple planar ionization detector this introduces a dependence of the charge signal amplitude with the γ-ray interaction point on the detector, resulting on a broad photopeak in the pulse height spectrum. As the energy resolution degrades with the semiconductor thickness, a good energy resolution resolution is possible only with a slim semiconductor, deteriorating the detection efficiency and image contrast to levels worst than the conventional Anger cameras [4, 7, 10].

1.1.2.1 Animal SPECT detectors

Imaging of small animals, such as mice and rats, is especially attractive as they are easy to handle; the studies are inexpensive and several excellent small animal disease models have been developed [5]. The relatively small size of the objects under study in small animal imaging (rats and mice's small organs or brain) makes it difficult to use imaging instruments developed for human subjects. In order to obtain the same visualization detail as for human scanners, it would be necessary to have instruments with the same ratio between volume spatial resolution and object volume, i.e. instruments with a spatial resolution better than 1 mm. However, it is usually acceptable to work with a spatial resolution better than 2 mm FWHM for rats (for example for the imaging of the brain), while for mice it would be ideal to use instruments with a resolution of less than 1 mm FWHM [8].

Also, due to the bulky and heavy design of the conventional Anger camera, it is often difficult to position it as close to the human organ as desired and to obtain the most suitable view. This difficulty is enhanced by the existence of a dead zone of several cm at the camera edges. The limitation in the device positioning is particularly important when imaging small organs as, for instance, in scintimammography, endocrinology, small animal ima-

ging or intra-operative radio-guided surgery (RGS)[11, 12]. In view of these demands, new gamma cameras have been designed and tested adopting technical solutions as optically isolated crystal pillars read by a single PSPMT, very thin crystals individually read out by PIN silicon photodiodes and the direct application of pixelated semiconductor detectors with charge readout [4].

The use of pinhole collimators is a solution for ultra-high-resolution SPECT [5, 8]. For this type of collimators the FWHM spatial resolution is given by:

$$\text{FWHM} = D_e \frac{(d+b)}{b} \tag{1.3}$$

where d is the distance between the object and the pinhole and b is the distance between the pinhole and the scintillator. D_e represents the effective diameter of the pinhole, depending also on the attenuation coefficient of the collimator material and on the hole aperture [7, 8]. By using the intrinsic geometrical magnification of a pinhole collimator, it is then possible to obtain high-resolution images with a FWHM of the same order of $D_e (b > d)$. Note that, in pinhole collimators the sensitivity is proportional to $1/d^2$, thus the closer the object is to the hole, the higher is the sensitivity [8]. Since imaging with single pinhole results in dramatically low efficiency, usually multiple pinholes in non overlapping or overlapping configuration are used. These systems have much better resolution (0.5-2 mm) and sensitivity ($\sim$0.3%) than clinical SPECT cameras; the cost is, however, a small field of view, FOV, (5-8 cm) [5].

Commercial devices like X-SPECT® by Gamma Medica-Ideas present a maximum FOV of $12.5 \times 12.5\,\text{cm}^2$ by using a parallel-hole collimator. If maximum sensitivity is mandatory, a ϕ=2 mm pinhole collimator should be used providing 855 cps/MBq, while the best FWHM spatial resolution (0.62 mm) is obtained with a ϕ=0.5 mm pinhole collimator. Other example is the NanoSPECT system by Bioscan, presenting spatial resolutions that range from FWHM$\leq$1.2 mm with 1.5 mm multi-pinholes to FWHM$\leq$0.8 mm

with 1.0 mm multi-pinholes. Both systems are multi-head NaI(Tl) based detectors (2 in the former case and 4 in the latter) [8].

Several small FOV γ-ray imaging systems based on CZT detectors are being developed for medical applications [4, 11]. Generally such devices present an intrinsic position resolution of a few hundred microns with energy resolution between 4% and 8% for 140 keV γ-rays. The detection efficiency is lower than that of the conventional Anger camera: for 140 keV γ-rays varies typically from 60% to 80%, depending not only on the thickness of the semiconductor but also on the position correction method. The main drawbacks besides the modest efficiency are their costs [4].

Other detector technologies have been suggested and pursued, as for example, liquid Xenon that has been recognized long ago as a very good γ-ray detector medium. The successful operation report of a liquid Xenon ionization chamber with imaging capability can be found in [13].

The proposed detector just makes use of the primary charge produced upon direct conversion of the γ-rays in the Xenon, using a $50\times50\,\mathrm{mm}^2$ bi-dimensional micro-strip plate based charge readout. First results already showed the feasibility of the concept and the possibility of obtaining a position resolution better than 2 mm for 122 keV γ-rays [4, 13]. In conclusion, the development of new gamma cameras for SPECT/scintigraphy has been carried out along two main directions: the development of compact, small area, task-specific gamma cameras and the improvement of performance of the conventional large area gamma cameras, by optimizing the light collection and using recently developed position-sensitive photomultipliers or by using a completely different detection technique such as liquid and gas Xenon detectors [4, 14–16].

1.2 F2F detector: A new concept for a gamma-camera

The detector here presented follows the work started and developed during my Master degree [17], being the result of 2 actual R&D interests: high pressure Xenon gaseous detectors [18] and gaseous VUV (vacuum ultra violet) photosensors [19]. The main goal is to develop and study a windowless gamma-camera by replacing the radiation detection media, i.e., by replacing the scintillation crystal by a scintillation gas: Xe. Also, the light readout photosensors are replaced by a low cost device with already proved performance: a VUV photosensor based on a gaseous micro pattern gas detector (MPGD) [20, 21].

The Face-to-Face (F2F) detector concept is based on simplicity: detect the gamma photons with a high pressure Xenon gas detector using its scintillation light for signal amplification purposes; read the light with 2 gaseous VUV photosensors, operating face-to-face, within the same Xenon gas medium [21, 22]. This concept avoids the use of crystals or complex PMTs/photodetector array systems (those require complex electronics systems for triggering, coincidence determination and position calculation), as the Xe is used as detection and amplification media (window-less).

High pressure gaseous detectors, based on micro-structures technology, have shown the possibility to detect hard X- and γ-rays with fair detection efficiency [23–25]. In addition, advances in VUV photosensors operating within the Xenon medium allows the efficient detection of the VUV photons resulting from Xenon scintillation [26, 20].

The main drawback in the use of gaseous radiation detectors applied to nuclear medical imaging, especially when the goal is to detect 140 keV photons, is the low detection efficiency for that energy. A possibility to increase the detection efficiency of a noble gas detector is, in first approach to use Xe, which is the natural noble gas with the highest atomic number, and secondly, to increase the gas density by increasing the pressure [18, 25, 27].

However, electron-avalanche based gaseous detectors present a gain decrease behaviour with the increasing pressure [23, 28, 29], leading to a degradation of the position and energy resolutions [30]. A solution to reduce this effect [28] goes through a gas scintillation amplification stage, i.e., the VUV scintillation photons emitted by the gas atoms through electroluminescence processes [31, 32]. The number of VUV photons emitted per primary electron increases with gas pressure for the same reduced electric field, E/p, resulting in an increase of the scintillation amplification and, consequently, an increase of the detector gain [28]. For the VUV readout, a CsI-2D-MHSP photosensor (based on a CsI (Caesium Iodide) photocathode deposited on a 2D-MHSP top electrode) is used [20, 33, 34]. The operation principle and the detector concept is described in detail in the following sections.

The F2F prototype was built from a Duraluminium block, with thick walls in order to ensure 10 bar gas pressure, see Figure 1.2. Inside, 2 photosensors are positioned face-to-face with 7 stainless steel meshes in between. On top and bottom covers, several feedthroughs were glued in order to bias the electrodes and readout the photosensors signals.

More details on the F2F construction, photocathode deposition, gas injection/purification and previous studies can be found in [17]

1.2.1 Operation principles

1.2.1.1 Gamma-photon detection and primary charge production

Figure 1.3 presents the F2F detector operation principle: a 140 keV γ-photon interaction with a Xe atom results in the atom ionization, mainly through the photoelectric effect. In this process, the gamma-photon completely transfer its energy to an electron of the Xe bound shells, with the extracted electron energy given by:

$$E_c = E_i - E_b \tag{1.4}$$

where E_c is the kinetic energy of the electron, E_i represents the photon

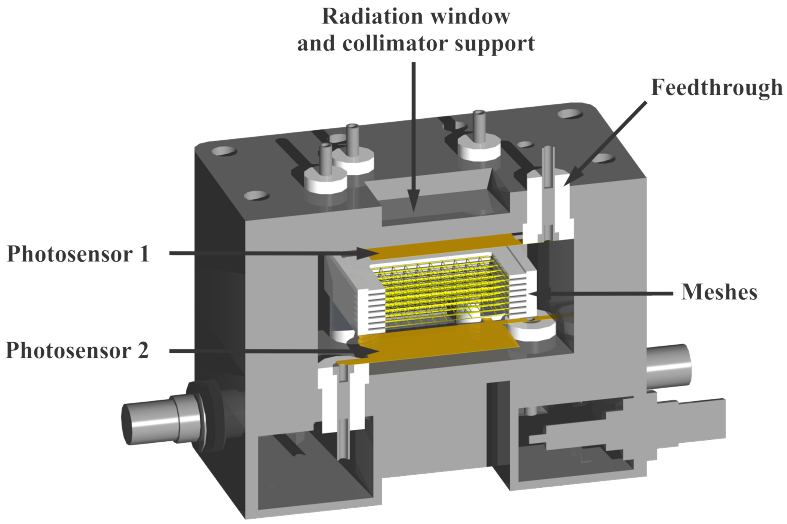

Figure 1.2: F2F detector vertical cross section.

energy and E_b is the binding energy of the electron in its original shell. The extracted electron will have enough energy to ionize other Xe atoms and, as a result, new electrons will be produced. Again, if the new produced electrons have enough energy other ionizations could occur until their energy becomes smaller than the required energy to produce an eletron-ion pair. The produced electrons during the gamma interaction process are called "primary electrons", and their group is designed as "primary electron cloud" [6, 18]. Note that other mechanisms could take place during the primary charge formation, as for example, the emission of one or more characteristic X-ray photons, Auger electrons, etc, resulting in a complex process [6]. As a result of the various processes, the average number of primary electrons is given by:

$$N_{ep} = \frac{E_i}{W} \tag{1.5}$$

where E_i is the gamma-photon energy and W is, by definition, the required energy for an electron-ion pair production [6, 18], which, in the case of Xe gas is 22.1 eV [18].

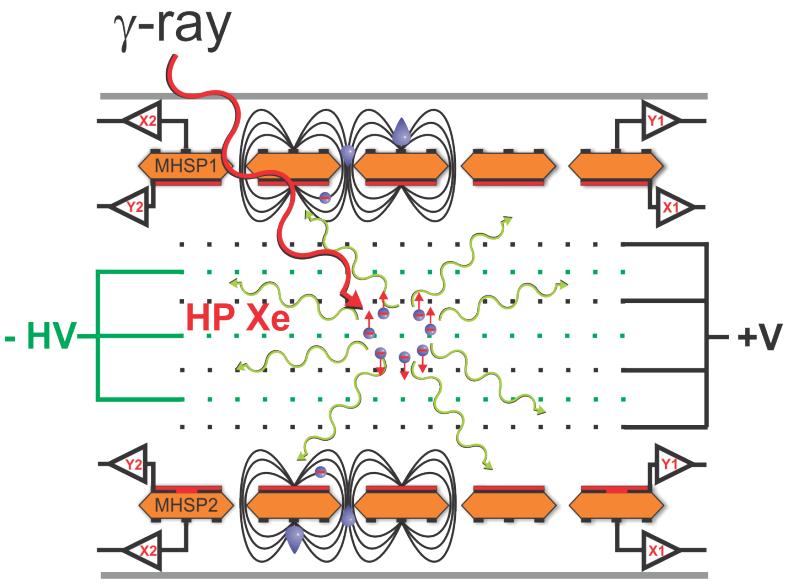

Figure 1.3: Scheme of the F2F detector operation principle.

1.2.1.2 "Light amplification"

In the absence of an electric field, the recombination process is 100% efficient and all electrons and ions produced by the absorbed radiation eventually recombine and generate a flash of VUV light. This process is called primary scintillation [18]. Even considering that each ionisation/excitation will origin a VUV photon, the number of produced photons will be small. Another process denominated by electroluminescence or secondary scintillation is often used to increase the number of produced VUV photons: in the presence of a sufficiently high electric field, primary electrons can gain enough energy between successive collisions to cause excitations of atoms or secondary ionizations. If the energy gained between collisions of the drifting electrons is slightly below the ionization threshold, they do not initiate charge multiplication avalanches but rather excite the gas atoms generating intense electroluminescence light [18], consisting on a narrow line peak at 175 nm, with 15 nm FWHM, for pressures above a few tenths of mbar [35].

In order to control the primary electrons energy during the drift, the F2F detector uses 7 stainless steel meshes distanced by 1.4 mm, Figure 1.3, crea-

ting 6 absorption/scintillation regions, i.e., by analogy, 6-in-series driftless gas scintillation proportional counters [36]. The meshes are biased intercalated to +V (positive low voltage, i.e., <200 V) and -HV (negative high voltage), the external meshes being the positive ones, positioned ∼5 mm from each photosensor [21, 22, 28].

To keep the primary electrons with enough energy to excite but not to ionize the Xe atoms, the reduced electric field (E/p), i.e. the electric field normalized to the gas pressure, should be kept between the excitation and ionization thresholds, which for Xe roughly corresponds to the range of 1 to and 6 $\mathrm{Vcm^{-1}Torr^{-1}}$ [31]. In this condition the number of scintillation secondary photons will be proportional to the number of primary electrons and to E/p, given by:

$$N_{TfUV} = \frac{\Delta V.e}{\epsilon_{UV}} \times Q_c \tag{1.6}$$

where N_{TfUV} is the number of secondary scintillation photons per primary electron, ΔV is the voltage difference between the meshes, ϵ_{UV} is the average energy of a Xe scintillation photon (7.2 eV [37, 38]), Q_C is the scintillation efficiency ($Q_C \approx$ 0.8 for Xe at E/p=5 $\mathrm{Vcm^{-1}Torr^{-1}}$ [31]) and e represents the electron charge [38].

The F2F detector makes use of 2 photosensors in order to read out the scintillation light. The main idea is to combine the contributions of both photosensors in order to increase the detector output signal. Of course, due to the solid angle variation, the number of photons that reach each photosensor will be dependent on the gamma-interaction point relatively to the photosensor, thus indicating the need for an energy correction method.

A correction method based on a pulse-shape analysis [39] could be implemented in order to avoid the interaction position contribution. Although, as the photosensors have different signal amplitudes depending on the distance to the interaction point, it will be possible to calculate the interaction point by just analysing the contribution of each photosensor, and also possible to use these values to correct the solid angle contributions [40].

1.2.1.3 The CsI-2D-MHSP UV position sensitive photosensor

The purpose of a photosensor is to produce a response when "excited" with light. Photosensors with capability to produce a response to a single photon are designated as single-photon detectors. Nowadays there is a huge amount of different photosensors based on different technologies and working principles, as for example, CMOS, CCD, photoresistor, photodiodes, phototransistors, etc.. This work makes use of another photosensor type: the photocathode [41].

The photocathode's response to a light stimulus is produced through the ejection of an electron, in this case named a photoelectron. But photocathodes are not the perfect photosensor and the efficiency of converting a photon into a photoelectron, the Quantum Efficiency (QE), is defined as:

$$QE = \frac{N_e}{N_{ph}} \tag{1.7}$$

where N_{ph} is the number of photons impinging the photocathode and N_e is the number of ejected photoelectrons. The QE is an intrinsic property of the photocathode that is mostly dependent on the photocathode material, the status of its surface and on the impinging photon wavelength [42]. Also it depends on the photocathode geometry (reflective or semitransparent) [43], the substrate material [44], the deposition technique [45] or the humidity exposition [44, 46, 47]. A concise review on CsI photocathode properties is presented in [43].

In Figure 1.4 are plotted the Ar and Xe gas emission spectra at atmospheric pressure (adapted from [48]) together with several photocathodes QE (CsI [43, 49]; CVD diamond and CsBr [49]; KBr and CsI semi-transparent [43]) showing the match between the photocathode choice and the gas emission spectra. From the extensive literature on photocathodes, CsI is without any doubt, the most used and suitable photocathode for the VUV region, where the electroluminescence emission peaks of noble gases, namely Xe, Kr and Ar, are centered. This is the reason why CsI is used as a photo-converter

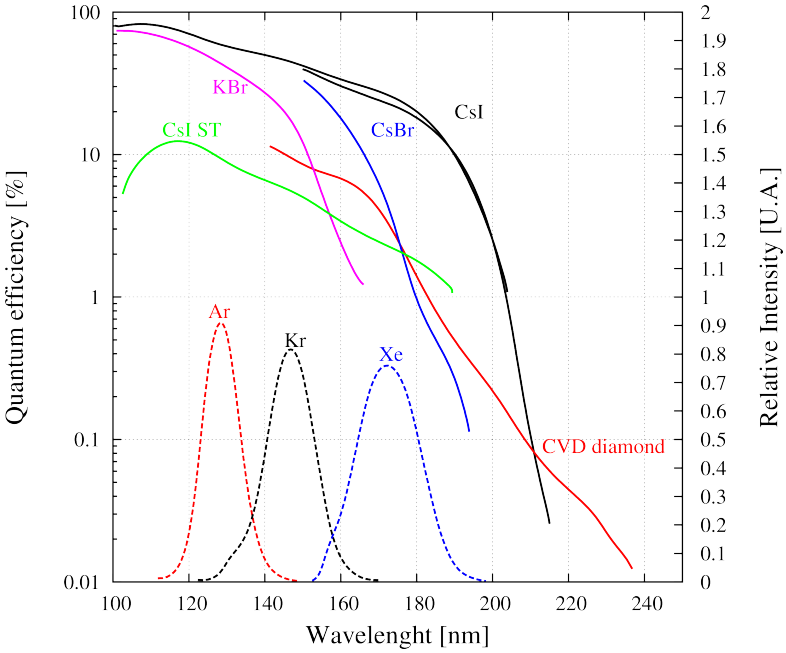

Figure 1.4: Several photocathodes QE (solid lines) adapted from [43, 49]; Ar, Kr and Xe emission spectra at atmospheric pressure (dashed lines) [48] as a function of the wavelength.

in several applications like: high energy physics (HEP) experiments using gaseous detectors (namely in Ring Imaging Cherenkov (RICH) detectors, as for example: ALICE [50], COMPASS [51], HADES [52], STAR[53], PHENIX [54], etc) or as PMT photocathode.

Some interesting characteristics that make CsI the natural choice as VUV photocathode are [43]:

- Its Quantum Efficiency (QE) to limited in the short wavelengths by optical window or gas absorption presenting a cutoff in the long wavelengths around 210 nm (Eg≈6 eV) [43, 49].

- Conversion and emission at the surface layer, important characteristics for high photon flux and for ultimate location and timing.

- Simple preparation by standard thermal evaporation technique[45].

- Suitable for several substracts including Cu-Ni/Au[44] (usual substrate in MPGD).

- Large-area application, low volume and high resistivity make possible its stable operation in high radiation flux under high multiplication conditions.

- Radiation-hardness, an important parameter for long term operation under high radiation environments.

- Moderate hygroscopic properties that allow few minutes exposition to air without visible degradation [44] and QE possible recovery by post-treatment.

The low number of extracted photoelectrons does not allow the direct charge reading without amplification, triggering the use of a device with the capability to multiply the photoelectrons and, at the same time collect the multiplied charge discriminating the position: the 2D-MHSP [33, 34]. The 2D-MHSP, Figure 1.5, is a new double-sided micro-pattern gas electron multiplier with 2D discrimination capability [30, 55].

The 2D-MHSP integrates in a single plate, two successive independent charge amplification stages: a GEM-like hole-avalanche [56] and an MSGC-like anode-strip avalanche [57], resulting in a high total gain. Like the GEM, the 2D-MHSP is manufactured with printed circuit board technology from a 50 μm thick Kapton® foil, metallized with 5 μm thick Cu-Ni/Au layers on both sides. A GEM-like pattern of bi-conical holes (50/60 μm diameter) is etched through the foil with a stripped metal electrode on the top side (Figure 1.5 a), and a standard microstrip pattern etched on the bottom side (Figure 1.5 b), with the holes centred and running along the cathode strips. The width of the cathode and anode strips are 100 μm and 20 μm, respectively, with a 200 μm pitch. The strips on the top-side, etched in a perpendicular direction relatively to the bottom strips, have the holes etched in the middle and present a *zigzag* pattern due to the hexagonal distribution

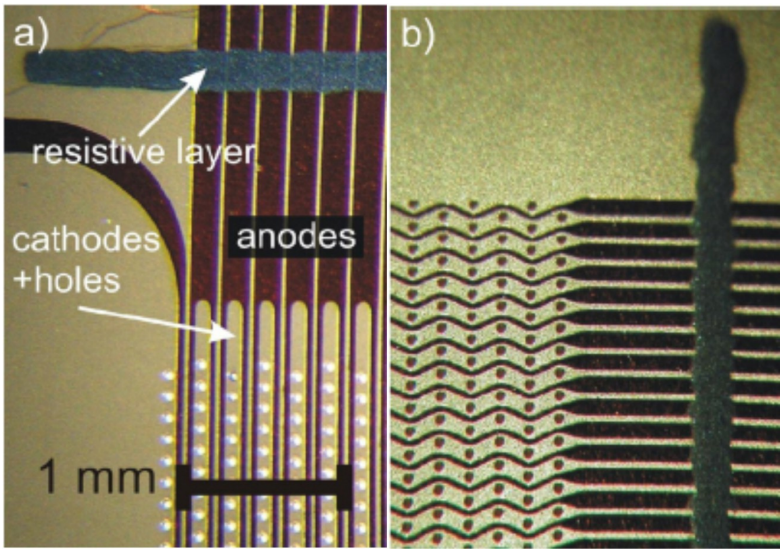

Figure 1.5: The 2D-MHSP. a) bottom side: the holes are aligned along the cathode strips, the resistive strip interconnects the anode strips; b) top side, structured with strips interconnected with a resistive strip. Adapted from [30].

of the holes, Figure 1.5. The 2D capability is achieved through a resistive charge division method [58, 59] by interconnecting the strips on both sides with a resistive layer presenting, usually, a resistance of about $400\,\Omega\text{mm}^{-1}$ [30, 33, 34, 55, 60].

The 2D-MHSP properties that make it suitable for the F2F concept are: charge gain as high as 5×10^4, and energy resolutions of 14% for 5.9 keV and 8% for 22.1 keV in pure Xe at atmospheric pressure [61]; position resolutions of about 130 and 250 μm (σ), along the X- and Y-direction, respectively, for 8 keV photons, with a FOV of $28\times28\,\text{mm}^2$ [30]; a count rate capability up to $0.5\,\text{MHz/mm}^2$ at a 10^4 gain without noticeable gain neither energy resolution degradation [62] and a fast signal response 10-30 ns (in Ar/30%CO_2) [63].

Figure 1.6 presents the operation principle schematic of the CsI-2D-MHSP photosensor.

As already mentioned, when a VUV photon hits the photocathode, a photoelectron could be ejected. After a successful extraction, the photoelectrons are focused into the holes where a strong electric field is applied by V_{CT}

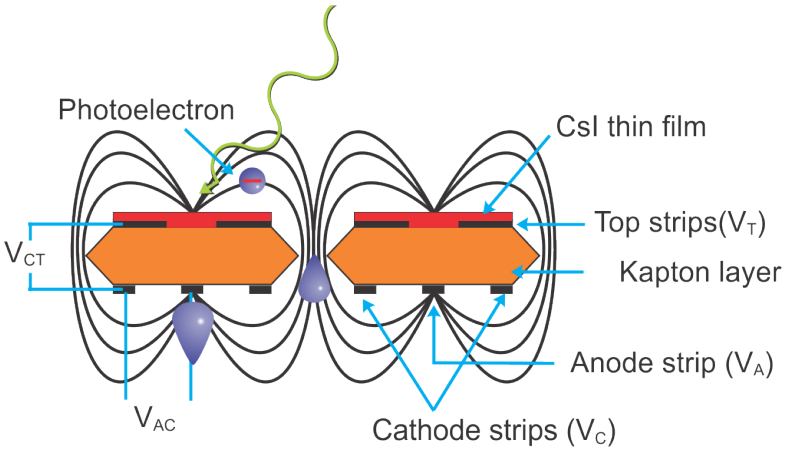

Figure 1.6: The CsI-2D-MHSP photosensor schematic.

(voltage difference between the top electrode (V_T) and the cathode electrode (V_C)) and multiplied through a Townsend Avalanche process. The avalanche electrons are then extracted from the holes region towards the anode strips where they are again multiplied in another strong electric field produced by V_{AC} (voltage difference between the cathode and anode strips (V_A)) [28]. For the 2D imaging capability, two thin orthogonal resistive lines of about 400 Ωmm^{-1} were used. The interaction position of the X- or γ-photons in the gas can be determined by acquiring and weighting the signal amplitudes from the top and bottom electrodes of the CsI-2D-MHSP photosensor, as presented in the scheme of Figure 1.7.

For one of the dimensions, the anode-strips (bottom side) are interconnected through the resistive line. For the second dimension, the top side is also structured in several different strips perpendicular to the anodes, all connected through the second resistive line. The charge deposited in the strips is collected at both ends of the resistive line, and the difference in amplitudes allows the centroid determination of each event's charge distribution. For each coordinate, the signals from both ends of the resistive line, X_A and X_B, are used to obtain the centroid distribution position, X, of the charge produced in the photosensor according to:

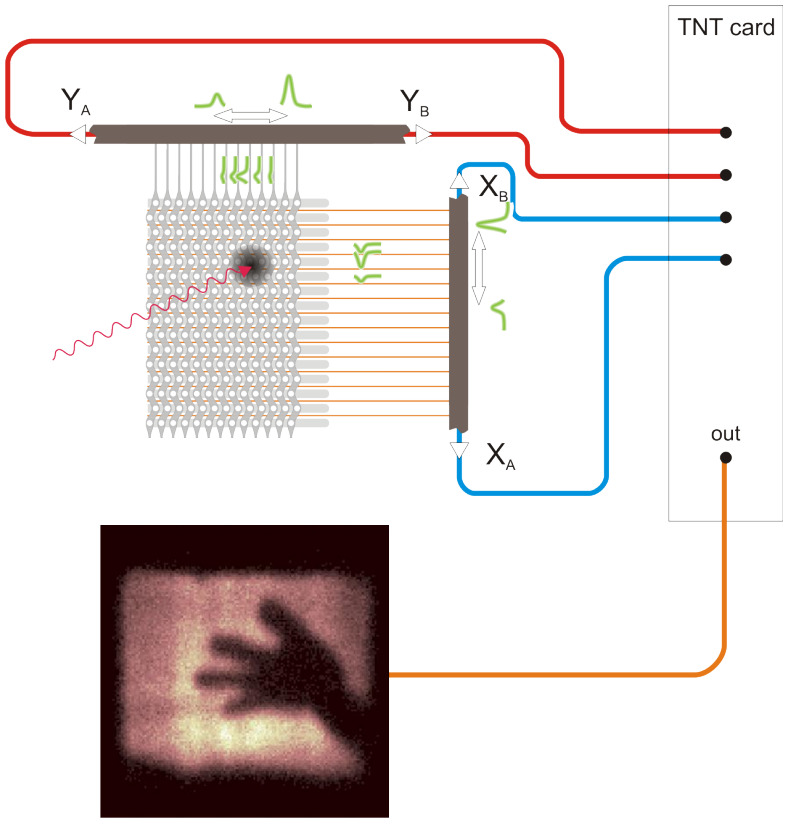

Figure 1.7: Resistive charge division method schematics. For each dimension, the charge reaching each end of the resistive layers gives information about the position where the primary electron cloud was formed. Adapted from [33].

$$X = k\frac{X_A}{X_A + X_B} \tag{1.8}$$

where k is a calibration factor. The total pulse amplitude, i.e. the energy information, is obtained by summing both amplitude contributions X_A and X_B of the shared charge for each event [30, 33, 34, 55, 60].

Note that, the signals on the top electrode are not originated by the back-flow of positive ions. They are induced by the charge on the anode strips across the Kapton® substrate as the 2D-MHSP acts like a capacitor, with Kapton® being the dielectric material [60].

2 Studies and Measurements

2.1 CsI photoelectron extraction efficiency into Ar and Xe atmospheres from 1-10 bar

Besides the photocathode QE, other parameters can affect the absolute single-photon detection efficiency (ε_{photon}) - the number of single-photon events which are detected per impinging photon, of a micro-pattern gaseous detector. If the gaseous detector uses a reflective photocathode there are 3 major parameters to consider: the photocathode QE, the photocathode effective area (A_{eff}) and the photoelectron extraction efficiency (ε_{extr}) [42, 64, 65]. The first one, QE, is as intrinsic property of the photocathode, which has already been discussed in the previous chapter. The photocathode effective area (A_{eff}) is the fraction of the micro-pattern device surface not covered by holes [42], i.e., the area where the photocathode is deposited. The photoelectron extraction efficiency is the probability of an ejected photoelectron to be successfully extracted from the photocathode vicinity without returning to it. In a gas medium, when a photoelectron is ejected from the photocathode, it has a probability of colliding with the gas atoms/molecules and returning to the photocathode where it is reabsorbed. This phenomenon, known as Photoelectron Backscattering has a major importance as it is responsible for the decrease of the charge signal amplitude (in case of multiple photon

operation) or, in the most sensitive applications where single-photoelectron detection is a demand, a loss on the number of detected events [66, 67].

The photoelectron extraction efficiency (ε_{extr}) is defined as the ratio between the number of successful extracted photoelectrons into gas relatively to vacuum:

$$\varepsilon_{extr} = \frac{I_{gas}}{I_{vacuum}} \tag{2.1}$$

where I_{gas} and I_{vacuum} are the photoelectron currents in gas and vacuum, respectively [42, 68].

ε_{extr} literature shows an extensive work on this subject: theoretical (based on Monte-Carlo simulations) and experimental, performed on pure noble gases, pure organic gases (CH_4, CF_4, CO_2, N_2, etc...) and their mixtures [66, 67, 69–72] revealing that ε_{extr} depends on the gas mixture, on the reduced electric field (E/p) and on the incident photon energy [66, 73].

Nowadays, high-pressure systems incorporating solid photocathodes are one of the scientific community main interests, principally due to their application within noble gas scintillation based systems. This includes, with special relevance, possible future designs of dual phase gas detectors for dark matter search [74–78], future time projection chambers operating at high pressures such as the one used in the NEXT collaboration for neutrino-less double beta decay search [79], hard X-ray spectrometry [25], and, as in this work, future designs for medical imaging applications [28, 34].

The pressure of the gas medium is expected to act as a scale factor and the photoelectron extraction efficiency is expected to be independent from pressure when the electric field is scaled accordingly. Despite of the absence, up to this date, of any theoretical reason for a hypothetical dependence of the extraction efficiency on the gas pressure, the presumed independence was never unambiguously verified by experimental methods and the referred measurements with CsI photocathodes were done at pressures close to the atmospheric [80].

2.1.1 Experimental Setup

A stainless steel chamber with inner volume of about 90 cm^3 was designed to seal a gaseous atmosphere at high pressure and additionally allow measurements in high vacuum ($\sim 10^{-6}$ mbar). No significant gas leakage rate was registered in tests at 10 bar with Argon. A 500 nm reflective CsI photocathode layer with about 1 cm^2 area was deposited on a Cu-Ni/Au substrate coated on one surface of a Kapton® film.

The photocathode was vertically aligned with a quartz window coated with a 30 $\AA$ aluminium layer. The quartz window had a diameter of 1 cm, distanced 6 mm from the CsI film. Metallic feedthroughs, electrically isolated from the chamber body by Macor® ceramics, ensured the electrical connection to the aluminium and Cu-Ni/Au layers. A mercury vapour lamp peaking at 185±5 nm was employed to irradiate the photocathode.

By applying a sufficiently high voltage to the aluminized window while keeping the Cu-Ni/Au substrate connected to ground, the extracted photoelectrons would drift towards the window inducing an electron flow from the ground to the photocathode, thus refreshing it. A Keithley 610C electrometer connected to the Cu-Ni/Au substrate was used to measure the induced current. The aluminized window was polarized by a Caen N471A power supply [80].

Figure 2.1 shows a schematic of the setup. Argon and Xenon with purities of 99.9999% and 99.99%, respectively, were used. The Xenon underwent further purication by being forced into a U-tubing at cryogenic temperatures to condensate and retain water as well as other organic impurities. The photoelectron extraction efficiency in Argon and Xenon was measured as function of the reduced electric field (E/p). For each pressure and applied electric field, its value is given by the ratio between the induced current read in gas and the current obtained while operating in vacuum, Eq. 2.1. To avoid any significant influence of the CsI ageing [81, 82], the induced currents were measured, first in high vacuum (10^{-6} mbar) and immediately afterwards in gas by keeping the filling and measuring times short: Argon fillings took

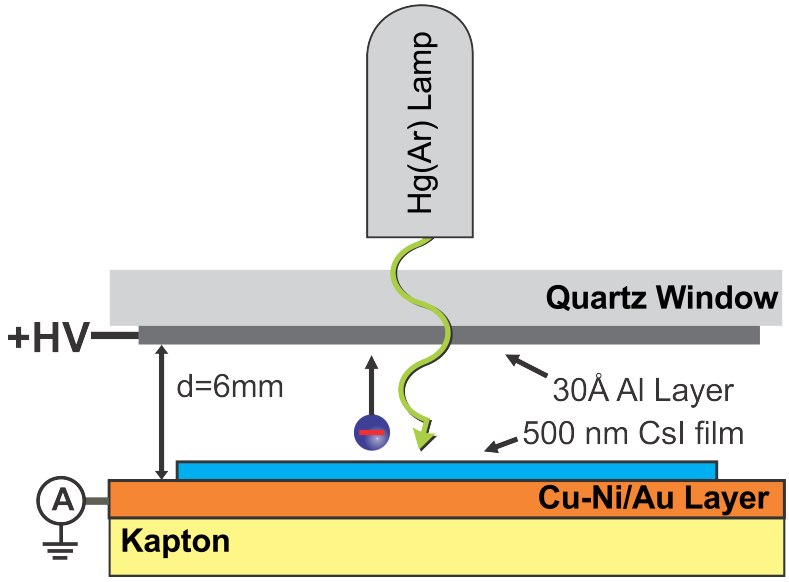

Figure 2.1: Schematic view of the experimental setup for measuring the photoelectron extraction efficiency from a CsI photocathode. Adapted from [80].

less than 1 minute; Xenon fillings lasted a few minutes; the measurements lasted typically 10 to 20 minutes. The gas was always evacuated after each measurement and new and highly pure one was used in the next measurement. This procedure is also expected to ensure the high purity of the gas without requiring a purification system, hence maintaining the simplicity of the experimental setup. To obtain each extraction efficiency curve several sets of measurements were performed in order to minimize the effect of the small fluctuations in the current readings. The pressure was controlled by a Bourdon tube gauge with 1% accuracy full span (10 bar)[80].

2.1.2 Results and discussion

Figure 2.2 shows the typical photocurrents curves as function of the drift-field, in vacuum and in gas (Ne, Ar and Xe at atmospheric pressure), measured in the previously described setup.

As observed in earlier works, the vacuum photocurrent constantly in-

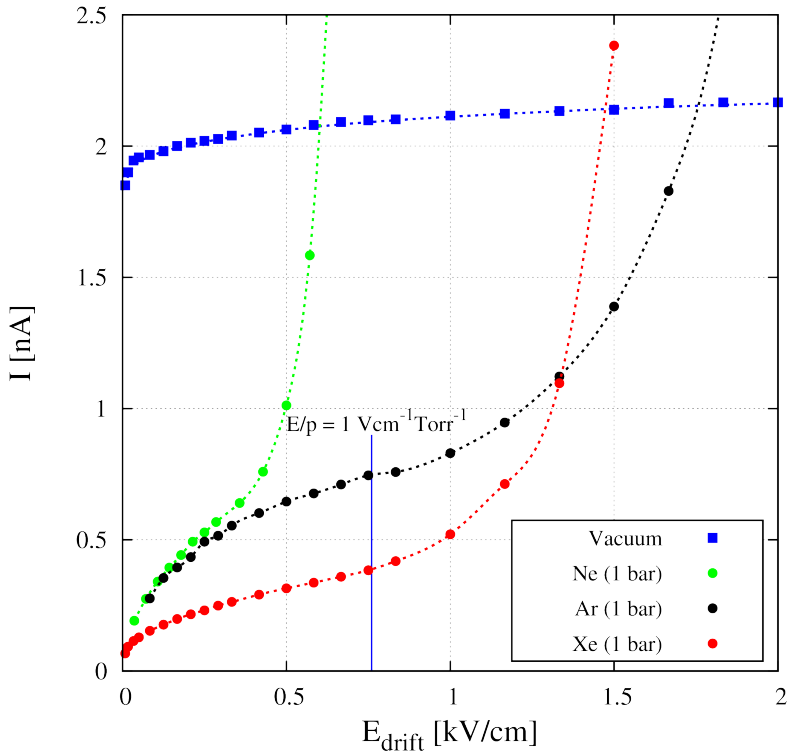

Figure 2.2: Typical photocathode currents, in vacuum and gas (Ne, Ar and Xe at 1bar), as a function of the drift field, using the photons provided by a Hg(Ar) UV lamp (185 nm peak). Dashed lines are just guides-to-the-eyes.

creases with drift field, without reaching a real plateau, presenting a QE enhancement effect with the electric field. The same QE enhancement was observed in several works as, for example [83, 84]. There is not a simple unique explanation for this effect: some authors suggest the enhancement of the photoelectron extraction probability due to a decrease of the electron work function, similar to the Schottky effect in metals (a surface phenomenon) [85, 86]. Other authors suggest including the possibility of an electric field penetration into the CsI bulk, enhancing the extraction of photoelectrons from deeper layers, i.e., a bulk phenomenon [87].

The difference between the vacuum and the gas currents is, as expected, due to the electron backscattering effect. It is possible to confirm that the backscattering effect depends on the gas being higher for Xe and lower for

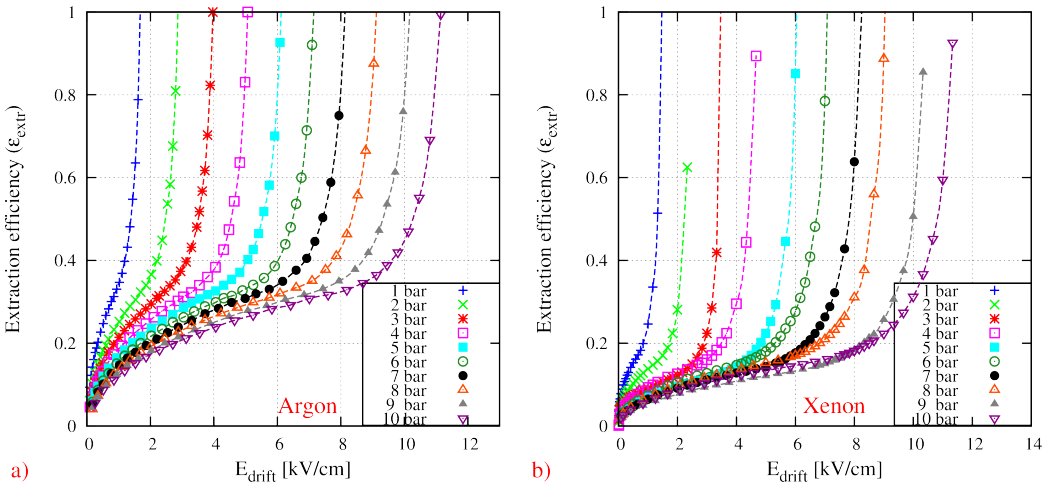

Figure 2.3: CsI photoelectron extraction efficiency as a function of the drift field for pressures between 1 and 10 bar: a) Ar ; b) Xe. Dashed lines are guides-to-the-eyes.

Ne [88].

Focusing in Ar and Xe currents, they increase with the field, up to 0.75 kV/cm, due to the well known reduction of backscattering [72, 89], and then diverge due to the onset of photon feedback [66, 72]. As soon as the reduced electric field exceeds the gas excitation threshold ($\approx 1\,\mathrm{Vcm^{-1}Torr^{-1}}$ [31]), scintillation photons start to be produced due to the photoelectrons drift. As CsI is sensitive to VUV scintillation photons produced by the noble gases (Figure 1.4), the result is a positive photon feedback. Same conclusions could be extrapolated for Ne, although the photon-feedback onset is lower as depicted in the previous figure.

In Figure 2.3 the results of ε_{extr} as a function of the drift-field for Ar and Xe, for pressures varying between 1-10 bar, are shown. In both cases, it is shown that it is possible to reach the same ε_{extr} value for all the pressures by simple increasing the drift-field. This is an important result as it demonstrates the possibility to increase the gas pressure without losing photoelectrons through backscattering effect by just increasing the electric field [80].

When the pressure increases, the collision probability between the photo-

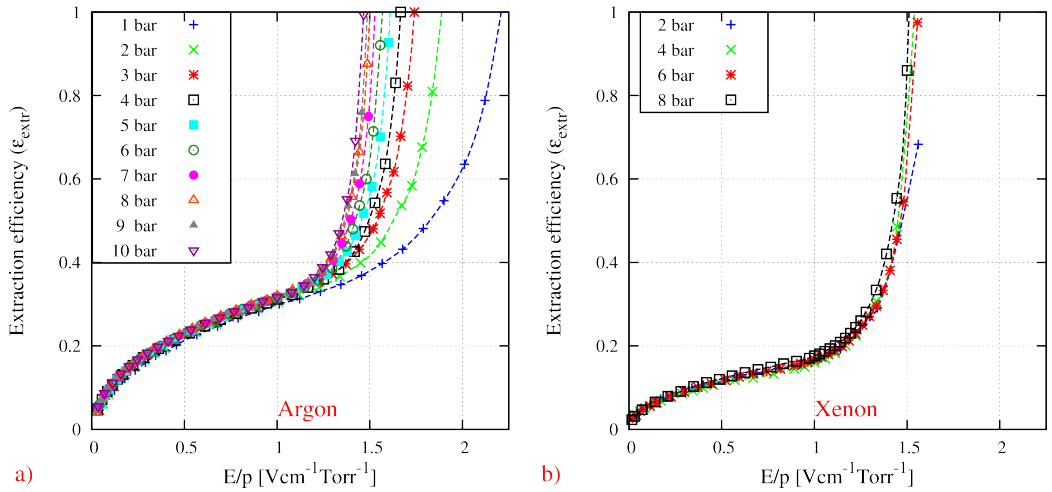

Figure 2.4: CsI photoelectron extraction efficiency as a function of the reduced electric field (E/p) for pressures between 1 and 10 bar: a) Ar ; b) Xe. Dashed lines are guides-to-the-eyes.

electrons and the gas atoms/molecules also increases, resulting on a higher backscattering effect. In order to guarantee the same ε_{extr} enhancement, the electric field must be incremented, explaining the right-shift of the curves observed in the Figure 2.3.

By comparing Figure 2.3 a) and b) it is also possible to observe that Xe presents a higher backscattering effect relatively to Ar, as expected from the literature [66, 88]. The much higher values of the ε_{extr} in Argon are attributed to the deeper penetration of the first free path of the photoelectrons, after being emitted from the photocathode and measured perpendicularly to it, which results from the lower cross-section for the elastic channel in Argon [72].

The extraction efficiency results obtained for Ar and Xe are gathered in Figure 2.4 a) and b), respectively. The curves have a similar shape, being dominated by a logarithmic-like profile at lower values of the reduced electric field ($\leq 1\,\mathrm{Vcm^{-1}Torr^{-1}}$) and starting to develop an exponential-like nature, more pronounced for higher pressures, in the proximity of E/p=1 $\mathrm{Vcm^{-1}Torr^{-1}}$. The logarithmic profile of the curves is a characteristic of the process which is predicted by the Monte-Carlo simulations indepen-

dently of the gas [69, 72].

As already explained, the exponential increase of the extraction efficiency is attributed to gas scintillation, and consequent photon feedback, which in Ar (as well as for Xe) starts at a reduced electric field of about $1\,\mathrm{Vcm^{-1}Torr^{-1}}$ [31, 66]. Nevertheless, qualitative information can be extracted from this characteristic shape. By taking into account that scintillation is very sensitive to impurities, the "clean" shape of the curves, as well as the expected faster increase for higher pressures, indicate a high gas purity.

The more pronounced increase of the curves at higher pressures is explained as follows: as the gas gets denser, the photoelectron mean free path between collisions decreases and the number of possible collisions for the same drift gap increases. Hence, if the higher amount of energy that the electron requires from the electric field to induce scintillation between collisions is guaranteed, the number of scintillation photons (produced during its drift towards the detector window) is higher and higher the number of feedback electrons generated [38, 90].

As explained in the Experimental Setup, section 2.1.1, the detector was immediately filled with gas after the photoelectron current measurement in vacuum. Argon fillings took less than 1 minute while Xenon fillings lasted few minutes, thus resulting in a higher gas contamination probability. Also, the initial gases purities are different: 99.9999% for Ar and 99.99% for Xe. This could explain why in Xe the photon feedback slopes are not so "clean" as in Ar.

Figure 2.5 presents in detail the obtained ε_{extr} on the region below the electroluminescence thresholds ($\leq 1\,\mathrm{Vcm^{-1}Torr^{-1}}$), i.e., the region where no photon feedback occurs, including results from other authors, at 1 bar. Focusing in our measurements, the registered discrepancies are smaller than 2% of the absolute values of the efficiencies. In Argon, persistent lower values for the ε_{extr} are observed for 1 bar (more accentuated) and 2 bar. In fact, by removing these data the discrepancies would reach a value as low as 0.8% of the absolute values of the efficiencies. In principle, such effect cannot be

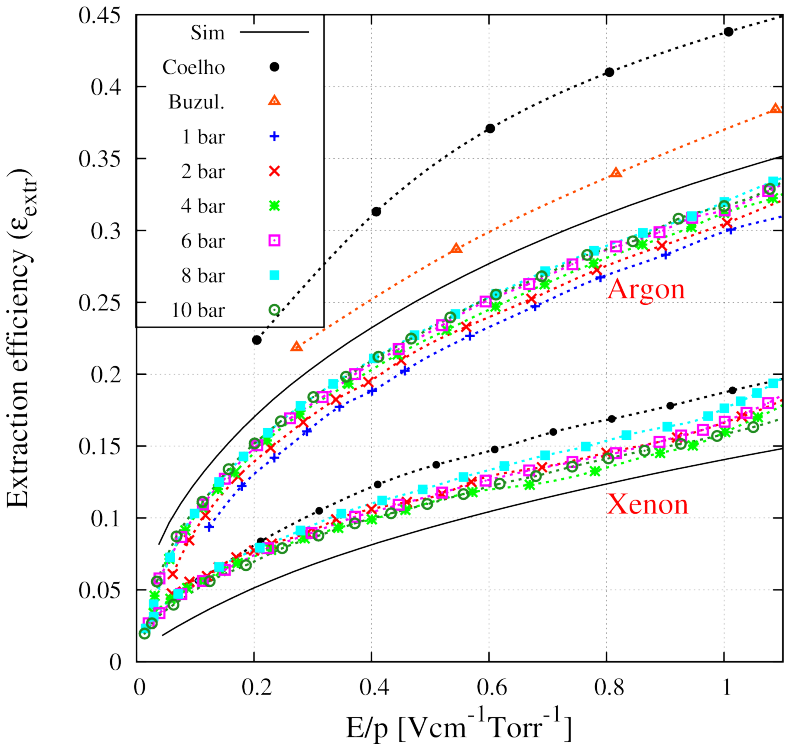

Figure 2.5: CsI photoelectron extraction efficiency as function of E/p in Ar and Xe for 1 (only Ar), 2, 4, 6, 8, and 10 bar. Results from other authors are depicted as well for comparison: experimental at 1 bar [68, 71] and Monte Carlo simulations [69, 72]. The dashed lines are guides-to-the-eyes.

attributed to the presence of impurities as the shape of the efficiency curves above the electroluminescence threshold point to a gaseous atmosphere in very pure condition. Therefore, this outcome may be related to some systematic effect not accounted [80].

Apart from the results for Ar from Coelho [71], the agreement with the experimental results obtained by other authors [68] is also acceptable by considering experimental errors and/or the different levels of gas purity in each experiment. In fact, when comparing the results from Coelho for Ar, with the extraction efficiency curve calculated via Monte-Carlo techniques the higher values obtained experimentally may indicate a purity problem, which seems to be better under control in these measurements.

Moreover, it is evident from Figure 2.5 that the ε_{extr} curves measured

within this work and the ones obtained via Monte Carlo simulation follow the same profile and agree within an average discrepancy of about 3% and 2.5% of the absolute values of the efficiencies for Ar and Xe, respectively. Furthermore, the average values of 31.4% and 16.5% measured for the ε_{extr} at E/p=1 Vcm^{-1}Torr^{-1} for Ar and Xe, respectively, are in fair agreement with the ones calculated via simulation [69, 72]: 34.7% and 14.3%.

As a result, it can safely be stated that, within a 2% uncertainty of the absolute values of the efficiency, the photoelectron extraction efficiency from CsI photocathodes in Ar and Xe is independent from the pressure when scaling the electric field accordingly.

2.1.3 Conclusions

The photoelectron extraction efficiency from a CsI photocathode as function of the reduced electric field has been successfully measured for the first time at pressures above 1 bar for Ar and Xe. It was independently shown for each gas that the extraction efficiency curves have a common profile which is basically the one calculated by Monte-Carlo techniques. On top of that, the results are in agreement with other authors.

The average values of 31.4% and 16.5% were measured for the ε_{extr} at E/p=1 Vcm^{-1}Torr^{-1} for Ar and Xe, respectively.

Finally, by comparing the measured curves the independence of the photoelectron extraction efficiency from the pressure is unambiguous. It should be stressed that, although it was an expected result, it was never validated by experiment up to now.

2.2 F2F vertical interaction position linearity and energy resolution

The idea of using 2 photosensors positioned face-to-face is related with 2 facts: first, to increase the detector signal amplitude (by summing both

signals) and improve the energy resolution; second, to determine the event interaction position, i.e., the interaction point in the direction perpendicular to the photosensors planes. This position information, combined with the 2D information of the photosensors, will give the 3 dimensional (3D) information of the interaction point in the detector. The 3D information will allow the development of correction methods for the solid angle variation between the interaction position and the photosensors, responsible for the lack of energy resolution and position correction as predicted by simulation [28] and observed in previous works [22].

2.2.1 Experimental Setup

In order to study the linearity of the position response and its resolution, an experimental apparatus as the one presented in Figure 2.6 was used. In this study, for sake of simplicity, the photosensors used were not the CsI-2D-MHSP, but the CsI-MHSP. The main difference between them is that the second ones have a conductive line interconnecting the strips (instead of a resistive layer) discarding the 2D position discrimination [20]. With this simpler photosensors we just use 1 pre-amplifier per photosensor (instead of 4 pre-amplifiers) and we do not need to compute the sum of the anodes charges as the full charge will be collected on a single pre-amplifier.

In this experiment, all MHSP electrodes were biased independently through CAEN N471A power supplies, with RC low pass filters, R=15 MΩ, C=1 nF (except the anode electrode, feed trough the pre-amplifier). The photosensors charge signals were pre-amplified using two Canberra 2006 pre-amplifiers (sensitivity of 1.5 V/pC). Using two channels from a CAEN digitizer N1728 (4-channel, 14 bit, 100 MHz ADC) the signals from both pre-amplifiers were digitized. Digital pulse shaping was performed applying the Jordanov trapezoid algorithm [91] to determine the signal amplitudes, $A1$ and $A2$, from the photosensors and the amplitudes were registered with the respective time stamp in a file.

The voltages on each photosensor were adjusted in order to have approxi-

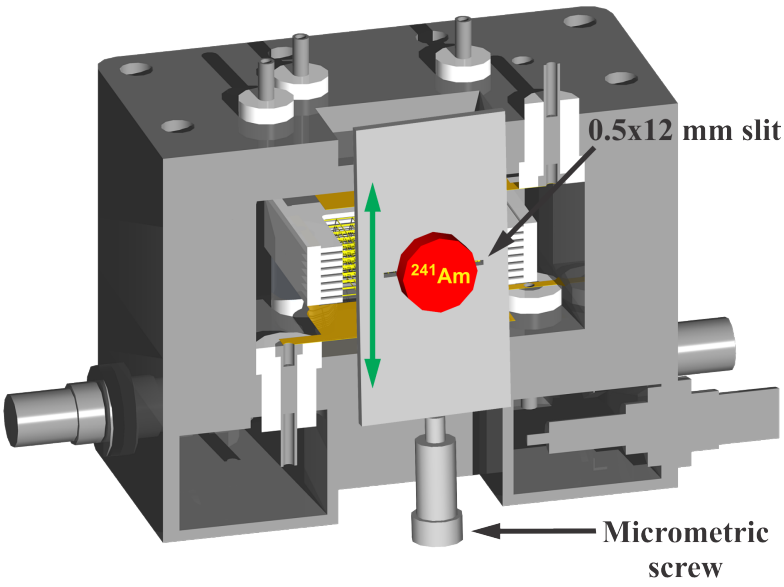

Figure 2.6: Schematic view of the experimental apparatus showing the radiation source position relatively to the detector.

mately the same gain on both photosensors. The reduced electric field in the scintillation gaps, was set at about 6 $\mathrm{Vcm^{-1}Torr^{-1}}$. On the drift region, optimal electric field values were found and established in order to have the best photoelectron extraction/collection efficiency (see method in section 2.3.2). This technique also allows discarding events interacting on the drift regions, as the optimal electric field is slightly reversed, forbidding the multiplication of the primary electron clouds.

The detector was filled with 1 and 2 bar Xe and irradiated using 59.6 keV γ-rays from a ^{241}Am source, collimated with a 0.5×12 mm lead slit. The source and collimator position were moved, using a micrometric screw, along the perpendicular direction to the photosensors in 250 or 500 μm steps, for 1 and 2 bar, respectively, up to a distance of -4.5 to 4.5 mm relative to the center of the cluster grids.

Total pulse amplitude was obtained by adding the amplitude contributions $A1$ and $A2$ of the shared light for each event. The vertical position, Z, orthogonal to the detector window, can be determined by weighting the light sharing on the photosensors:

$$Z = k\frac{A1 - A2}{A1 + A2} \tag{2.2}$$

where k represents a calibration constant. A Gaussian function was fitted to the obtained interaction position distribution, Z (centroid) and the position resolution (FWHM).

2.2.2 Results and discussion

In Figure 2.7 the vertical interaction position distribution is depicted as a function of the detected energy, when the entire detector gas volume was irradiated with 59.6 keV γ-rays. The meshes position can be clearly distinguished in the figure: the outer meshes are +V meshes while the next ones and central meshes are the negative high voltage (-HV).

We can observe that the detected amplitude is higher when the interactions occur near the outer meshes comparing with the interactions occurring on the detector center. This effect is due to the larger solid angle variation subtended by the CsI-MHSP photosensors and the photon transmission by the meshes. An event interacting near the photosensor will have a higher number of photons striking the photocathode due to a higher solid angle and to a decrease on the VUV photons absorbed by the meshes.

By analysing the energy *vs* position profile we can note that, the events interacting near the -HV meshes present a higher amplitude relatively to the events interacting near the +V meshes. This effect is due to a dependence of the number of produced VUV photons with the interaction position. From eq. 1.6, N_{TfUV}, the number of scintillation photons per primary electron is dependent on ΔV, the voltage difference between the consecutive meshes and on Q_c, the scintillation efficiency relatively to the E/p [38]. This is true when the electrons have the same drift distance. As the primary electron clouds have different drift distances, the number of produced VUV photons varies accordingly, presenting the typical driftless detector behaviour [36, 92]. This is clear when events interacting near the -HV meshes have higher amplitudes

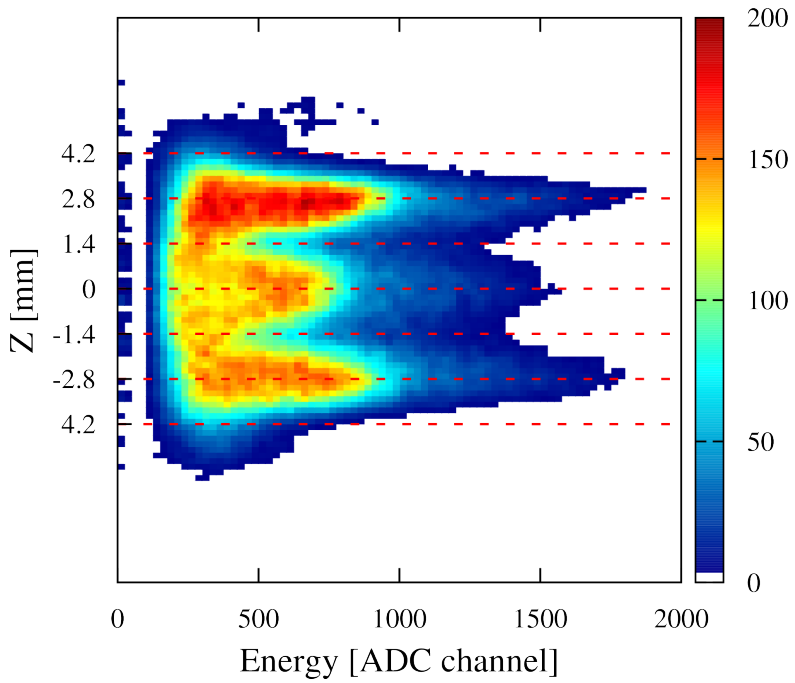

Figure 2.7: Vertical interaction positions distribution of the full irradiated detector for 1 bar Xe.

relatively to those occurring near the +V meshes. A higher distance to drift towards the +V mesh leads to a higher number of produced scintillation photons and thus to a higher photosensor signal amplitude.

This difference in the signal amplitude is expected to degrade the energy resolution, as clearly seen in Figure 2.10, leading to the need for a correction algorithm based on the position interaction point or using the so called drift-less technique [39, 92]. In this technique, the use of very short linear amplifier shaping-time constants (∼50 ns) enables pulse shapes to closely represent the scintillation light-pulse time-profile, resulting on a maximum achieved value which is dependent only on the number of primary electrons.

As described, a 0.5×12 mm slit and a micrometric screw were used to change the ^{241}Am source position relatively to the perpendicular direction of the photosensors. The results of the measured detector vertical position (Z) and its deviation from the slit position (real position), for 1 and 2 bar, are presented in Figure 2.8. Good linearity between real and measured positions

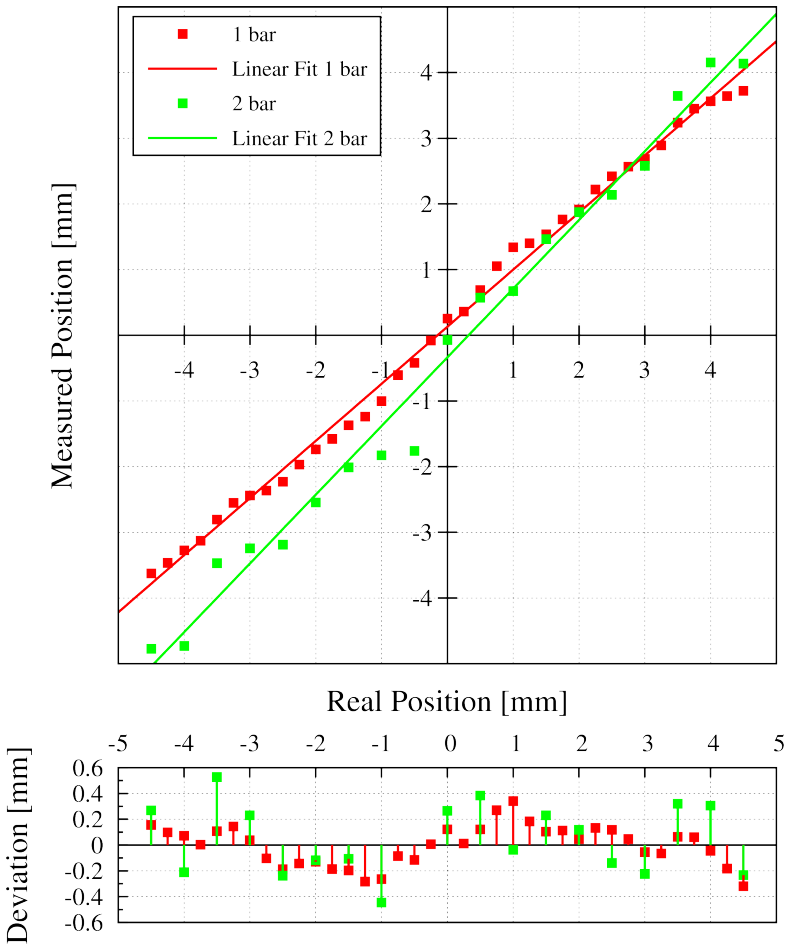

Figure 2.8: Measured position and its deviation as a function of the real position for 1 and 2 bar Xe: (250 and 500 μm pitch, respectively).

can be observed, presenting maximum deviations below 350 μm and 500 μm for 1 and 2 bar Xe, respectively. This is an important result as it shows the possibility to determine with accuracy the interaction position in the direction perpendicular to the photosensors planes, opening the possibility for performing corrections on the 2D detector response, namely the correction of the number of photoelectrons and the correction of the solid angle variation, thereby improving the energy resolution and the image performance on the detectors borders [28, 40].

The highest maximum deviation was reached for 2 bar. This difference is

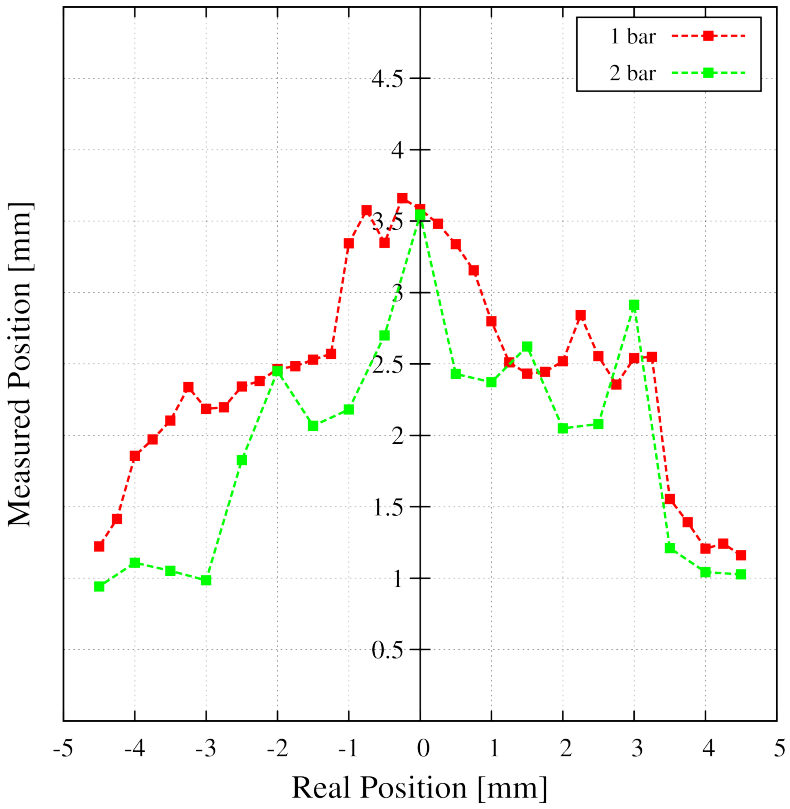

Figure 2.9: Position resolution of the measured position as function of the real position for 1 and 2 bar Xe: (250 and 500 μm step, respectively). Dashed lines are guides-to-the-eyes.

due to the low gain achieved in the CsI-MHSPs during the measurements, resulting in a lower signal-to-noise ratio (SNR), and of course a worse precision in the position calculation. The low gain, in this case, was due to defects in both MHSPs that have reached the discharge limit to soon, thus limiting the avalanche multiplication.

The different slopes and the 2 bar offset are due to different gain conditions of the 2 photosensors, which will produce an error on the position calculation, i.e., when the photosensors have different gains this results in a shift on the detected position in the direction of the photosensor operating at higher gain.

In Figure 2.9, position resolution (which corresponds to the LSF FWHM) as a function of interaction position is depicted. Despite the marginal po-

sition resolution achieved in the detector center, improvement was observed when moving to the borders. This phenomenon is again due to the solid angle variation and mesh photon transparency (responsible for the steps related to the mesh position, see Figure 2.7). When the interaction position approaches one of the photosensors, the scintillation light collected increases, resulting in higher photoelectron statistics and, consequently, in better position calculation [22]. The position resolution value in the extremities is of about 1 mm.

A slight improvement of the position resolution is achieved by going from 1 to 2 bar. We believe this improvement is due to a combination between the higher confinement of the primary electron cloud and a lower electron diffusion with the increasing pressure.

Figure 2.10 presents the signal amplitude distribution of the detector response for 1, 2 and 2.5 bar Xe when irradiated using a ϕ=1 mm lead collimator. Although the marginal energy resolution of the raw spectra, i.e., the spectra without any correction of the position interaction, an improvement is observed for pressures higher than the atmospheric pressure. We believe that this fact is related with the spatial dimension of the primary electron cloud at the atmospheric pressure, which could be much larger than the distance between the meshes, meaning that some of the electrons will be spread to the neighbouring scintillation regions and will add another fluctuation in the process, degrading the energy resolution. The simulation of the primary electron cloud distribution and the operation of the F2F at higher pressures will clarify this behaviour [22].

2.2.3 Conclusions

By fully irradiating the detector we have observed a dependence of the response amplitude with the interaction position. This is due to a different number of detected scintillation photons produced per event. Nevertheless, the good position linearity response (250 μm and 500 μm) opens the possibility to develop a correction method based on the interaction position.

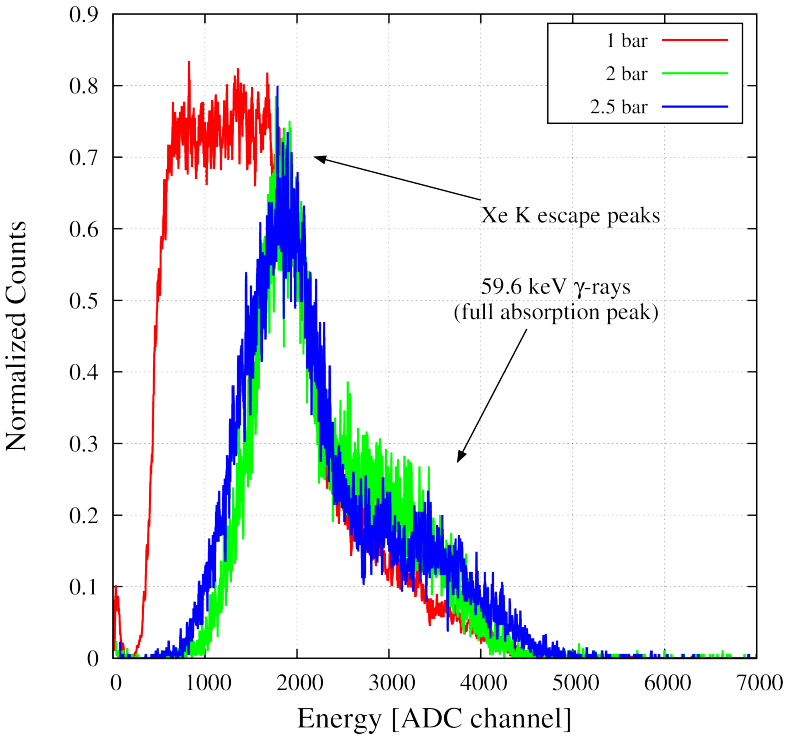

Figure 2.10: Normalized energy distribution of the detector response for 1 bar, 2 bar and 2.5 bar Xe, by adding the contributions of the 2 photosensors. In order to simplify the view the data was smoothed with a 5 points moving average function.

A maximum value for position resolution of about 3.5 mm was measured at the center of the scintillation regions, improving towards the borders, where it reaches the 1 mm value.

The energy resolution improves with the increase of Xe pressure. Increasing the Xe pressure reduces the dimensions of the primary electron clouds, resulting in better detector energy and position resolutions, as a result of the primary electron confinement.

2.3 2D-GSPC Imaging system

In order to study the 2D position and the energy resolution performances, a simpler detector configuration was used. For sake of simplicity we chose to use a well studied detector configuration: the Gas Scintillation Proportional Counter (GSPC) [34, 93–95]. In principle, this configuration will not influence the 2D position performance of a single CsI-2D-MHSP, as it will only be used to produce the VUV photons. Another advantage, besides the construction simplicity (just 3 meshes are used) and knowledge about the system, is its energy resolution (below 4% for 59.6 keV with a PMT [95] or a Micro Strip Gas Counter (MSGC) readout [25], both using Xe), that will allow the study of the 2D-CsI-MHSP photosensor energy resolution.

2.3.1 Experimental Setup

The GSPC schematics, using a CsI-2D-MHSP as the light readout, is presented in Figure 2.11. 3 stainless steel meshes (wire diameter ϕ=80 μm and pitch=900 μm) were used in order to define the radiation absorption region (10.7 mm), the scintillation region (1.9 mm) and the photoelectron drift region (4 mm). A 500 nm CsI film was evaporated directly onto the top electrode of the 2D-MHSP and the detector was filled with various pressures of Xenon, ranging from 1 to 3 bar being continuously purified through ST707/WASHER/833 SAES getters.

The charge signals from the CsI-2D-MHSP were integrated by four Canberra 2006 pre-amplifiers, connected to the four ends of the resistive lines. Using a NIM digitizer module N1728 from CAEN, the signals were digitally shaped and amplified by applying the Jordanov trapezoid algorithm to determine the signal amplitudes from each pre-amplifier.

For image acquisition, a lead collimator with 5 holes (ϕ=1 mm) distanced by 8 mm, was placed on the detector window. 59.6 keV γ-photons were provided by an ^{241}Am source, positioned about 50 cm away from the collimator.

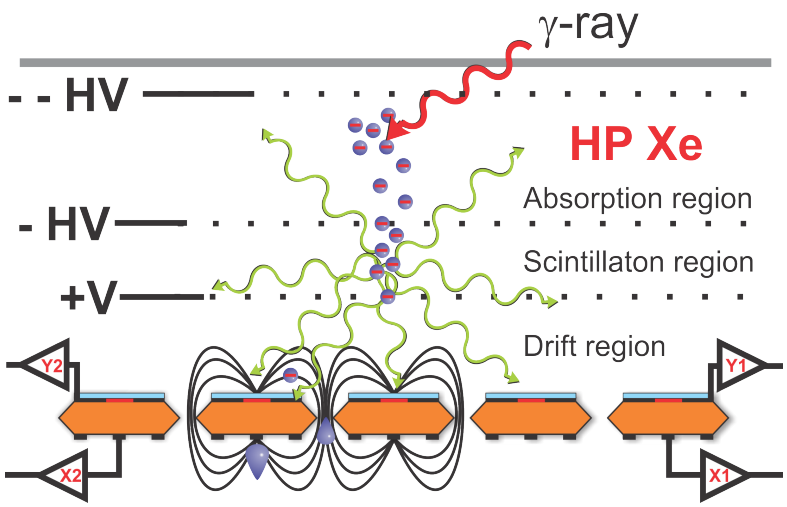

Figure 2.11: Schematic view of the GSPC detector configuration, using a 2D-CsI-MHSP photosensor.

2.3.2 Signal amplitude and energy resolution as a function of the drift-field

Before the image acquisition studies, a simple initial verification of the pulse amplitude and energy resolution of the CsI-2D-MHSP was performed. The setup was identical to the above presented except just for the use of one pre-amplifier on the anode strips (in order to fully collect the multiplied charge on a single pre-amplifier) at a gas pressure of 1 bar. The signal amplitude and energy resolution were measured as a function of the electric-field in the photoelectron drift region.

The electric field in the photoelectron drift region should be carefully set through the adjustment of the voltage in the +V mesh. Voltages higher than the optimal value will drift the photoelectrons to the mesh decreasing the single photoelectron collection efficiency. Lower voltage than the optimal value will result in a poor photoelectron extraction efficiency. Also, the primary electron clouds produced in the photoelectron drift region will be multiplied by the 2D-MHSP.

The main problem of the primary charge multiplication produced in the photoelectron drift region is that, depending on the system configuration,

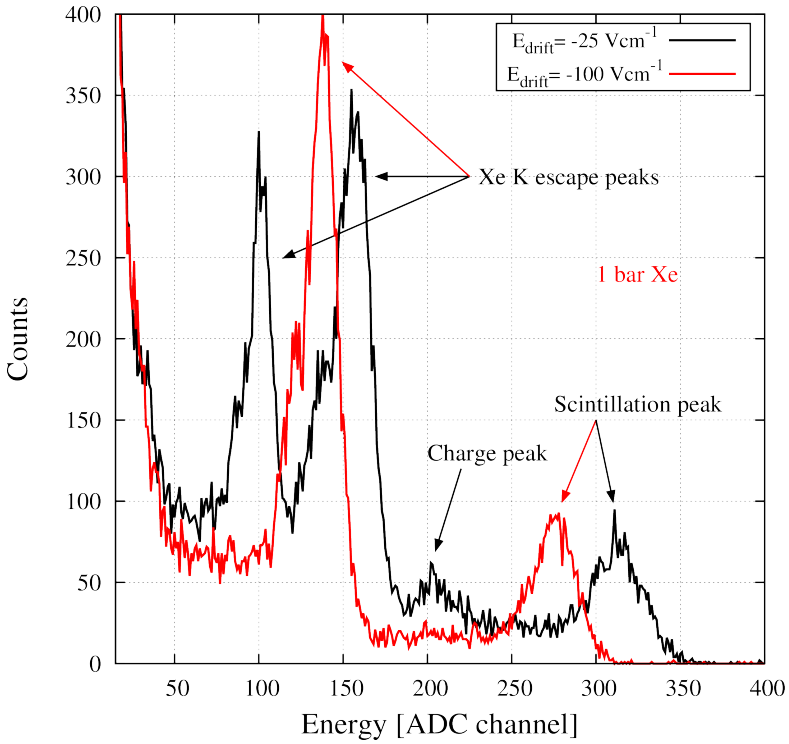

Figure 2.12: Pulse-heigh distribution obtained for -25 Vcm^{-1} and -100 Vcm^{-1} electric fields in the photoelectron drift region.

the charge signal may have an amplitude near to the photoelectrons signal, mixing the events and thus degrading the system energy resolution, as shown in Figure 2.12.

In Figure 2.12, an example of the above mentioned phenomenon is presented: 2 pulse-height distributions are presented for 2 different voltages between the +V mesh and the CsI-2D-MHSP top electrode. With E_{drift}=-25 Vcm^{-1}, the spectrum appears as a duplicated-like, with 2 total absorption peaks and also 2 Xe K escape peaks. We have found that the duplicated peaks, i.e., the lowest amplitude peaks, correspond to the primary charge produced in the drift region. It is strange to observe the drift of the primary charge with a reversed electric field. Nevertheless, the need for this reversed field is due to the effect of the scintillation electric field penetration into the photoelectron drift region [25, 20].

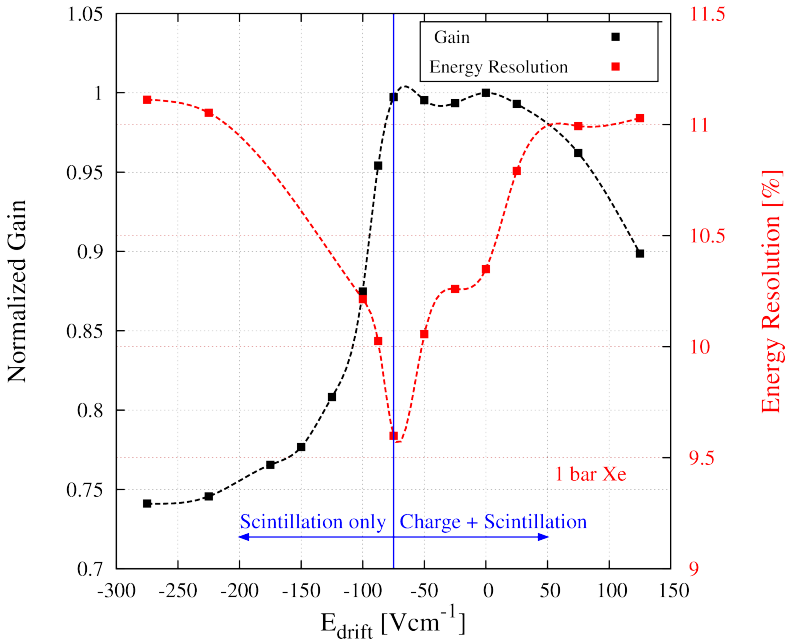

Figure 2.13: Scintillation peak relative amplitude variation and energy resolution as a function of the electric field in the photoelectron drift region. Dashed lines are guides-to-the-eyes.

The light gain can be estimated through the relative position of the duplicated peaks, i. e., the number of detected photoelectrons per primary electron. In the case of the E_{drift}=-25 $\mathrm{Vcm^{-1}}$ spectrum, by normalizing the scintillation peak to the charge peak we obtain a light gain value of approximately 1.5, demonstrating the concept of the scintillation light amplification. The simplicity of this calculation should be interpreted carefully, as it only gives an estimation, not a precise value. For example, to have a full collection of the primary charge, a higher value of drift field should be used. But the electric field will not be favourable to the photoelectron extraction. On the opposite electric field direction, the photoelectron extraction will increase but the primary electrons, and also the photoelectrons, will not be focused into the CsI-2D-MHSP holes, therefore decreasing the signals amplitude (for precise measurements of the light gain, another method should be used [28]).

In Figure 2.13 are depicted the results for the scintillation pulse signal amplitude and its energy resolution (estimated through the centroid

and FWHM of a Gaussian fit to the full absorption peak) as a function of E_{drift}. Two regions can be considered: "scintillation only" region (from -275 $\mathrm{Vcm^{-1}}$ to -75 $\mathrm{Vcm^{-1}}$) and "charge + scintillation" region (from -75 $\mathrm{Vcm^{-1}}$ to 125 $\mathrm{Vcm^{-1}}$). The first corresponds to E_{drift} where no primary charge is collected while the second one corresponds to the case of the duplicated spectra, where both charge and scintillation signals are present (see Figure 2.12, E_{drift}=-25 $\mathrm{Vcm^{-1}}$).

Starting the figure analysis from E_{drift}=125 $\mathrm{Vcm^{-1}}$ (in the direction of the negative values), the scintillation signal will increase until it reaches a plateau. This increase is due to the electric field approaching the optimal value. In this region, the electric field is in the opposite direction to the photoelectron extraction benefit; as soon as the electric drift field approaches the optimal value, the number of extracted photoelectrons and, of course, the pulse signal amplitude will increase. As the 2D-MHSP gain was kept constant we can conclude that the normalized gain variation is a direct reflection of the photoelectron extraction efficiency. The result of the photoelectron extraction increase is the improvement of the energy resolution.

After the optimal value (-75 $\mathrm{Vcm^{-1}}$, coincident with [20, 25]) only one total absorption peak is observed, while the signal amplitude has a sudden decrease. This decrease with the electric field is explained by the drift of photoelectrons towards the +V mesh instead of the CsI-2D-MHSP holes. Obviously, the decrease on the number of detected photoelectrons leads to the degradation of the energy resolution value.

The drift-field was carefully monitored and set for each pressure. As the present method takes a long time to perform, a simpler visual method, based on the signals shape was used: starting with a positive E_{drift}, the photosensor signals were monitored in an oscilloscope, while reducing the electric field. The electric-field reversing voltage is clearly identified by the presence of long flat signals corresponding to the poor primary charge drift (electric field close to 0 V). After that, a fast amplitude increase of the photoelectrons signal is observed due to the increase of the photoelectron extraction efficiency.

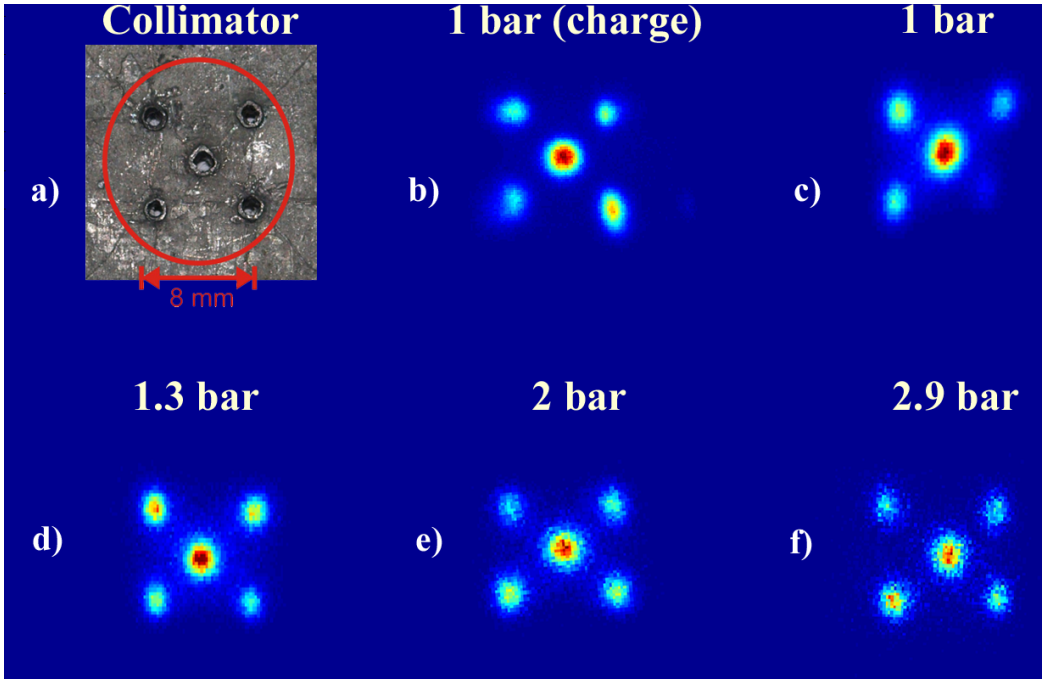

Figure 2.14: Image results for several detector gas pressure, using only the 59.6 keV total absorption peak, from the ^{241}Am source.

2.3.3 Image capability and image quality

In order to study the system imaging capability, several images were acquired for Xe pressures between 1 and 3 bar. Some examples of the acquired images are plotted in Figure 2.14.

Image quality is a subjective expression that connotes the observer's reaction to the clarity of information in the image. The clarity of information in a medical image is a measure of how well the image expresses the information about the patient. If the information is blurred or distorted, or if the image lacks contrast or is too noisy, the clarity is compromised and the information is less helpful [96].

Generally the imaging systems performance is evaluated through a quantitative parameter: the spatial resolution. It looks simple but, unfortunately, a single and unambiguous parameter is not always sufficient to characterize all the subtle aspects of image quality [97]. Also, in the literature, there are

several approaches to achieve the position resolution of a system. It could be estimated through the Point Spread Function (PSF), the Line Spread Function (LSF) or even the Edge Spread Function (ESF) [96–98].

The PSF contains the complete information about the spatial resolution. To express the spatial resolution by a single number, the most common way is to use the Full-Width-at-Half-Maximum (FWHM) value of the PSF. Unfortunately, this method has two significant drawbacks. First, it does not match other measures of spatial resolution, including the subjective judgement of observers viewing the images. Second, it is usually very difficult to directly measure the PSF as it is impractical to irradiate a detector with a point-like source.

Like the PSF, the LSF is also difficult to measure, as it is defined as the detector's response to a single line. However, the LSF can be easily calculated through the ESF (the detector's response to a sharp straight discontinuity (an edge)) by taking its derivative, as a line is the derivative (or first differential) of an edge.

The most simple way to achieve the position resolution of a system is through a simple parameter: the distance required for the edge response to rise from 10% to 90%. There are many advantages on using the edge response for measuring resolution. The edge response is simple to measure because edges are easy to generate in images. Also, common edge responses have a similar shape, so, the 10%-90% distance is an excellent single parameter measure of resolution [97].

The position resolution does not determine the minimum size of the objects that can be visualised in an image. In reality, what determines if objects can be distinguished or not, is much more complex and is related to the contrast of the image and distortion, besides their size. So, in order to describe an imaging system another parameter is often used, the Modulation Transfer Function (MTF): the fraction (or percentage) of an object contrast that is recorded by the imaging system, as a function of the size (i.e., spatial frequency) of the object [98].

Another advantage of using the method here described for the determination of position resolution is that the MTF can be found directly by taking the one-dimensional FFT of the LSF (unlike the PSF to MTF calculation that must use a two-dimensional Fourier transform) [97].

2.3.3.1 Position resolution calculation method

In order to calculate the position resolution (10-90% ESF) and the MTF of the acquired images, some considerations and approximations were performed. Starting from the raw image, the first consideration is to select just the high amplitude events on the energy spectrum, i.e., events belonging to the total absorption peak of the 59.6 keV photons from the ^{241}Am, Figure 2.15 a), red area. An example of the resulting reconstructed image is depicted in Figure 2.15 b).

The next step is to take a "thin slice" (corresponding to the area in the red square in Figure 2.15 b)) from the image and make its projection for both X and Y directions. This projection is in approximation an irradiated edge, which is then used for the ESF and position resolution calculation.

We decided to use the top-left-hole in order to take the projection edges. The central hole is not a good option as it presents several events in its vicinity (due to the proximity of other holes, background or secondary effects) contributing to a non-regular shape of the ESF, making it difficult to apply the presented method.

The spectrum presented in Figure 2.15 a) corresponds to the events inside the red rectangle in Figure 2.15 b).

Figure 2.16 is an example of a ESF profile obtained by projecting the "slice" (blue dots). Red line represents a fitted function which models the ESF with adequate accuracy. The empirical model function used is given by the following equation:

$$\mathrm{ESF}(x) = a_0 + \frac{a_1}{1 + \exp(-a_2(x - a_3))} \tag{2.3}$$

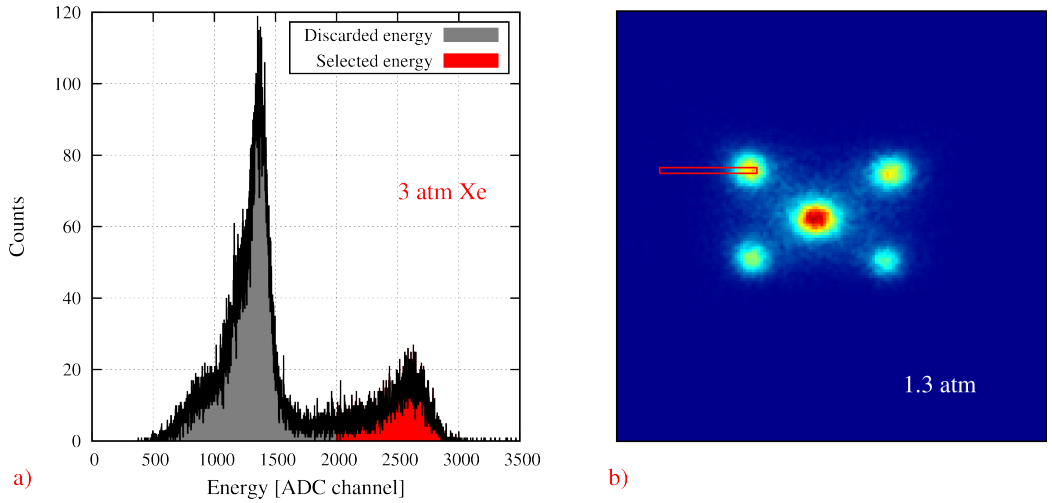

Figure 2.15: a) Pulse height distribution obtained at 3 bar Xe,identifying the energy ROI for the image reconstruction; b) Example of a reconstructed image by choosing only the events of the total absorption peak for 59.6 keV photons. Red rectangle represents the events which are used to make the projection and posterior calculations (10-90% ESF and MTF).

where a_0 is related to the X-ray transmission by an object, a_1 is the brightness of the fully irradiated sensitive area, a_2 is the steepness of the edge function (related to the spatial resolution of the imaging system) and finally a_3 is the centroid of the edge function [99, 100].

As expected, the acquired ESF profile does not present a top plateau as it was obtained from a hole. This fact is a major issue when trying to fit the empirical model: it fails. Nevertheless, if an approximation is performed, by adding some points to the ESF corresponding to its maximum value (purple dots), a good fit is achieved as depicted in the figure.

The plots in Figure 2.17 a) are examples of the LSF obtained from the ESF fitted model differentiation (blue dots) and the corresponding Gaussian fit (red line). The obtained MTF, by applying the FFT to the LSF function, is depicted in Figure 2.17 b).

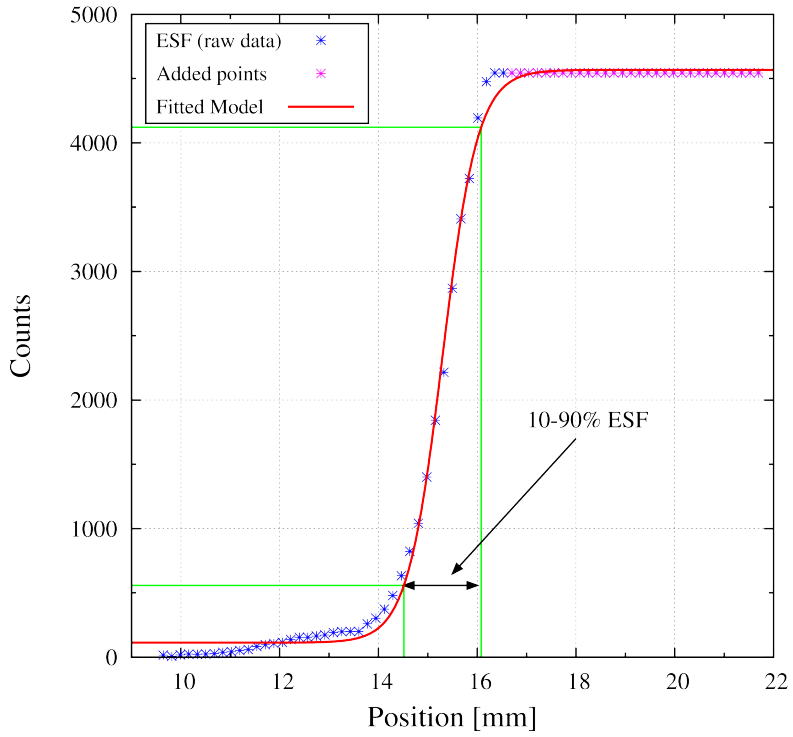

Figure 2.16: Example of an acquired edge spread function (ESF) along the X coordinate (blue dots). The purple dots are the added data in order to use the model. The red curve is a fit with a suitable model function. Green lines are representing the values for 10 and 90% of the ESF.

2.3.3.2 Results and discussion

The position resolution (10-90% ESF value) obtained for Xe pressures varying from 1 to 3 bar is depicted in Figure 2.18. As expected, the position resolution in X and Y directions is not the same, being better for the X direction. The X direction was taken from the CsI-2D-MHSP anode electrode, where the full charge was collected, while the Y direction was taken from the top electrode, where the charge is induced and the signal has typically 40-60% of the amplitude when compared to the anode signal [30, 58]. This fact results in a lower SNR, thus resulting in a slightly worse position resolution.

The main limitation of the position resolution in noble gas detectors is the size of the primary electron cloud [18, 101, 102], which for a 50 keV electron in Xe at atmospheric pressure, should be about 1 mm [103]. By

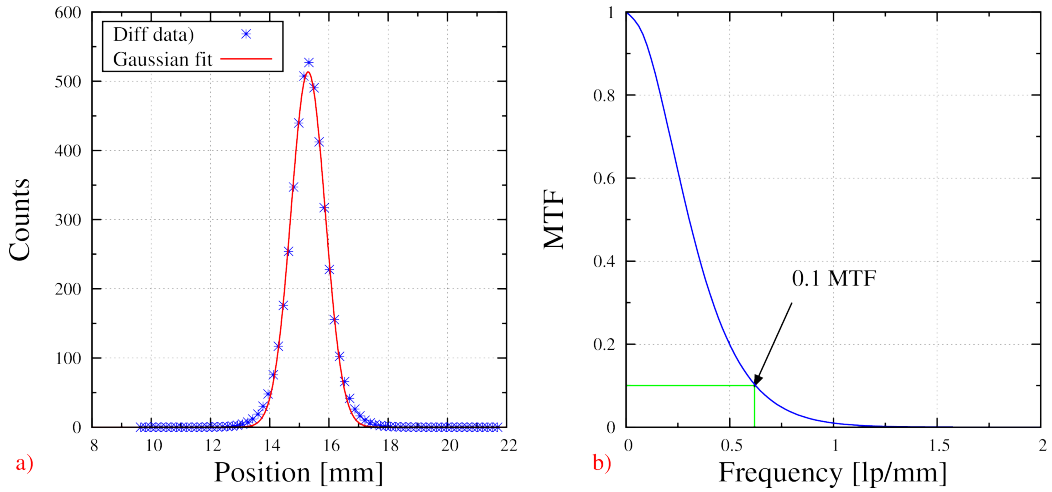

Figure 2.17: LSF determination from the ESF differentiation (a) and the corresponding MTF (b).

considering this value and comparing it with our measured value for 1 bar (≈1.3 mm) we can infer that this effect has a significant contribution to the obtained position resolution, demonstrating the good performance of the imaging system, namely the CsI-2D-MHSP.

The position resolution should benefit with the increasing pressure as the primary cloud size decreases for the same energy [104]. This behaviour is not directly reflected in the results, where the position resolutions have practically the same value (around 1.2 mm for the X direction) and some fluctuation in the case of the Y direction, probably due to the contribution of the different SNR. This non-significant improvement of the position resolution value with the pressure is explained by the decrease of the detector gain with the pressure (see Figure 2.5), thus degrading the position resolution value [58, 105].

Figure 2.19 presents the MFT profiles of the analysed images, showing that higher spatial frequencies are reduced in amplitude. The value of the MTF is maximum for low spatial frequencies, signifying that the imaging system reproduces low frequencies without distortion or loss of resolution. As the frequency increases, the MTF decreases approaching zero, signifying

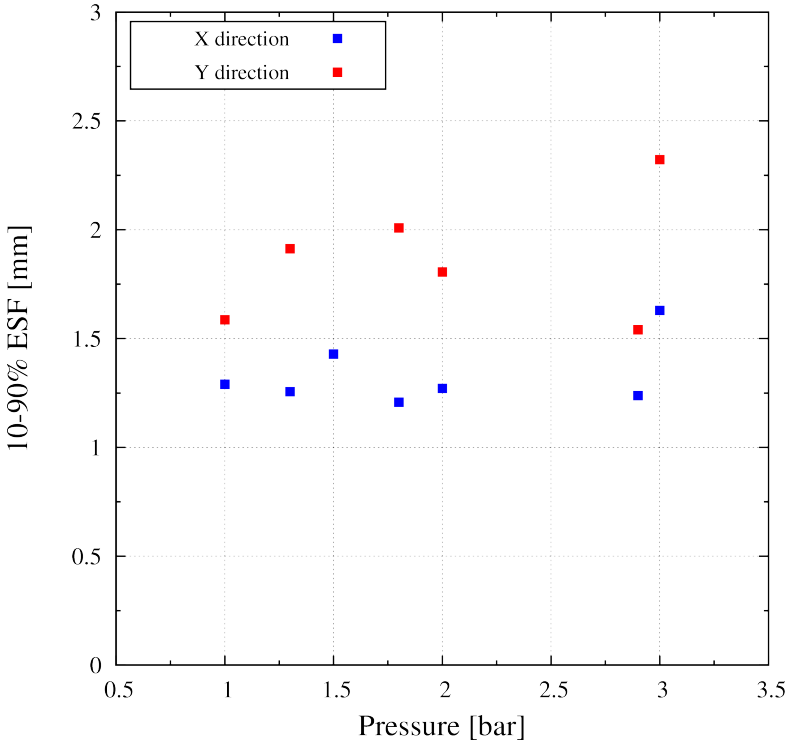

Figure 2.18: Position resolution (10-90% ESF) for Xe pressures from 1 to 3 bar.

that the spatial frequencies are so high that the imaging system provides no reproduction at all, resulting in a blurred image at high frequencies [96].

The MTF profiles are used to define the system limiting resolution, generally specified as the frequency when MFT is reduced to 3%, 5% or 10% (depending on the manufacturer chosen value). The limiting resolution is a vague term related to the human eye ability to distinguish the low contrast difference between the peaks and valleys in the presence of image noise. The objects will be distinguishable in the image as long as the MTF amplitude is greater than about 3% to 10% of the original height [97].

Converting the limiting resolution (10% contrast) to 10-90% ESF value is as easy as inverting the values:

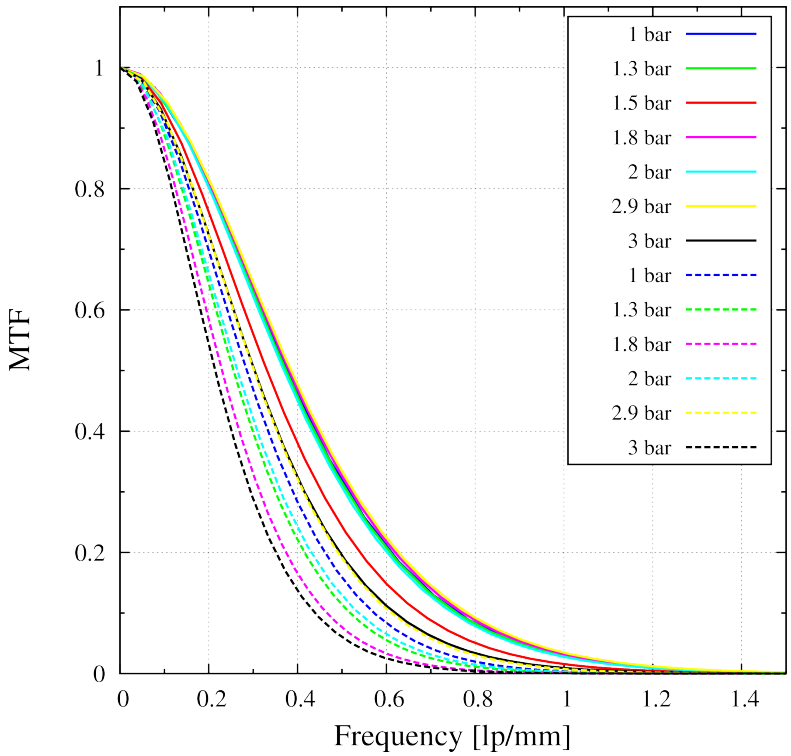

Figure 2.19: MTF profiles for the acquired images at pressures varying from 1 to 3 bar, for the X (solid lines) and Y (dashed lines) directions.

$$10-90\%\mathrm{ESF}(mm) = \frac{1}{limiting\,resolution(10\%\,contrast)(lp/mm)} \tag{2.4}$$

For example, lets take the limiting resolution extreme values: 0.46 lp/mm and 0.78 lp/mm, for 3 bar Y and 2.9 bar X. By inverting, we obtain 10-90% ESF values of approximately 2.2 mm and 1.3 mm, values which are in agreement with the measured ones in Figure 2.18.

2.3.4 Detector gain as function of the pressure and imaging consequences

In order to determine the detector gain when the image was acquired, the front-end electronics should be calibrated, i.e., we need to know the charge

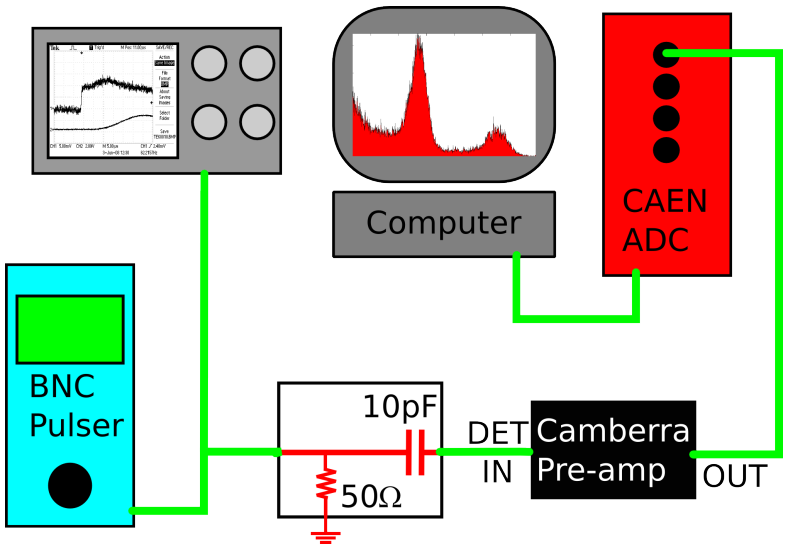

Figure 2.20: Schematic diagram for the electronic calibration.

value that corresponds to each ADC bin, in order to infer the collected charge for a given event or peak.

Figure 2.20 presents the schematic setup for the electronic front-end calibration. The method is based on the ejection of a precise charge value on the pre-amplifier making a correspondence between the charge injected and the ADC bin fired. To produce the precise charge pulse a BNC PB-5 Precision Pulse Generator and a 10 pF capacitor with 1% tolerance were used. Also a 50 Ω grounded resistor was used in order to fit the oscilloscope 50 Ω input impedance.

There are two reasons for using a low capacitor value: the first one is to generate very low charge pulses, preferentially at the same scale as the charge produced in the detector for the γ-photons. The second one is to avoid the influence of the pre-amplifier coupling capacitor, which generally has a capacity of a few nF. By using a small series capacitor (1000 times lower) the value of the coupling capacitor association will be negligible.

By loading the TNT-card parameter file it is possible to restore the front-end electronics settings. After that, all we need is to inject a rectangular voltage pulse on the capacitor, calculate the injected charge and register the

corresponding ADC bin.

In order to estimate the charge values of events in the acquired images (produced by the 59.6 keV photons) a Gaussian function was fitted to the total absorption peak of the pulse-height distribution. The gain is immediately calculated by dividing the peak charge value ($charge_{peak}$) by the average number of primary electrons (N_{ep}, see 1.5) produced by the 59.6 keV in Xe:

$$\text{Gain} = \frac{charge_{peak}}{N_{ep}} \tag{2.5}$$

2.3.4.1 Results and discussion

The results for the detector's position resolution, in the X direction, as a function of the collected charge, for 59.6 keV events, are depicted in Figure 2.21. It is shown that the position resolution improves as the collected charge increases, as expected from the literature [105]. Lower collected charge means a decrease in the SNR, responsible for the loss of precision in the interaction position calculation with the charge resistive division method [58]. From 1 bar till 1.8 bar, it is possible to observe a small influence of the increasing pressure in the position resolution, even when the collected charge decreases. This fact is due to the primary electron cloud confinement. However, the effect is no longer observed for pressures higher than 1.8 bar as the collected charge decreases to a tinny level resulting in a primary electron cloud confinement benefit dominated by the SNR influence.

From the present results it is possible to observe that the total detector gain decreases with the pressure. This decrease is a limitation of the micropattern gaseous detectors when working at high pressure [28, 23, 29], as reflected in Figure 2.22.

Figure 2.23 a) presents the relative light gain obtained as a function of the pressure and Figure 2.23 b) presents the relative 2D-MHSP gain. Using eq. 1.6 it is possible to estimate the number of produced scintillation photons per primary electron (N_{TfUV}). If considering Q_c approximately constant during the measurements, N_{TfUV} will depend only on the voltage applied across the

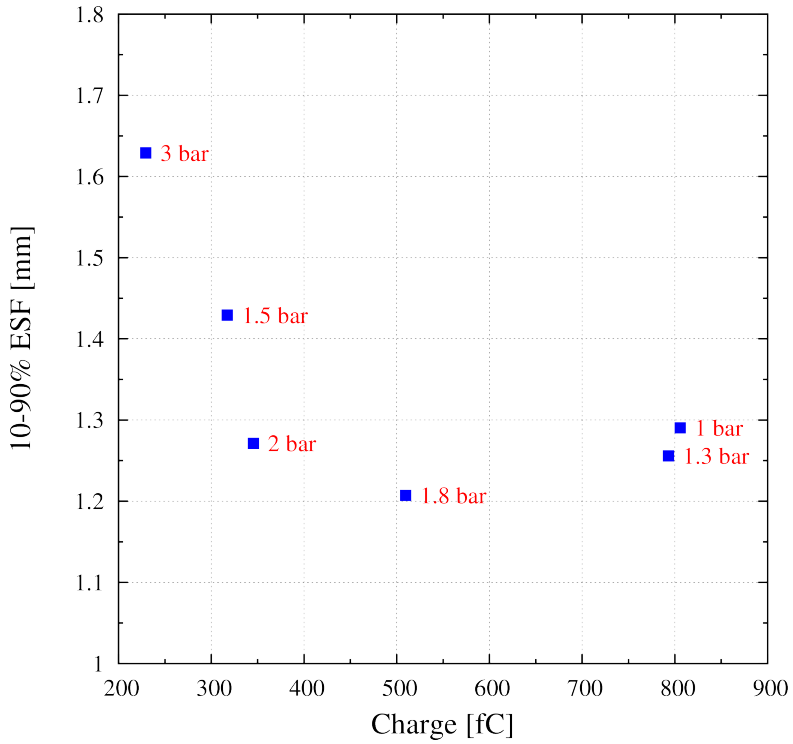

Figure 2.21: Position resolution in the X direction as a function of the collected charge for the 59.6 keV events.

scintillation region.

However, in this study, we cannot obtain the absolute light gain value as we cannot estimate the 2D-MHSP charge gain and we have to consider that the extraction efficiency did not change with the pressure, but we can simply normalize the results to 1 bar. The results of the relative light gain (Figure 2.23 a)) show a linear behaviour of the light gain with the increasing pressure. Is a direct influence of the increase of N_{TfUV} with the pressure. As the pressure increases the electron mean free path between collisions decreases and the number of possible collisions for the same drift length increases. If E/p is kept constant, the primary electrons will have the same average energy between collisions, resulting in a higher number of scintillation photons per primary electron.

The value for 2 bar is slightly lower because E/p was mistakenly set lower

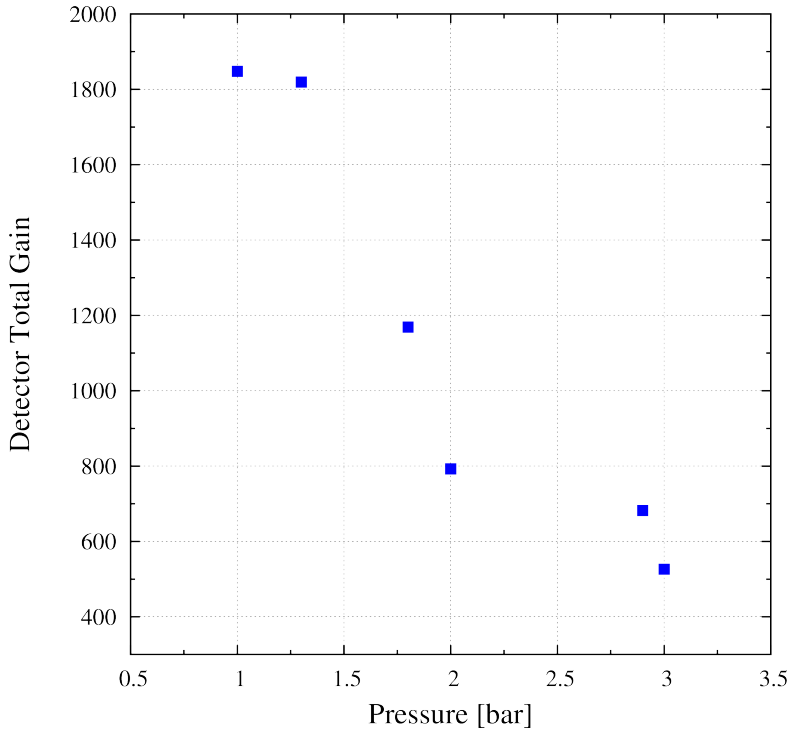

Figure 2.22: Total detector gain as a function of the gas pressure.

than the optimal value.

By knowing the total detector gain and the relative light gain it is possible to estimate the relative 2D-MHSP charge gain:

$$G_{Total} = G_{light} * G_{2D-MHSP} \tag{2.6}$$

where G_{Total} is the total detector gain, G_{light} is the scintillation light gain and G_{MHSP} is the charge gain of the 2D-MHSP.

To have a relative 2D-MHSP charge gain estimation, some approximations must be performed: the QE was assumed to be the same for all the photocathodes used and the solid angle variation was roughly constant.

The results for the relative charge gain as function of the pressure are depicted in Figure 2.23 b). The charge gain decrease behaviour with the increasing pressure is clearly observed. As the pressure increases, the mean-free-path between collisions and the electron energy between collisions de-

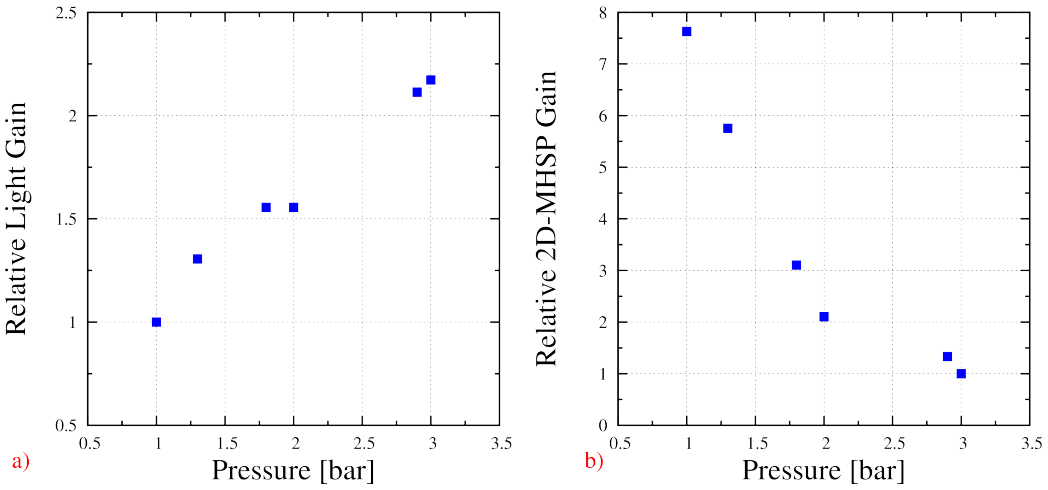

Figure 2.23: Relative gain as a function of the pressure: a) Relative light gain normalized to the value at 1 bar; b) Relative 2D-MHSP gain normalized to the value at 3 bar.

crease, resulting in a lower avalanche amplification. In order to restore the same amplification level, the electric-fields in the micro-pattern device should increase accordingly. However, it is not possible to infinitely increment the voltages in the electrodes due to the onset discharge, thus limiting the maximum achievable gain [25, 23, 24].

From 1 to 3 bar the charge gain decrease is almost of one order of magnitude, roughly 8 times, while the total detector gain (Figure 2.22) decreases just 4 times, showing the influence of the light gain.

2.3.5 Conclusions

The use of a GSPC configuration allowed performing the studies and evaluate the CsI-2D-MHSP photosensor.

The presence of a small reversed electric field in the photoelectron drift region improves the signal gain and the energy resolution as it benefits the photoelectron extraction efficiency. The optimal drift field could be easily and rapidly adjusted by monitoring the photosensor's signals with an oscilloscope.

The 1.3 mm position resolution obtained for 1 bar is almost in the limit of

the 59.6 keV electron range in Xe, demonstrating the good performance and image capability of the CsI-2D-MHSP. However, the benefit of the increasing pressure to the position resolution was just slightly verified until 1.8 bar. For higher pressures, the gain decreases to minimal levels and the lower SNR influences the position resolution performance.

The presence of a light gain was clearly demonstrated and it was shown that it increases with the pressure (considering that the extraction efficiency is independent of the pressure). However, as the light gain increases with the pressure, the CsI-2D-MHSP charge gain decreases in a faster proportionality.

3

General Conclusions and Future Work

The F2F concept has shown some possibilities of its application to nuclear medical imaging. Some changes should however be considered, in order to overcome its limitations.

CsI-2D-MHSP has shown to be a good photosensor choice for the light readout. At the atmospheric pressure the position resolution measured is almost the range of the 59.6 keV photoelectron in the gas. However, when the pressure increases (in order to increase the position and energy resolutions) the gain of the CsI-2D-MHSP degrades to minimal levels. A possibility to overcome this issue is to physically decouple the detector with a thick quartz window, having a scintillation region at high pressure and a VUV detection with multiplication region at the atmospheric pressure. Despite the increase of complexity, this solution will allow to pressurize the Xe at, for example, 20 bar, while keeping the CsI-2D-MHSP at the atmospheric pressure. The problem will then be centered in the new window. A quartz window with enough thickness to ensure 20 bar pressure does not favour the transmission of the produced VUV photons. Also, it will be a major issue for large area detections, as the costs and thickness required will increase with the area.

With this solution, the scintillation region and the photosensor are decoupled, giving the possibility to change the gas in the photosensor region, namely to Ne/CF_4 based mixture. As demonstrated in section 5.1.2.1, the photoelectron extraction efficiency is roughly 5 times higher in Ne/10%CF_4

than in pure Xe. Also, Ne based mixtures present a higher gain at low electric fields, a major advantage when the micro-pattern device has a low voltage discharge limit, making those mixtures a good choice for VUV gaseous photomultipliers [64, 106]. A full characterization of the CsI-2D-MHSP in Ne mixtures should be performed in order to evaluate its potentialities for this application.

Following the same idea of decoupling the detector and photosensor, the GSPC with imaging capability can be considered. GSPC configuration has shown excellent energy resolution and positioning properties when working at high pressure. Combining those properties and the CsI-2D-MHSP could open new possibilities for the application of gaseous detectors in medical imaging, spectroscopy and imaging of gamma and hard X-rays.

Part II

Study and development of UV position sensitive photosensors coupled to detectors envisaging High Energy Physics: RICH detectors

4 Introduction

4.1 Cherenkov Radiation

Similarly to the sonic boom generated by a supersonic aircraft travelling faster than the speed of sound in the air, when a charged particle in a material medium moves faster than the speed of light in that same medium it emits a special kind of radiation called Cherenkov Radiation, Figure 4.1. In fact, the first Cherenkov radiation was observed by Pavel Cherenkov in 1934 as blue light coming from a bottle of water undergoing bombardment by particles from a radioactive source. This discovery and his subsequent explanation of the process earned him Nobel Prize in Physics in 1958 [107–109].

The emitted light has a spectrum of frequencies, with the most interesting component being in the blue and ultraviolet band of wavelengths [108] as the yield of Cherenkov photons per unit wavelength (λ) is proportional to $1/\lambda^2$ (at extremely short wavelengths, the yield eventually drops off since the refractive index as a function of wavelength approaches unity) [6]. The blue light can be detected with a standard PMT while the UV light can be detected using GPMs [108].

Cherenkov radiation has a certain geometric signature: it is emitted in the form of a cone having an angle θ defined by:

$$\cos\theta = \frac{1}{\beta n} \tag{4.1}$$

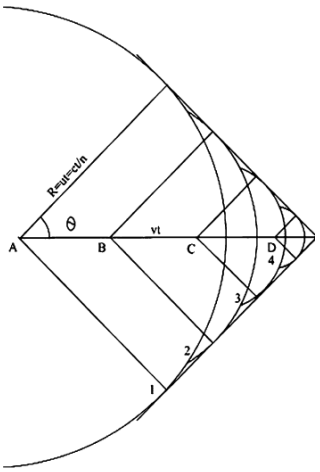

Figure 4.1: Movement of a charge particle in a medium with a velocity $v > u$. v - particle velocity; u- the speed of light in the medium having the refraction factor n. Adapted from [110].

where n is the refractive index of the medium and $\beta = v/c$ is the ratio of the velocity of the particle in the medium to the velocity of light in vacuum [107–109].

4.2 RICH Detectors

The first RICH (Ring Imaging Cherenkov) detector was proposed and demonstrated in 1977 by Seguinot and Ypsilantis [111], since then RICH detectors have become irreplaceable tools in a large number of nuclear and particle physics experiments, as for example CERN-Super LHC-ALICE [50], and CERN- COMPASS [51].

The base of RICH detectors is, to record and reconstruct the cone of light projected onto a planar surface (the photon-detector), providing particle identification (PID) as the cone angle is proportional to the momentum [112]. An example of PID is the Hadron identification presented in Figure 4.2, where it is possible to observe the $\pi/K/p$ separation performance of the COMPASS RICH-1 detector [113].

RICH detectors differ in geometry (focusing, proximity-focusing, etc),

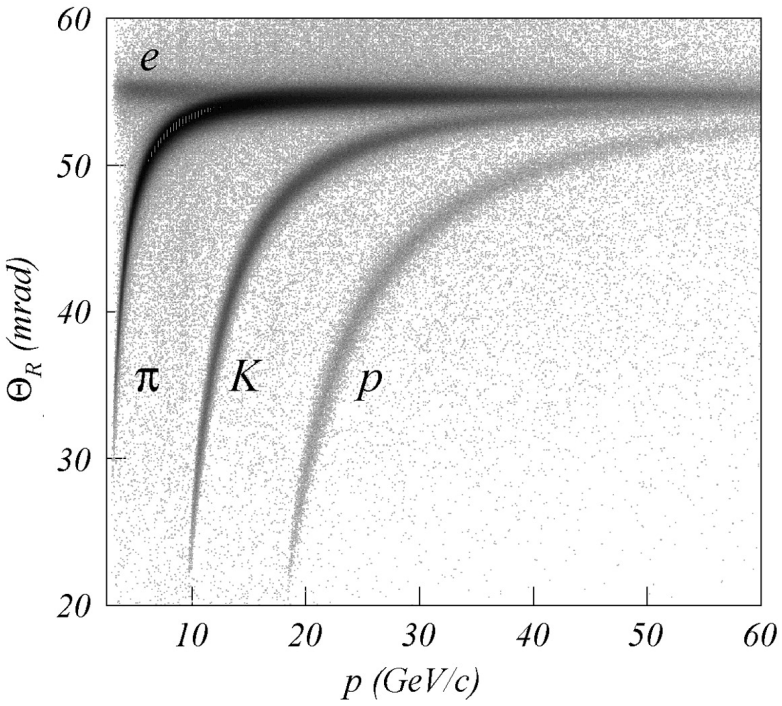

Figure 4.2: Measured ring Cherenkov angle Θ_R versus the particle momentum p in COMPASS RICH-1. Adapted from [113].

radiator (CF_4, C_2F_6, C_6F_{14}, etc) and in the photon-detector (PMT, MWPC) [114, 115].

The role of these detectors is so relevant that, in several fields, the advancements of experimental physics depend crucial on their characteristics. Crucial elements are the single photon detectors that have to make imaging possible, and important improvements in photon detection will automatically result in RICH detectors of increased performance.

The use of gaseous detectors, namely MWPC with coupled with CsI photocathodes, for large-area (several m^2) RICH counters is a well-established technique in nuclear and particle physics [115, 116]. In spite of the remarkable success, MWPCs with CsI photocathodes suffer from some limitations. Ageing resulting in a severe decrease of the quantum efficiency is reported after a collected charge of the order of some mC/cm^2 [117]. The presence of the CsI layer causes electrical instabilities of the MWPCs and long recovery

time (about 1 day) after discharges: due to avalanche photon-feedback it must be operated at low gain ($\sim 10^4$), limiting the single photoelectron detection efficiency[118, 119]. These features are related to the bombardment of the CsI layer by the positive ions generated in the multiplication process, which flow back to the cathode elements [120].

MicroPatterned Gaseous Detectors (MPGDs), in particular GEM-like devices, are a very promising technology in this field due to the intrinsic ion feedback suppression, the cascadability of the multipliers to reach high gain, the possibility to directly deposit CsI photocathodes on the multiplier's surface and the large area capability. For application in RICH detectors, a rather coarse spatial resolution is usually sufficient [121].

4.3 The THGEM

THGEMs (THick GEM) [122–124] are electron multipliers derived from the GEM design, scaling the geometrical parameters and changing the production technology. THGEMs can be produced over a large area by standard PCBs with holes mechanical drilled with chemical etched rims, in order to reduces edge discharges [118, 124].

Typical values of the geometrical parameters are PCB thickness of 0.4-1 mm, hole diameter ranging between 0.3 and 1 mm, hole pitch of 0.7-1.2 mm and rim width between 0 and 0.1 mm [118, 124], Figure 4.3.

Furthermore, THGEM-detectors were shown to have moderate (sub-millimeter) localization resolution [99, 106] and about 10 ns time resolution [126, 127], which comply with the requirements from most RICH devices in Particle Physics [116, 120, 128]. High gains were demonstrated in a variety of gases including noble gases and their mixtures (Ar, Xe, Ar-Xe [129], Ar/CH_4, Ar/CO_2 [123, 124], Ne, Ne/CH_4 [106]). One should note that although THGEM detectors have shown high gas gains for single-photoelectron detection [123, 124], the latter could be considerably lower in the presence of a relatively intense radioactive background (charged particles, X-rays), due

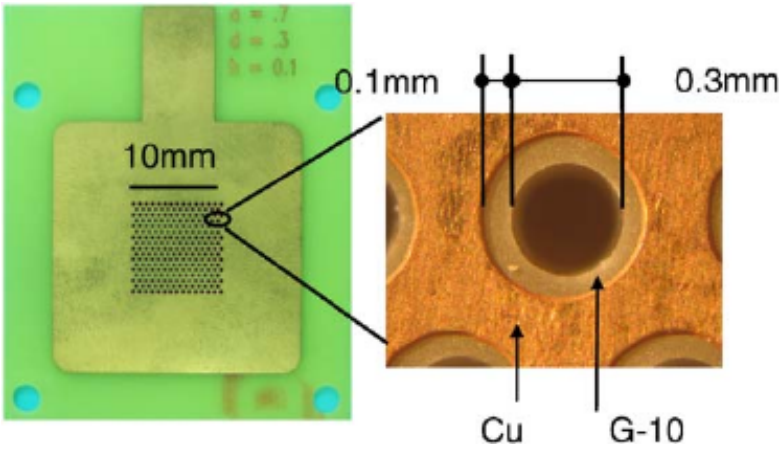

Figure 4.3: A photograph of a 0.4 mm thick THGEM with 0.3 mm holes and 0.7 mm pitch. The enlarged part (right) shows the 0.1 mm etched copper edge, preventing discharges at high potentials. Adapted from [125].

to the Raether limit [119, 106, 130].

4.4 Towards THGEM UV-photon detectors for RICH

The requirements imposed by the novel UV-photon detectors for RICH at CERN-Super LHC-ALICE [50] and CERN- COMPASS [51]experiments include high sensitivity to single photons, stable operation under intense ionizing-radiation background and the possibility of covering a large detection area at low production cost.

The Thick Gas Electron Multiplier (THGEM) could be a favourable building block and an electrode of choice, including one with a reflective CsI photocathode deposited on its top surface (Figure 4.4) [125, 131]. It is considered as an option for upgrading RICH detectors [121, 127, 132].

Reflective photocathodes are preferred to semitransparent, as they present a larger QE due to the higher photoelectron escape probability [43]. Also, a semitransparent photocathode requires keeping the entrance window at a fixed voltage by coating it with a thin metallic film, which absorbs pho-

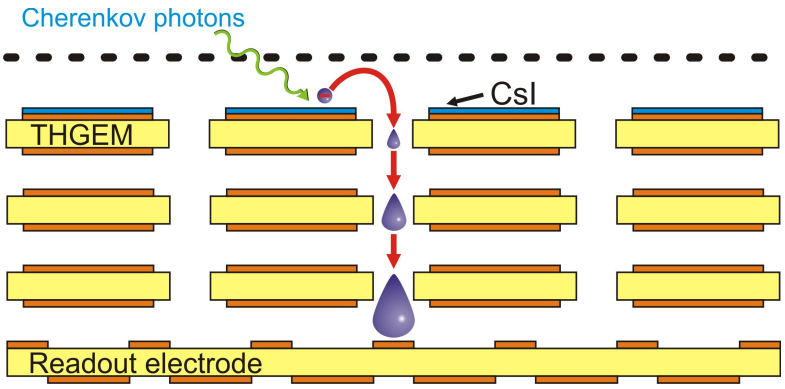

Figure 4.4: Schematic view of a THGEM-based UV-photon detector. This possible candidate for RICH, comprises a cascade of 2 or 3 THGEM electrodes, the top one coated with a reflective CsI photocathode,followed by a 2D readout anode.

tons [118]; moreover, thanks to the reduced gaps between the multiplication stages, these detectors can be successfully used in a magnetic field [118].

There are several advantages in using to use CsI-THGEM based detectors as UV-photon detectors for RICH [119]:

1. High gains ($>10^5$) are reachable with single or cascaded CsI-THGEM electrodes. Due to the exponential nature of single-photoelectron pulse-height distributions, and taking into account signal-over-threshold considerations, a high detector gain is an important factor in improving single-photon detection efficiency.

2. A THGEM can operate in poorly quenched gas mixtures as well as in gases emitting UV light (e.g. noble gases [129], CF_4 [125, 64]). This allows conceiving windowless detectors (same detector and radiator gas, e.g. like in [54]), with simpler layout and larger Cherenkov-photon detection yields.

3. In intense-background environment, CsI-THGEMs can operate in the so-called "Hadron-Blind mode" with zero or reversed electric field above the photocathode [123]; this significantly reduces particle-induced ionization signals [54].

Recently, there has been considerable interest in THGEM operation in Ne-based gas mixtures [106, 70, 133]. The main reasons are the comparatively low operation voltages and the higher gains reached in the presence of radioactive background (higher dynamic range); the low operation voltages result in reduced discharge probability, discharge energy and charging-up effects.

Ne-mixtures could be naturally of general interest for a broad field of detector applications; however, the main goal of this work has been the demonstration of their applicability to RICH. We therefore aimed to demonstrate, as a first step, that in these mixtures one can reach high photoelectron extraction from the CsI photocathode followed by their efficient collection and multiplication.

Indeed, as observed in section 4.5, since UV-induced photoelectrons are extracted from the CsI photocathode into gas, a fraction of them are backscattered into the CsI, depending on the gas, the electric field and the UV-photon energy [70, 67, 88, 66, 72, 89]. Furthermore, the extracted photoelectrons drift under the influence of the electric field and a fraction of them is collected by the THGEM-dipole field into the holes. In addition to the CsI QE, the photoelectron extraction and collection efficiencies play a major role in the detector's sensitivity to single photons (through the effective photon detection efficiency, as discussed below) and it is therefore important to maximize them, through optimization of the operation parameters.

For the sake of definition clarity, Figure 4.5 presents the possible fate of the photoelectrons in the case of a gaseous UV photon-detector based on a reflective CsI-THGEM: photoelectrons emitted from a reflective photocathode on top of a THGEM electrode, are (a) extracted from the photocathode with an efficiency ε_{extr}; (b) guided into the THGEM apertures and multiplied with an efficiency ε_{hole} ; (c) a fraction of the avalanche electrons is extracted and transferred to the following element with an efficiency ε_{trans}; another fraction is lost to the bottom-THGEM electrode. ε_{trans} equals unity, if at least a fraction of the avalanche charge is transferred to the next stage and the

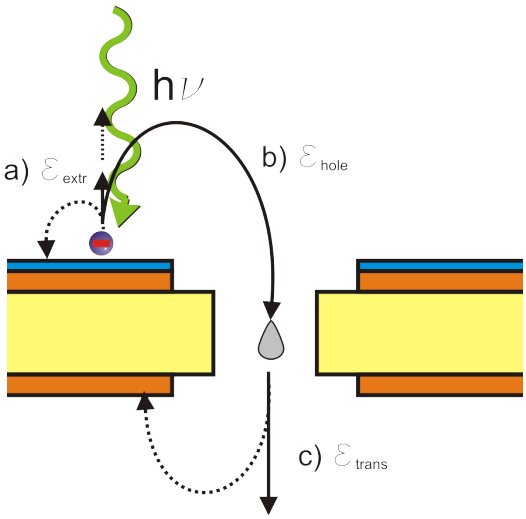

Figure 4.5: Schematic definition of the photoelectron efficiencies namely, a) extraction efficiency (ε_{extr}), b) photoelectron multiplication probability (ε_{hole}), c) transfer efficiency (ε_{trans}) and their possible paths.

event is detected [42].

The collection efficiency into the holes (ε_{coll}), defined as the resulting probability of ε_{hole} and ε_{trans}, was previously measured in a THGEM with the same geometry as used in this work (see below) for several gases (Ar/CH_4, Ar/CO_2, and CH_4); it was found to be unitary even at low THGEM gains (30, 20 and 6, respectively) [123], unlike the situation in GEMs with smaller holes [134]. However, it was never measured in Ne mixtures, where the higher value of the electron diffusion can be an issue.

It is important to note that the absolute single-photon detection efficiency of a detector system combines the effective photon detection efficiency (studied in this work) and the efficiency of counting single-photoelectron pulses above threshold. The latter, depends very critically on the total gain and on the threshold of the readout electronics (system noise), in view of the typical exponential distribution of single-electron pulses.

5 Studies and Measurements

5.1 THGEM in Ne/CH_4 and Ne/CF_4 mixtures

5.1.1 Experimental Setup

Measurements of the extraction and collection efficiencies were carried out using a single THGEM (thickness of the FR4 substrate t=0.4 mm; hole diameter d=0.3 mm; pitch a=0.7 mm; rim around the hole h=0.1 mm), sandwiched between two Multi-Wire Proportional Chambers. The MWPC had 1 mm spaced wires of 20 μm diameter. The distance between the wire plane and the cathode mesh was 1.6 mm. The top face of the THGEM electrode was coated with a reflective CsI photocathode (200 nm thick), deposited by thermal evaporation. The measurements of extraction efficiency were carried out with the MWPC positioned above the CsI surface ($MWPC_{top}$) as shown in Figure 5.1. The measurements of the collection efficiency of the extracted photoelectrons into the holes, were carried out with both, $MWPC_{top}$ and $MWPC_{bottom}$, as shown in Figure 5.6.

The assembled THGEM and MWPCs were introduced into a stainless steel vessel equipped with a UV transparent Suprasil window. It was continuously flushed with 1 bar of Ne/CH_4 and Ne/CF_4 mixtures, pure CH_4

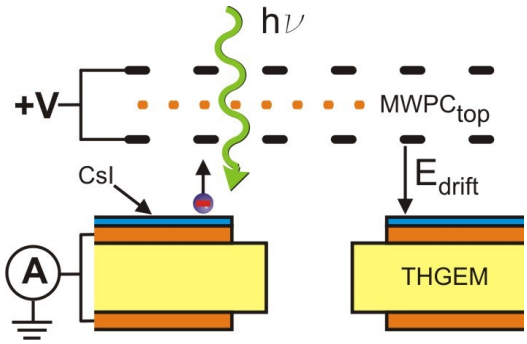

Figure 5.1: Schematic view of the experimental setup for measuring the photoelectron extraction efficiency from a CsI photocathode deposited on a THGEM.

and pure CF_4. The vessel was evacuated to 10^{-5}-10^{-6} mbar with a turbomolecular pump, prior to the gas filling. Gas composition and flow were controlled with two Mass Flow Controllers (MKS type 1179A) and a control/readout module (MKS type 247). The detector was irradiated with UV photons (185±5 nm peak) from a continuously emitting ORIEL Hg(Ar) lamp. All electrodes were biased with CAEN N471A power supplies and the currents were recorded with Keithley 610 CR electrometers (current mode). In pulse-counting mode, signals were recorded with an ORTEC 124 preamplifier followed by an ORTEC 572A amplifier (shaping time=0.5 μs) and an Amptek MCA 8000A multichannel analyser.

5.1.2 CsI photoelectron extraction efficiency into Ne/CH_4 and Ne/CF_4 mixtures

The experimental setup for the extraction-efficiency (ε_{extr}) measurements is depicted in Figure 5.1. The procedure is similiar to the one in section 2.1.1: a positive voltage was applied to the window establishing the drift field, being the top and bottom THGEM electrodes interconnected and grounded through the picoamperemeter, which records the photocurrent, both in vacuum (I_{vacuum}) and in gas mixture (I_{gas}).

The extraction efficiency (ε_{extr}) was obtained using Eq. 2.1.

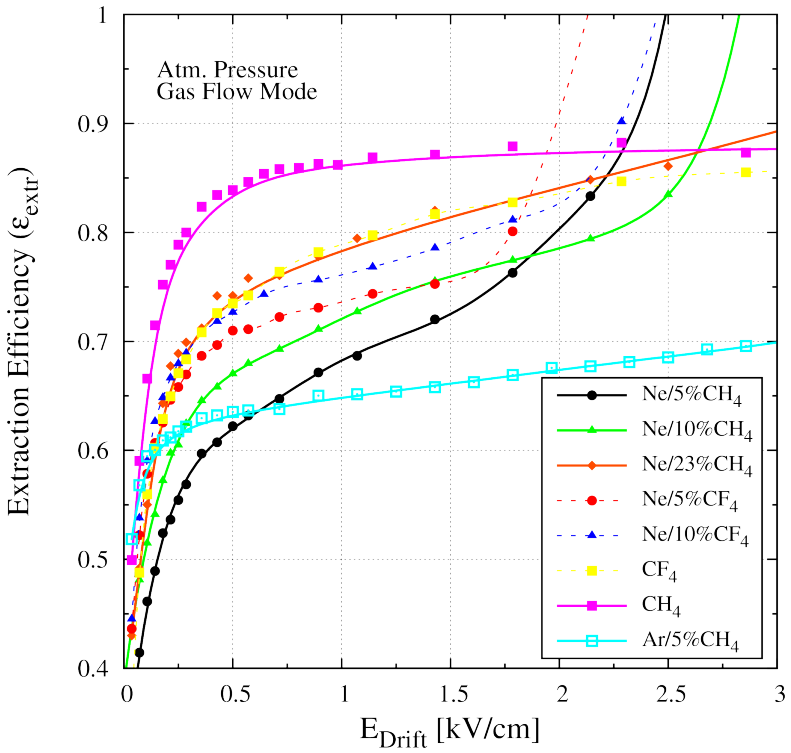

Figure 5.2: Photoelectron extraction efficiency from CsI into CH_4, CF_4, Ne/CF_4, Ne/CH_4 and Ar/5%CH_4 (for comparison) as function of the drift field using a UV lamp (185 nm peak). Data points measured for ε_{extr} >1 are not shown. Lines are just guides-to-the-eyes.

5.1.2.1 Results

The complete data set of the photoelectron extraction efficiency from CsI as function of the drift field is depicted in Figure 5.2. The extraction efficiency in Ar/5%CH_4, previously investigated in THGEM and other micro-pattern detectors, is shown for comparison.

Higher ε_{extr} was observed with CH_4 compared to CF_4; this is in accordance with the recent independent data and simulation results of [70], but in contradiction to the data of [67]. With small additives of CH_4 and CF_4 to Ne this behaviour was reversed; i.e., ε_{extr} was higher in Ne/CF_4 compared to Ne/CH_4. The explanation of both effects is not trivial and requires Monte-Carlo calculations, being carefully discussed in [70].

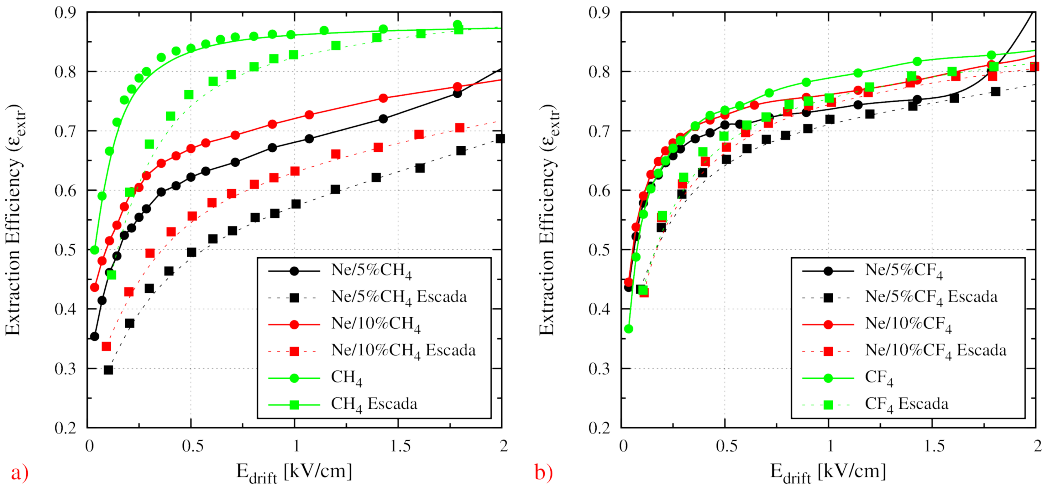

Figure 5.3: Photoelectron extraction efficiency from CsI into in Ne, CH_4 (a), CF_4 (b) and their mixtures as function of E/p. Results from other authors [70] are depicted as well for comparison. Lines are just guides-to-the-eyes.

Figure 5.3 presents in detail the obtained ε_{extr} on the region below $\leq 2\,\mathrm{Vcm^{-1}Torr^{-1}}$) together with results from Escada [70] for comparison. The registered discrepancies, at 1.5 kV/cm, are smaller than 2% in CF_4 and Ne/CF_4 mixtures (Figure 5.3 b)) but almost 10% in the case of Ne/CH_4 (Figure 5.3 a)). In fact the lines are almost parallel and in principle such discrepancy cannot be explained due to different gas purities, leading the explanation to a probable systematic effect not accounted. Several error sources could be considered: an error in the mass flow controllers settings could explain the discrepancy in the Ne/CH_4 mixtures but not for pure CH_4. Other possible explanations may rely on the drift distance or in the pressure regulation system with a pressure in the chamber lower than 1 bar.

5.1.3 Single THGEM effective gain

In order to measure the THGEM effective gain [65] (total charge produced in the avalanche normalized to the initial photocathode current), the setup present in Figure 5.4 was used. The initial photocathode current (I_{PC0}) is the "plateau" of the current curve measured according to the schematic

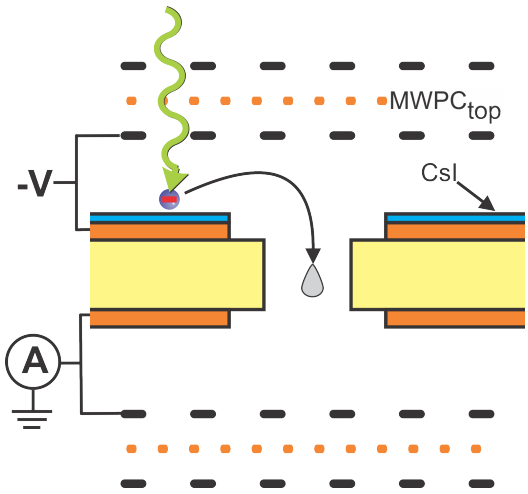

Figure 5.4: Schematic view of the experimental setup for measuring the single-THGEM effective gain.

presented in Figure 5.1, i.e., the "plateau" value of I_{gas} (see Figure 2.2).

5.1.3.1 Results

Figure 5.5 shows single-THGEM effective gain as function of the voltage across the electrodes for atmospheric pressure of Ne/5%CH_4, Ne/10%CH_4, Ne/23%CH_4, Ne/5%CF_4 and Ne/10%CF_4. As expected, in Ne-mixtures the charge multiplication starts at a very low field and the gain is dependent on the gas mixture and ratio [106]. As general trend, the effective gain curves shift towards higher operation voltages with higher molecular-gas concentration; however, the maximum achievable gain increases with the ratio of the mixture. In the presence of X-ray photons or MIPs the maximum achievable gains were typically 10-fold lower [106].

An interesting result is the higher gains obtained in Ne/CF_4 mixtures (maximum 10^6), when compared with the Ne/CH_4, for the same mixture ratios and hole voltages, showing the possibility to operate a detector with high gains at lower voltages.

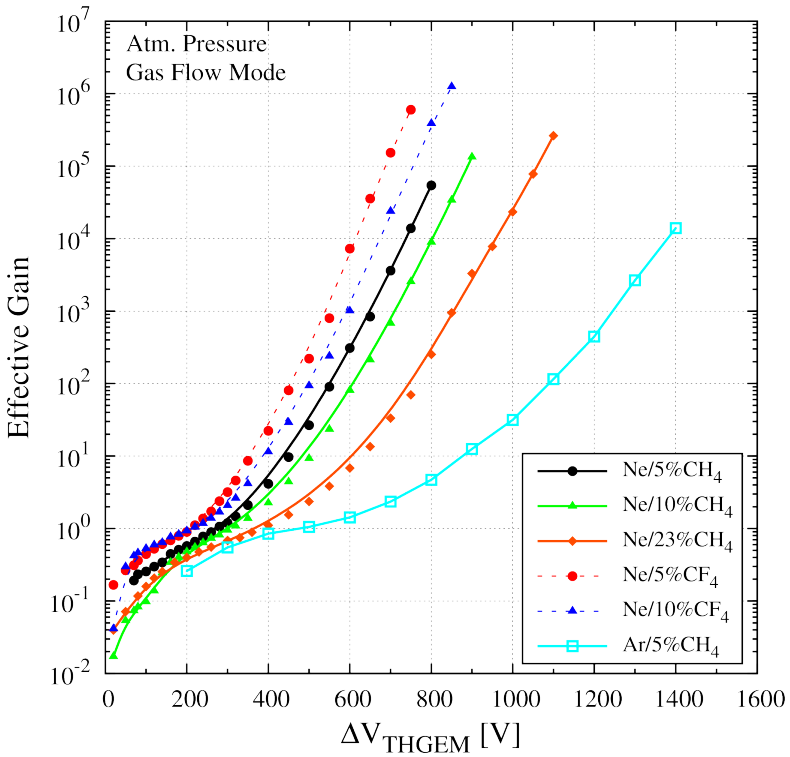

Figure 5.5: Single-THGEM effective gain curves, measured with UV photons in current mode, in Ne/CH_4 and Ne/CF_4 mixtures; and Ar/5%CH_4 (for comparison). Lines are just guides-to-the-eyes.

5.1.4 Single-photoelectron collection efficiency

The only accurate and unambiguous way to assess the single-photoelectron collection efficiency (ε_{coll}) is through a complex method using pulse-counting mode [65]. To perform such measurements, current mode cannot be used for two main reasons. The first is that, under gas amplification it is not possible to separate transfer efficiency and gas gain currents. It is possible to measure the single-photoelectron collection efficiency in current mode but, just in the case that THGEM gain is unitary [42, 83]. The second reason is that, due to the statistical fluctuations in the amplification process of single electrons, many events have only a small number of electrons at the THGEM hole exit (see Figure 5.7). DC current measurements are not sensitive to the loss of single photoelectrons or to events with small gain, as their contribution to

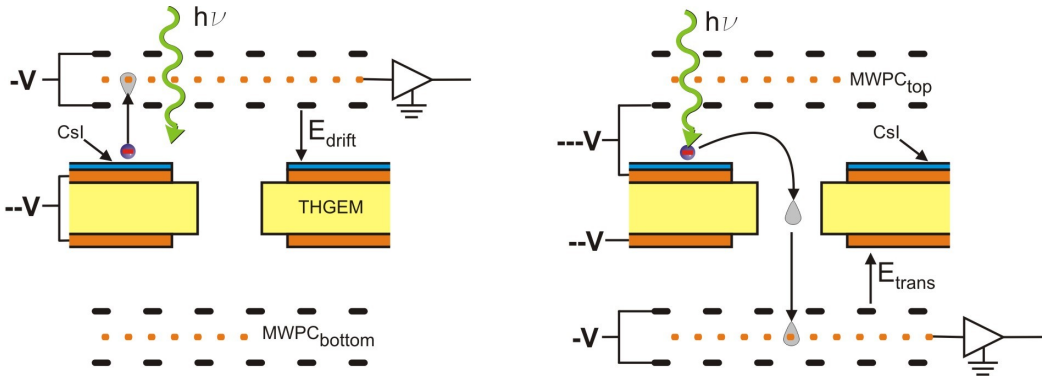

Figure 5.6: Schematic view and electrical bias of the experimental setup for measuring the single-electron collection efficiency into the THGEM holes: a) measurement of the reference pulse-height spectrum with a MWPC reference detector; b) measurement of the pulse-height spectrum of the investigated detector.

the total current is negligible when the detector is operated in multiplication mode [134].

The pulse-counting method (Figure 5.6) consists of comparing, under identical conditions, the event-rate of the THGEM/$MWPC_{bottom}$ to the one measured with the $MWPC_{top}$ (detector known to have ε_{coll}=1 [134] since the ratio of the electric fields in the MWPC mesh is higher than 3 [65]). The method relies on another assumption: in both cases the single-electron pulse-height distributions are exponential, following the Polya relation without saturation [123]:

$$P(q) \simeq \frac{1}{G} \mathrm{e}^{-(\frac{q}{G})} \tag{5.1}$$

where G is the total detector gain and q is the gain of each individual avalanche (in the case of single electron conditions, q represents the number of electrons in the avalanche following the multiplicative process). Therefore, it is important to adjust the total gain in both measurement steps to be identical, by comparing the slopes of the exponential distributions.

As shown in Figure 5.6, both detectors are coupled to the same photocathode, under the same UV flux. Reference detector ($MWPC_{top}$) and

investigated one (THGEM/MWPC$_{bottom}$) were operated at equal total gain of $\approx 10^4$, adjusted by the MWPC$_{bottom}$ voltage to have equal slopes of the total pulse-height distribution; the MWPC$_{bottom}$ role was to have the total gain sufficiently high for pulse counting even when the THGEM voltage (gain) is low. The drift field in the reference detector (Figure 5.6 a) was adjusted to have an efficient photoelectron extraction, namely a value at the "plateau" of the extraction versus the field (see Figure 5.2); in the investigated THGEM/MWPC$_{bottom}$ detector (Figure 5.6 b) the drift field between the photocathode and MWPC$_{top}$ was set to zero (as discussed in [123]) in order to establish a Hadron Blind configuration. The number of detected events in each configuration was evaluated by integrating the middle part of each pulse-height spectrum in order to minimize possible errors due to electronic noise contribution (lower end of the spectrum) or to secondary effects (higher end). Examples of single-photoelectron pulse-height spectra in both detectors and the integration region for collection-efficiency evaluation are shown in Figure 5.7.

The single-electron collection efficiency of the THGEM (ε_{coll}) was derived from the ratio between the number of events measured with the THGEM/MWPC$_{bottom}$ (N_{THGEM}) to that in the MWPC$_{top}$ reference detector (N_{ref}) [123, 134, 65]:

$$\varepsilon_{coll} = \frac{N_{THGEM}}{N_{ref}} \tag{5.2}$$

5.1.4.1 Results

The results of single-photoelectron collection efficiency into THGEM holes are shown in Figure 5.8. The photoelectron collection efficiency increases with the potential across the holes, reaching unity at THGEM gains of 25-1000, depending on the filling gas.

For a same ratio, the full ε_{coll} is reached in Ne/CH_4 and Ne/CF_4 at approximately the same THGEM hole potential. Due to the different THGEM gains (see Figure 5.5), the maximum ε_{coll} will be obtained at lower gains in

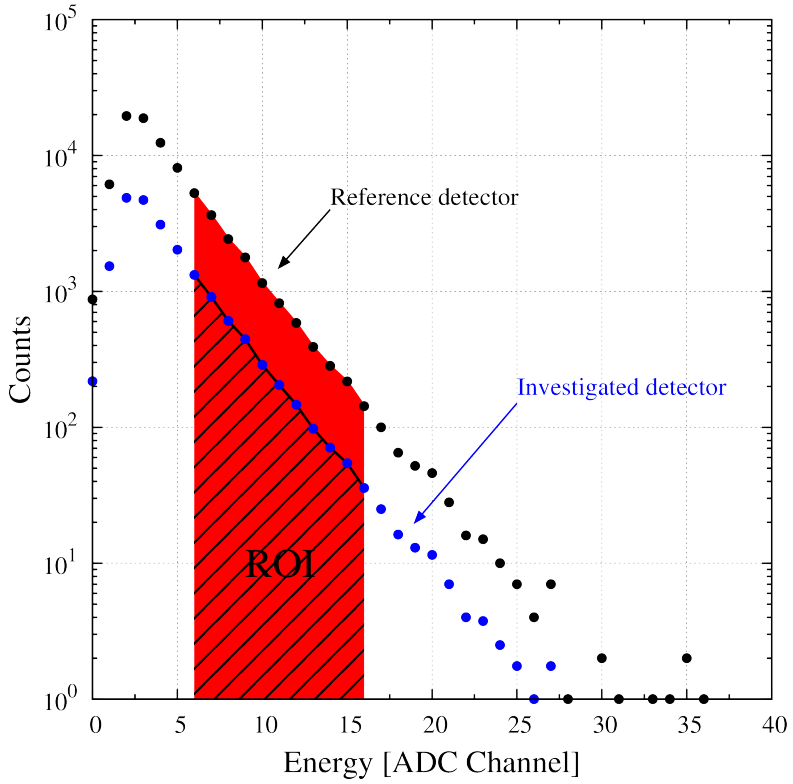

Figure 5.7: An example of single-photoelectron pulse-height distributions measured in the reference and in the investigated detectors; the respective counts, N_{THGEM} and N_{ref}, at equal total gains (slopes) and measurement times, were derived from the integration of the ROI shown in the figure.

Ne/CH_4. As an example we can compare, the mixtures 95/5: the full collection efficiency is obtained at a gain=25 in Ne/CH_4 while in Ne/CF_4 the gain is equal to 220.

The results also depicted the mixture ratio influence on ε_{coll}. When the ratio increases the full ε_{coll} is obtained at higher gains.

Examining the data we may conclude that full collection efficiency is achieved for realistic working conditions.

5.1.5 Discussion

The effective photon detection efficiency of the CsI-coated THGEM is defined as:

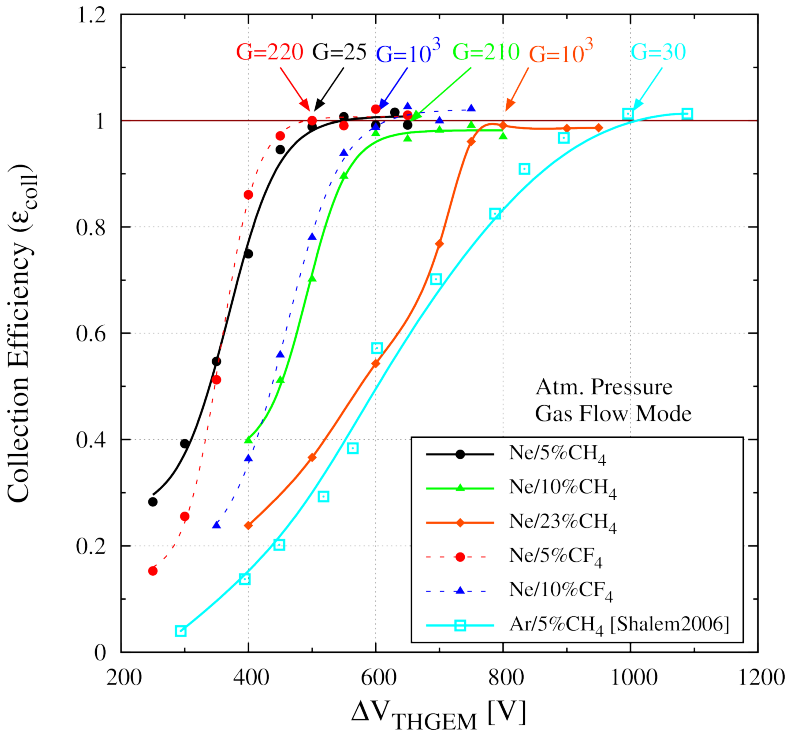

Figure 5.8: Single-photoelectron collection efficiency in Ne/CH_4 and Ne/CF_4 mixtures, measured in pulse-counting mode, versus the voltage across the THGEM; the threshold gain values for reaching full collection efficiency are indicated for each mixture. $Ar/5\%CH_4$ curve [123] was plotted for comparison.

$$\varepsilon_{effph} = QE \times A_{eff} \times \varepsilon_{extr} \times \varepsilon_{coll} \tag{5.3}$$

where QE is the CsI vacuum quantum efficiency at a given wavelength [43], A_{eff} is the photocathode effective area (fraction of surface not covered by holes), ε_{extr} is the extraction efficiency into the gas mixture (Figure 5.2) and ε_{coll} is the single-photoelectron collection efficiency into the THGEM holes Figure 5.8.

With a reflective photocathode on the THGEM top, the field at the photocathode surface is defined by the voltage across the plate (affecting the dipole field emerging out of the holes). Examples of the field in the present electrode geometry are given in Figure 5.9.

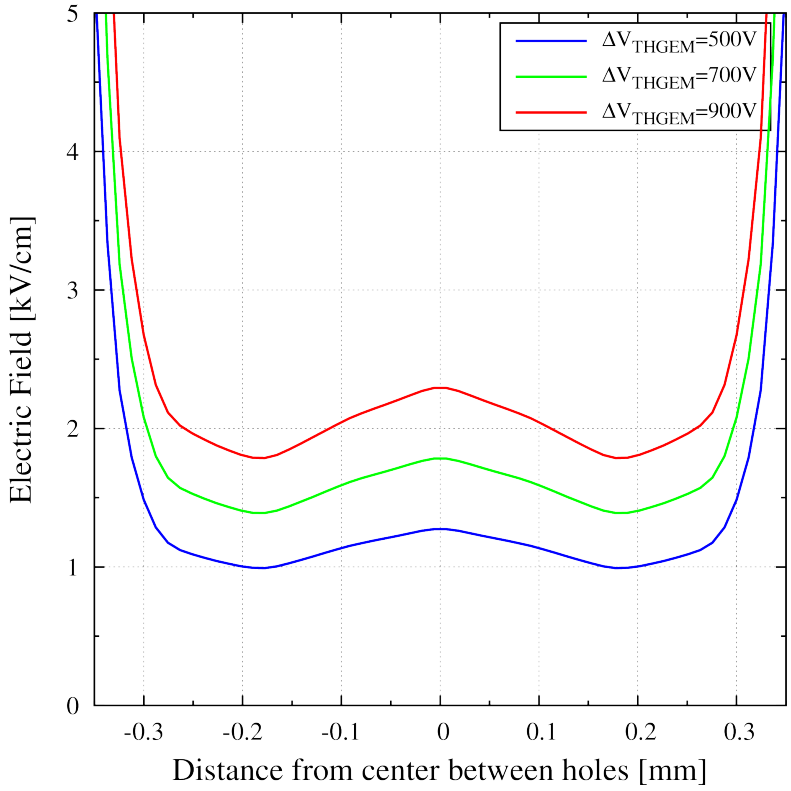

Figure 5.9: The electric field on THGEM top surface used in this work, $E_{surface}$, as calculated by MAXWELL along the line interconnecting two hole centers.

Figure 5.9 shows the electric field on the photocathode surface between two adjacent holes, as a function of the voltage applied across the THGEM, calculated with MAXWELL software [135]. As can be seen, the field at the surface exceeds 1.5 kV/cm (for maximum gains in all gases investigated; see Figure 5.5 and Figure 5.9); thus one can evaluate ε_{extr} being 0.72-0.87, at 1.5 kV/cm, and larger at higher fields (see Figure 5.2). In order to maximise ε_{extr} the CsI-coated electrode should be preferably operated at the highest possible applied voltage across the holes, though keeping in mind stability effects (charging up, micro-discharges) that are often affected at higher voltages.

The electric field near the holes reaches values of 4-5 kV/cm; in this case, the electrons, drifting at the high field in the photocathode vicinity, might

Gas	ΔV_{THGEM}	Gain	QE (170nm)	A_{eff} This THGEM	A_{eff}* Optimal THGEM	ε_{extr}	ε_{coll}	ε_{effph} This THGEM	ε_{effph}* Optimal THGEM
Ne/CH_4 (95/5)	800	5.4E4	0.3	0.54	0.91	0.73†	1	0.12	0.20
Ne/CH_4 (90/10)	900	1.3E5	0.3	0.54	0.91	0.79‡	1	0.13	0.22
Ne/CF_4 (95/5)	750	6.0E5	0.3	0.54	0.91	0.76†	1	0.12	0.21
Ne/CF_4 (90/10)	850	1.2E6	0.3	0.54	0.91	0.83‡	1	0.14	0.23

Table 5.1: Schematic view of a THGEM-based UV-photon detector. This possible candidate for RICH,comprises a cascade of 2 or 3 THGEM electrodes, the top one coated with a reflective CsI photocathode, followed by a 2D readout anode.

initiate both scintillation (photon feedback at the photocathode) and charge multiplication [106], before entering the hole. One can speculate that in case a primary electron misses the hole due to the relatively large electron diffusion in Ne mixtures, the resulting secondary electrons could compensate for that. This was demonstrated in GEM [65]. Indeed, as seen in Figure 5.8, the THGEM voltage, and gain, required for the onset of full ε_{coll} increase with molecular-gas concentration. This may indicate indeed that some gain outside the hole is needed to overcome the possible suppression of scintillation-induced secondary electrons by the quencher in the mixture.

Table 5.1 summarizes the main results and predictions of the effective photon detection efficiency (ε_{effph}) of a THGEM-based UV-photon detector; for simplicity, the efficiency was determined for photons with a wavelength of 170 nm.

ε_{effph} values between 0.12 and 0.14 were calculated in Table 5.1 for the THGEM geometry used in this work (t= 0.4 mm, d=0.3 mm, a=0.7 mm, h=0.1 mm), for a single QE value taken here as example, of 0.3 at 170 nm [43]. One of the main factors in the ε_{effph} value is the photocathode effective area: A_{eff}=54% in the present case. One way to increase ε_{effph} is increasing

*Optimal THGEM: t=0.4 mm, d=0.3 mm, a=1 mm; h=0.01 mm
†Value for 1.5 kV/cm photocathode electric field
‡Value for 2 kV/cm photocathode electric field

A_{eff}, by increasing the hole pitch and decreasing the rim size ("optimal" THGEM in Table 5.1). For example, a THGEM geometry with t=0.4 mm, d=0.3 mm but with a=1 mm and h=10 μm, will have A_{eff}=91%. Based on our previous experience [123], the collection and extraction efficiencies will not change significantly with the optimal geometry, at the high-range operation voltages (gain $>10^3$). As shown in Table 5.1, assuming that there will be no significant change in the operation voltages (indicated in the table for the current geometry), we expect for this "optimal" electrode geometry, ε_{effph} values of 0.20-0.23 for the different mixtures used in this work.

It should be noted that a small rim, of 10-20 μm, was shown to result in lower attainable voltages and therefore about 10-fold lower attainable gains (this was observed in Ar/CH_4 and Ar/CO_2 mixtures [118, 124]); but also that high total gains, of $\sim 10^6$, were recently demonstrated in a triple-THGEM with 10 μm rims, in Ar/50%CH_4 [132]. However, in Ne-based mixtures the operation voltages are lower and the small rim is expected to affect the maximum attainable gain in a less dramatic manner. Further studies with the "optimal" THGEM will clarify its applicability.

All results described above relative to the effective photon detection efficiency, ε_{effph}, were obtained with a single-THGEM detector. The efficiency of transferring avalanche electrons from stage to stage, does not affect ε_{effph}.

The absolute single photons detection efficiency ε_{photon}, e.g. in RICH, depends both on the detector's effective photon detection efficiency ε_{effph} and on the achievable gain (detected pulses above threshold (fp_{th})). In a simplified way this can be written as:

$$\varepsilon_{photon} = \varepsilon_{effph} \times fp_{th} \tag{5.4}$$

At this point we could make a very preliminary comparison between THGEM- and MWPC-based UV-photon detectors. For example, in the MWPC of COMPASS, coated with CsI photocathode and operating in pure CH_4, both extraction and collection efficiencies are close to unity. The effective CsI area is 1 and the effective photon detection efficiency ε_{effph} ~0.3.

With a gain of 1-2×10^4 and electronic thresholds imposed by ionizing background and noise, fp_{th} values of 0.7 at best could be reached at the experiment (0.9 at the laboratory), yielding an absolute efficiency of detecting single photons ε_{photon}=0.21 (0.27 at the laboratory)[119, 136].

Another example is the ALICE HMPID module which presents a "single electron detection efficiency" (in our case corresponding to $\varepsilon_{coll}.fp_{th}$) higher than 90% at a gas gain of $\sim 5\times10^4$ [128]. Considering QE=0.3 and ε_{extr} close to unity (as the multiplication gas is CH_4 [137]), $\varepsilon_{photon}\approx$0.27.

This may indicate, that THGEM UV-detectors with optimal geometry (Table 5.1), capable of operation at higher gains (>10^5) even in the presence of higher ionization background [119], could possibly compete with MWPC/CsI devices in future RICH applications. They are also simpler, with low photon feedback and photocathode ageing and possibly cheaper, to produce over large surfaces.

5.2 THCOBRA: very first results in IBF suppression

Although the proof of principle of a cascaded THGEM detector for RICH applications was already shown, in beam, using Ne/10%CH_4 [138] and Ar/30%CO_2 [127], other subjects are still in intense R&D interest, namely the back-flow of the ions originated during the multiplication process, responsible for the trigger of secondary effects and ageing of the photo-converts used.

The Ion Back-flow Fraction (IBF) is defined as the fraction of the last-avalanche induced ions that flows back to the drift volume or to the photocathode [139]. In Figure 5.10 is presented the operation principle and physical processes on a multi-stage GPM, using a reflective photocathode, showing the electron and ion paths. The ions originated in the multiplication stages will drift to the upper multiplier and, some of them, that are not trapped in the electrodes, will drift to the photocathode, triggering secondary effects like the emission of secondary pulses, photocathode and hole surface charging-up

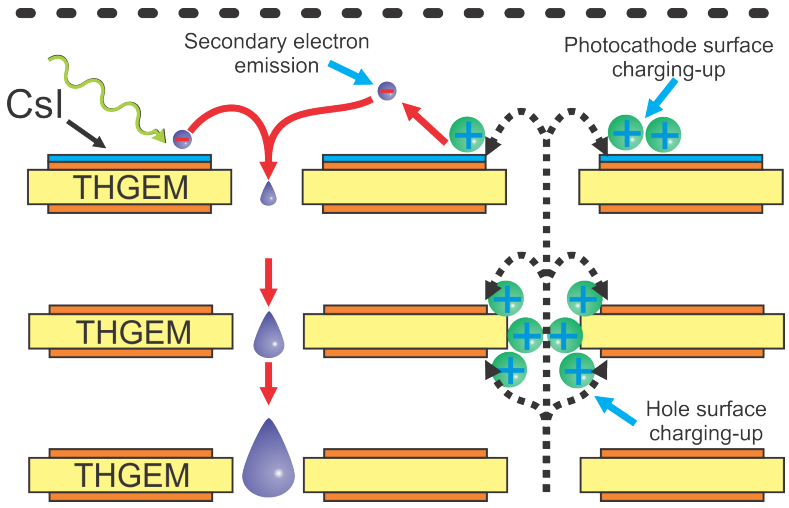

Figure 5.10: A cascaded triple-THGEM detector scheme showing photoelectron trajectories, avalanche development and some possible ion back-flow paths in the opposite direction. Secondary effects (secondary electron emission, photocathode surface charging-up and hole surface charging-up) are also represented.

[86, 140] and the photocathode ageing [82, 141].

An example of secondary pulses originated by ion impact on a CsI photocathode is presented in Figure 5.11 (adapted from [140]). The pulses are originated from the secondary electron emission (SEE) resulting from the ion collision against the photocathode or the copper electrodes. Those secondary pulses could cause problems on photon localization by broadening the charge induced on the readout elements, on single-photon detection efficiency and on gain limitations due to divergence from the Townsend-avalanche multiplication process and leading to instabilities and breakdown [86, 142, 143].

There are other secondary effects due to ion back-flow such the insulator charging-up, manifested at large fluxes and gains [86] and in Time Projection Chambers (TPCs), where the ion-cloud penetration into the drift volume builds up space-charge effects and causes rate-dependent dynamic electric-field distortions, consequently affecting the TPC resolution [139, 144, 123].

One of the most effective way to reduce the IBF is through a technique mostly used in TPCs by using an ion-gate electrode. However, ion gating

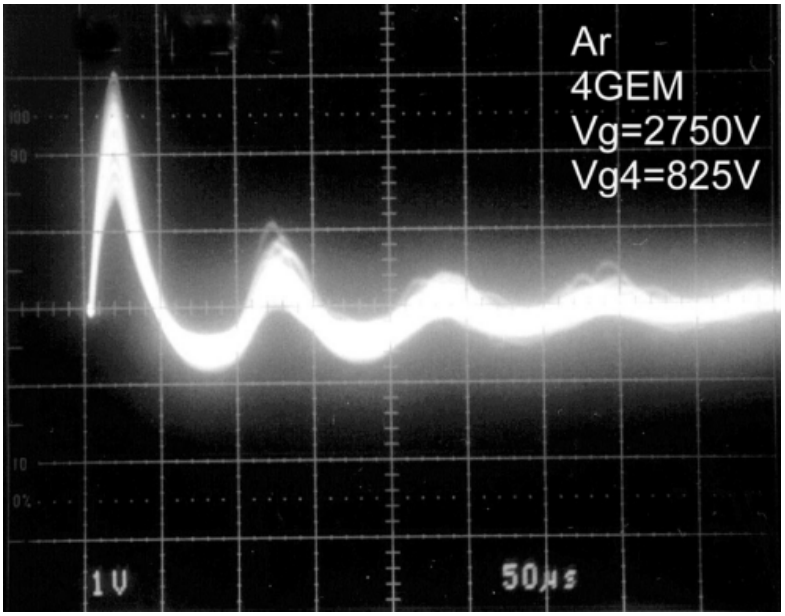

Figure 5.11: Ion feedback-induced signals in Ar, in a 4 GEM photo-multiplier. Adapted from [140].

often requires an external trigger source and involves electronic noise problems; it induces dead-time and thus rate-limitations, restricting its range of applications [139, 145]. For those reasons and for simplicity's sake, an IBF effective reduction in DC mode will have advantages. An operation of a 4-GEM detector with reflective photocathode on the top of the first electrode provided an IBF value of $\sim$0.1 at gains of 10^5-10^6 using the gating technique [145].

Works in DC mode have shown an effective IBF reduction by changing the detector's geometry and electric-field configuration [145]. In cascades comprising 3-4 GEM electrodes, it is possible to reduce the IBF by optimizing the hole diameter and shape as well as the transfer fields between the elements [146] and using asymmetric GEM powering [145].

Another technique to reduce the ion back-flow effects is by reducing the electric-field at the photocathode surface, reducing the ion-impact [141]. However, this approach is not always acceptable, as an efficient detection of single photons requires the highest possible collection efficiency (Figure

5.8), which in the case of Ne mixtures, is limited to at least 1 kV/cm (Figure 5.9). That could be another advantage when using Ne mixtures on cascaded detectors incorporating a solid photocathode. The full collection efficiency is reached at lower V_{hole} values, meaning that the electric field at the photocathode surface will decrease [64], thus decreasing the ion impact energy with the photocathode, which is directly proportional to the drift field [146].

For single-photon detection capability, a GPM should present gains above 10^5 [147], value from which the ion feedback begins to have a negative effect on the CsI photocathode [68]. The IBF is almost independent on the gas mixture [146], but the effects are strongly dependent on the photocathode material, mainly for visible sensitive photocathodes [143, 148].

A great advance of ion-blocking in DC mode was the introduction of the MHSP in a cascaded detector. Firstly as a last element on the cascade [143], and then as an ion-collector device, by swapping the strips polarity, having two possible configurations: Reversed-bias MHSP (R-MHSP) [139, 142, 149] and Flipped Reversed-bias MHSP (FR-MHSP) [150, 151], presenting IBF values of 9×10^{-4} and 3×10^{-4}, respectively, at a gain of 10^5 and with a CsI semitransparent photocathode [150]. Higher IBF values were obtained for reflective photocathodes when compared to the semitransparent ones due to the drift field value and direction [139]. However, IBF values of $\sim$0.02-0.03 at gains of 10^5-10^6 are considered suitable for a GPM incorporating a CsI photocathode [142].

Other concepts for ion-blocking using the MHSP are under development: the Photon-Assisted Cascaded Electron Multiplier (PACEM) [152], which presents good IBF performance even in high pressure detectors [29], but using a more complicated detector geometry and concept, where the signal is transmitted to the next amplification stage by the electroluminescence process occurring inside the GEM holes. As a result, there is the need of a CsI photocathode in each amplification stage.

Following the success of the MHSP operating in reversed or flipped reversed mode, a similarly concept was developed in a "thick-hole" configura-

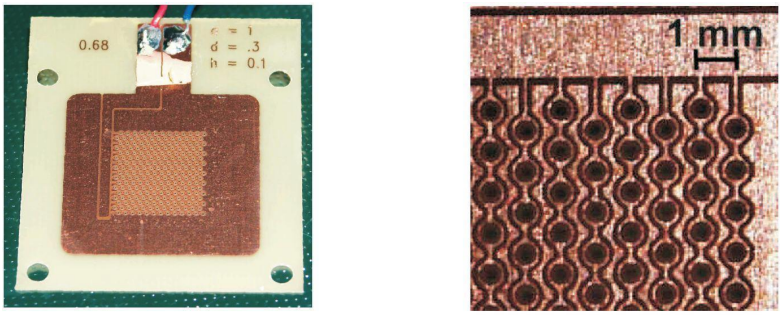

Figure 5.12: Global view of a THCOBRA (on the left); close-up view, showing the cathodes strips and the anodes around the holes.

tion - the THick-COBRA (THCOBRA) [153], Figure 5.12. Similar to the THGEM, the THCOBRA is produced by a printed-circuit board technique, including an additional patterned electrode on one side in order to trap the ions flowing from the multiplication stages.

The ion-trapping in the THCOBRA structure could occur in two different ways by using the additional electrode. One way is by facing it to the electron multiplication region, allowing the back-flowing ions to be trapped (THCOBRA in reverse mode: R-THCOBRA, Figure 5.13 a) and the other is with the additional electrode facing the opposite region of the electron multiplication region (flipped configuration with reverse polarization: FR-THCOBRA, Figure 5.13 b). In the latter, not only ions flowing back from the multiplication regions can be trapped by the extra electrode, but also those produced in its own multiplication holes[154].

In both modes, a systematic study of the operation voltages of all electrodes should be carefully performed in order to determine the efficiency of the ion trapping without sacrificing the full single-electron detection efficiency.

In these studies, a THCOBRA with the following geometry was used: thickness of the FR4 substrate t=0.4 mm; hole diameter d=0.3 mm; pitch a=1 mm and rim around the hole h=0.1 mm. The gas was Ar/5%CH_4 mixture (Ne system was unavailable during these measurements).

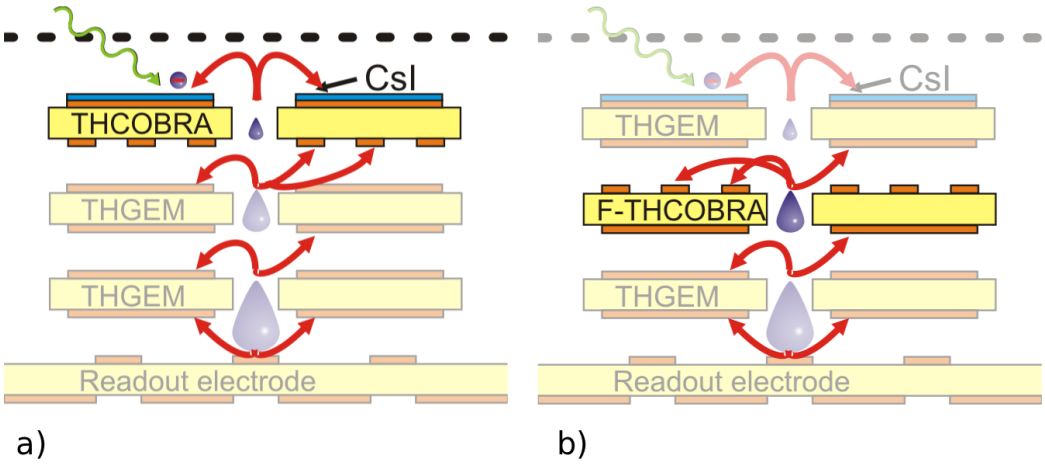

Figure 5.13: Two detector configurations using a THCOBRA acting as an ion suppressor element: a) As a first stage element in a reversed-bias configuration, R-THCOBRA; b) on the 2^{nd} multiplication stage in a flipped and reversed-bias THCOBRA configuration, FR-THCOBRA.

5.2.1 Visible gain

Visible Gain (G_{VIS}) is defined as the number of electrons transferred from a given multiplier element onto a consecutive electrode per primary electron, i.e., the gain measured at the top electrode of the next multiplier. Remember that the Effective Gain, is related to the total number of electrons created in the avalanche, per primary electron, including the charge trapped in the bottom electrode [139].

Figure 5.14 shows the schematic view and electrical bias of the experimental setup for measuring the R-THCOBRA visible gain. Following the definition, G_{VIS} is calculated from Eq. 5.5 [150]:

$$G_{VIS} = \frac{I_M}{I_{PC0}} \tag{5.5}$$

where I_M is measured in the MWPC mesh (while keeping the MWPC wires floating), and I_{PC0} is obtained as explained in section 5.1.3.

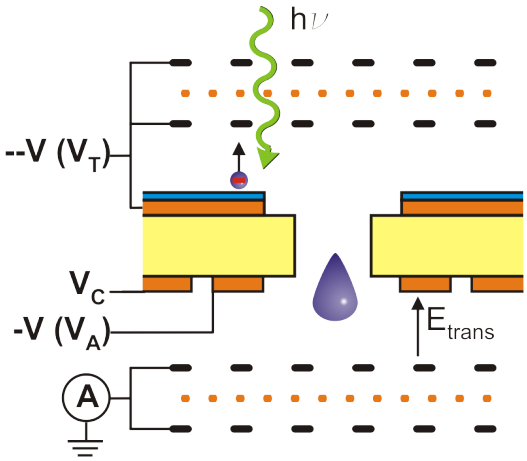

Figure 5.14: Schematic view of the THCOBRA G_{VIS} measurement (charge transferred to the next multiplier per single-electron.

5.2.1.1 Results and discussion

Figure 5.15 presents the results for the G_{VIS} as a function of V_{CA} (voltage difference between the strips (V_C-V_A)) for different V_{hole} values (V_A-V_T): 900 V, 1100 V, 1200 V and 1400 V, corresponding to gains around 10, 10^2, 10^3 and 10^4, respectively, for two transfer field values: 0.5 and 1.5 kV/cm. The results show that R-THCOBRA G_{VIS} increases with V_{hole} and with the transfer field. As the transfer field increases, the charge transfer to the next element also increases, decreasing the number of electrons trapped in the anode-strip.

The opposite behaviour is observed when increasing V_{CA}. As the voltage between the strips increases, the charge transferred to the next element decreases. Nevertheless, G_{VIS} decreases only one order of magnitude for V_{CA}=250 V when V_{hole}=900 V and for V_{CA}=500 V when V_{hole}=1400 V. In principle, it shows that G_{VIS} decreases one order of magnitude when $V_{CA} \approx 1/3 V_{hole}$.

By interconnecting the THCOBRA strip electrodes, i.e., V_{CA}=0 V, the same gain behaviour of a normal THGEM with the same hole and rim geometry has been measured.

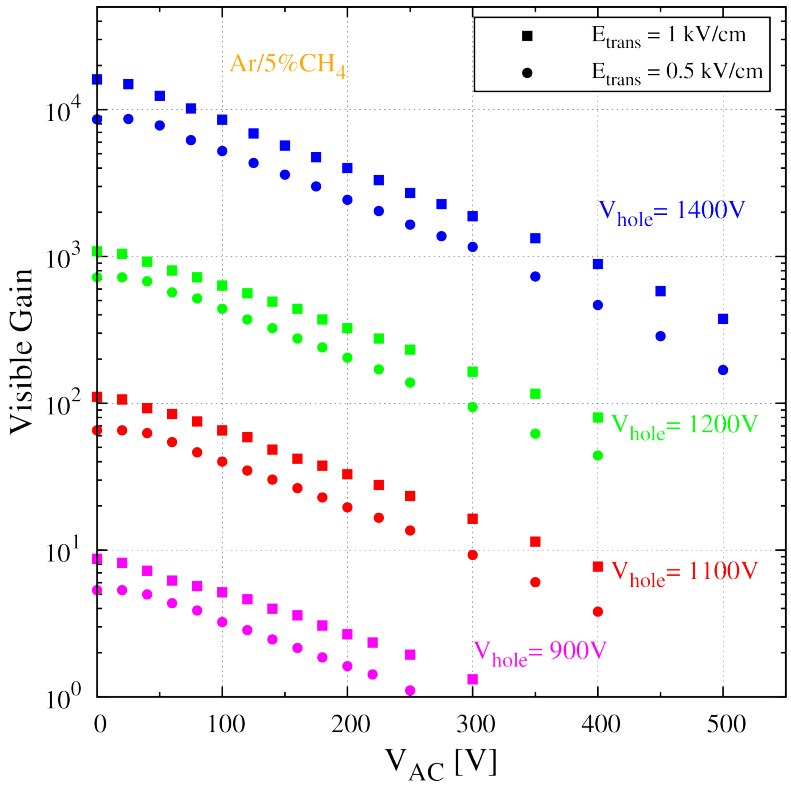

Figure 5.15: R-THCOBRA Visible Gain as a function of V_{CA} for 900 V, 1100 V, 1200 V and 1400 V V_{hole} voltages with transfer fields of 0.5 kV/cm (circles) and 1 kV/cm (squares).

5.2.2 IBF reduction as function of V_{CA}

The R-THCOBRA IBF reduction capability was studied using the setup presented in Figure 5.16: the first element is the R-THCOBRA followed by a THGEM acting as an ion source. We decided to use a THGEM instead a MWPC to act as ion supply in order to guarantee that the produced ions will drift towards the THCOBRA instead of being trapped in the MWPC mesh. Also, the use of a THGEM approaches the design conditions of RICH detectors.

The total electron current in this configuration was measured through the sum of the bottom mesh and bottom THGEM currents (as shown in Figure 5.16) by interconnecting both electrodes.

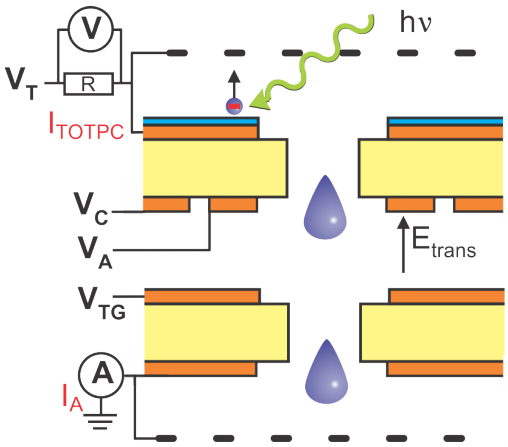

Figure 5.16: The schematic view of the setup used for measuring the ion blocking capability of the R-THCOBRA. Here, the THGEM acts as an ion-supply. The avalanche charge was collected at the interconnected THGEM-bottom and mesh electrodes.

The IBF was calculated as the ratio of the photocathode current under avalanche multiplication, I_{APC} (the ion current that reaches the photocathode) to the total avalanche current I_A (the number of ions produced in the last amplification stage):

$$\mathrm{IBF} = \frac{I_{APC}}{I_A} \tag{5.6}$$

I_{APC} was obtained by subtracting the initial photocathode current, I_{PC0}, to the total photocathode current under multiplication I_{TOTPC}:

$$I_{APC} = I_{TOTPC} - I_{PC0} \tag{5.7}$$

The THGEM element was biased at 1200 V (gain $\sim 10^3$) for two transfer fields: E_{trans}=0.5 kV/cm and E_{trans}=1 kV/cm. The drift field was set to E_{drift}=0 kV/cm by interconnecting the upper mesh and top-THCOBRA electrode. The study was performed for two THCOBRA V_{hole} values: 1100 V (G=10^2) and 1200 V (G=10^3) while varying V_{CA}. When planning the measurements, just two THCOBRA gain values were chosen: 10^2 and 10^3. Those

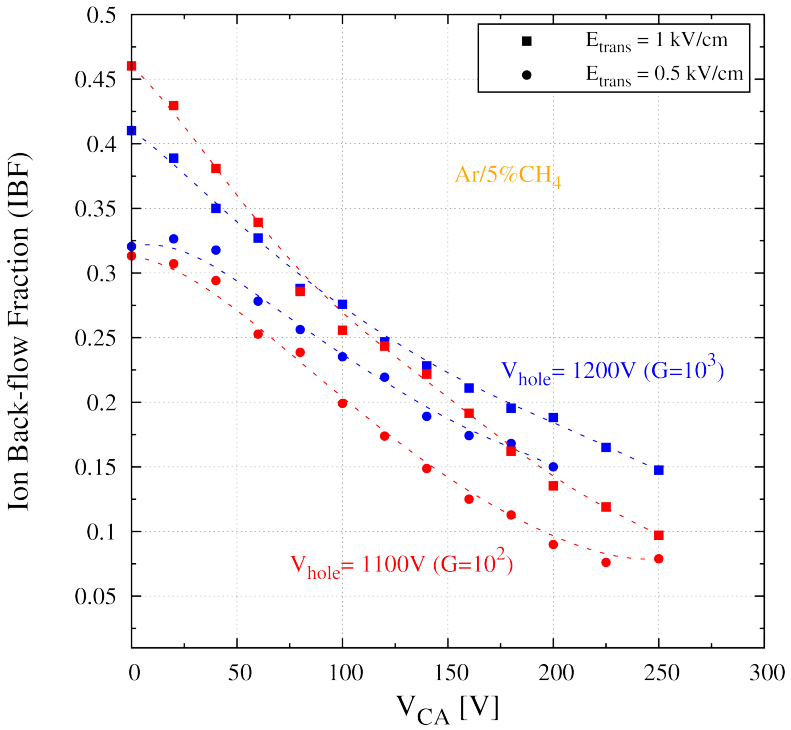

Figure 5.17: IBF as a function of V_{CA} for hole gain of 10^2 (red)and 10^3 (blue) and transfer fields of 0.5 kV/cm (circles) and 1 kV/cm (squares). Dashed lines are guides-to-the-eye.

values are in accordance to the bibliography in IBF reduction [139, 143, 150, 151]: low gain in the first element will have as consequence the loss of events, i.e., the detection efficiency decrease; high gain in the first element will increase the number of ions produced in the first multiplication stage that will drift to the photocathode reducing the IBF detector performance.

5.2.2.1 Results and discussion

Figure 5.17 presents the IBF measurements as a function of V_{CA} for four different conditions by varying the gain and the transfer field. The results show the R-THCOBRA ion back-flow reduction capability: by increasing the voltage across the strips (V_{CA}) the IBF value is reduced showing that the avalanche ions are trapped in the THCOBRA strip electrodes, namely in the cathode.

IBF reduction		Gain (V_{hole})	
		G=10^2 (V_{hole}=1100)	G=10^3 (V_{hole}=1200)
E_{trans}	0.5 kV/cm	3.5	2.4
	1 kV/cm	4.7	2.2

Table 5.2: Estimated IBF reduction by calculating the ratio between the IBF value for V_{CA}=0 V (THGEM mode) and V_{CA}=200 V.

As expected from literature [139, 150, 151] the IBF value is dependent not only on V_{CA} as also on the transfer field. Higher transfer field values will benefit the electron transfer efficiency, but at the same time will increase the ion transfer to the upper stage increasing the IBF value.

The above observations are summarized in Table 5.2, that presents an estimation of the IBF reduction by taking the IBF value for V_{CA}=200 V and comparing it with the value for V_{CA}=0 V (THGEM mode).

From Table 5.2 it is possible to observe that, for the same transfer field, the IBF reduction will degrade with the gain, i.e., the IBF reduction is improved for lower gains.

From Figure 5.17 it is also possible to observe that, the best IBF value achieved (0.1) was reached in the combination V_{hole}=1100 V and E_{trans}=0.5 kV/cm, i.e., the lowest V_{hole} and transfer field.

5.2.3 Single-electron collection efficiency

As mentioned, an important parameter in cascaded detectors applied to single-photon detection is the collection efficiency: the ability of a single element to transfer the event to the next stage [64], previously discussed in section 5.1.4. The collection efficiency should be studied in parallel with IBF as the collection efficiency is expected to change with V_{CA} [150, 154]. Also, it does not make sense to mention IBF reduction in single-photon detectors if the full collection efficiency is not granted, i.e., if the events are lost. It is mandatory to study the system in order to establish working conditions where ε_{coll} is unity and IBF is minimized.

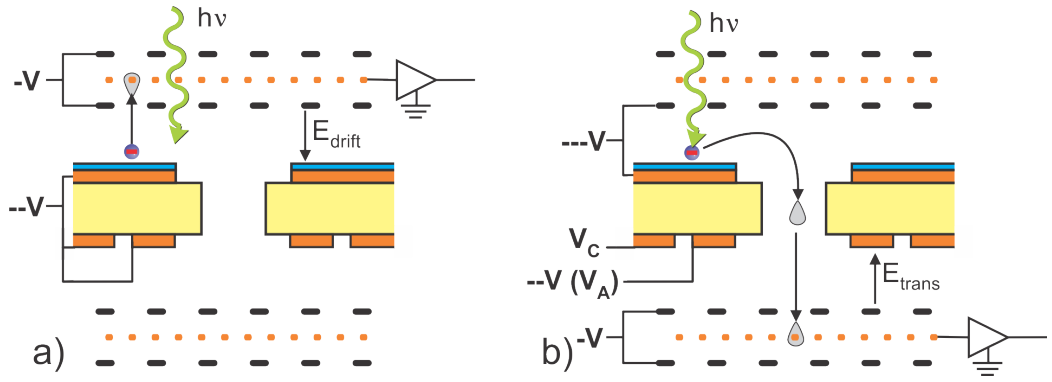

Figure 5.18: Schematic view and electrical bias of the experimental setup for measuring the R-THCOBRA single-electron collection efficiency: a) measurement of the reference pulse-height spectrum with a MWPC reference detector; b) measurement of the pulse-height spectrum of the investigated detector.

The method and measurements scheme (Figure 5.18) are similar to the ones used for THGEM single-photoelectron collection efficiency in section 5.1.4. In this case the measurements will be performed as a function of V_{CA} for different combinations of V_{hole} (1100 V and 1200 V) and fixed transfer fields values (0.5 kV/cm and 1 kV/cm), corresponding to the same conditions of the previous IBF study.

5.2.3.1 Results and discussion

Figure 5.19 presents the results for the single-photoelectron collection efficiency as a function of V_{CA} for a fixed V_{hole} and E_{trans}. In all cases, ε_{coll} loses the unitary value at V_{CA}>50 V. This was an unexpected observation from the analysis of previous results like the visible gain (Figure 5.15). Nevertheless, no conclusions about collection efficiency can be extracted from the visible gain results as they were measured in current mode and thus do not reflect the loss of small amplitude events as explained in section 5.1.4.

The sudden decrease of ε_{coll} with V_{CA} is explained by a distortion in the transfer field. The effect is presented in Figure 5.20 [154], where the simulated ion paths on a FR-THCOBRA operating in Ar are shown.

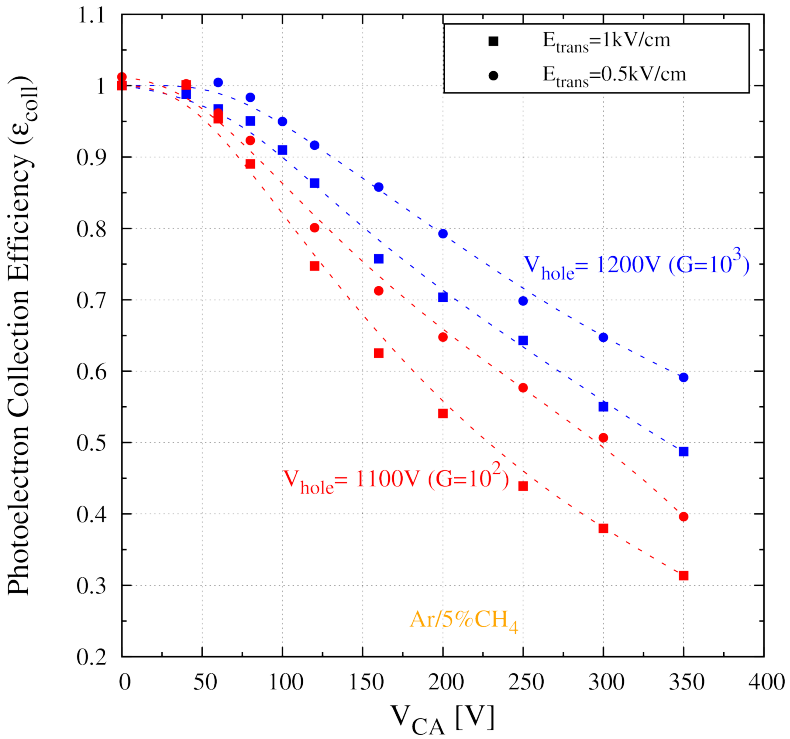

Figure 5.19: R-THCOBRA Single-photoelectron collection efficiency versus the voltage across the strips for V_{hole} of 1100 V (red) and 1200 V (blue) and for transfer fields of 0.5 kV/cm (circles) and 1 kV/cm (squares), in Ar/5%CH_4. Dashed lines are guides-to-the-eyes.

Despite the different THCOBRA and detector geometries used in the simulation, relevant information can be extracted from the figure: as the ions paths are coupled to the electric field lines, we can observe a transfer field-reversing effect by continuously increasing V_{CA}, meaning that the transfer field is influenced by the V_C voltage. Due to distortions in the transfer field and to the high fluctuation in the single-photoelectron multiplication, the degradation of ε_{coll} will be observed due to the loss of transferred events. The probable solution for this effect should be the correction of the E_{trans} when V_{CA} is increased.

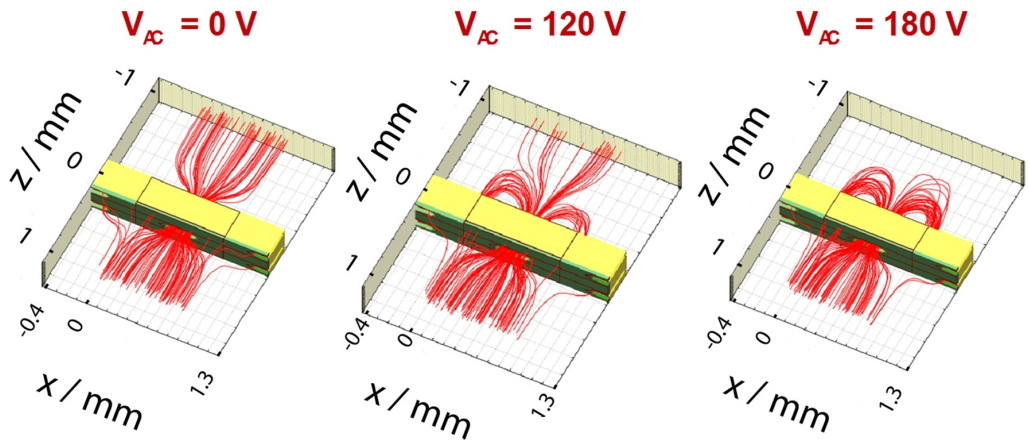

Figure 5.20: Ion drift lines in a FR-THCOBRA for different V_{CA} values. Adapted from [154].

6

General conclusions and future work

The presented work in Ne mixtures focused on the photoelectron extraction and collection efficiencies, showing that practically in all mixtures studied, extraction efficiency $> 72\%$ (assuming 1.5 kV/cm surface electric field) and full collection efficiency may be reached at realistic operation conditions. Effective photon detection efficiency values of 12-14% at 170 nm were calculated with the present THGEM geometry in the gases investigated, at gains $> 10^5$. These values are expected to increase significantly, to about 20-23%, with an optimized hole geometry (larger pitch; smaller rim size), as indicated in the discussion (section 5.1.5) and in Table 5.2.

Therefore, THGEM-based detectors operating in Ne-based mixtures (Ne/CH_4 or Ne/CF_4), may constitute an attractive alternative to current MWPC-based UV photon-imaging detectors for RICH applications. High gains ($>10^5$) were reached in this work in single-THGEM multipliers with Ne mixtures, at low operation voltages, with stable, discharge-free, operation - foreseeing high absolute single-photon detection efficiencies.

The data presented here are with single THGEM elements. An alternative solution would be to use cascaded-THGEMs, that have the advantage of higher gains at lower operating voltages per element, increased stability and reduced ion back-flow [124]. However, the voltage applied on the first THGEM, would have to be optimized so as to maintain the highest possible effective single-photon detection efficiency and low ion back-flow. Large-area

cascaded-THGEM UV-photon detectors with reflective CsI photocathodes would have some advantages over cascaded-GEM's [67, 155]. Besides simplicity and robustness, they have better electron collection and transport between the cascaded elements resulting in a lower gain required per element or, alternatively, fewer cascaded elements for the same total gain [124].

THGEM-based UV detectors are under investigation within the CERN-RD51 collaboration. Similar conclusions were recently reached by other authors [119] while the proof-of-principle of a cascaded Triple-THGEM detector using Ne/10%CH_4 [138] and Ar/30%CO_2 [127] has already been shown in test beam.

Further studies with the "optimal" THGEM will clarify its applicability to photon detectors namely for RICH applications.

Preliminary results in IBF reduction by using a THCOBRA operating in a reversed bias show good potential for its application in cascaded detectors using CsI photocathodes. These preliminary results show an interesting IBF reduction capability that could increase the lifetime of gaseous photomultipliers, such as in RICH detectors, operating at high radiation flux, reducing as well ion induced secondary effects [19, 86, 141].

Although THCOBRA for IBF reduction proof-of-principle has been shown in a reversed-bias configuration, a better performance would be expected by using the flipped geometry [150] being already presented in [154].

Detailed and systematic studies on ε_{coll}, IBF and visible gain are needed, by increasing E_{trans} proportionally to the increase of V_{CA}, for both R-THCOBRA and FR-THCOBRA.

Simulations on THCOBRA geometry (similar to the "optimal" THGEM studies) and detector configuration should be considered in order to maximize the IBF reduction while keeping ε_{coll} unitary.

The implementation of a R-THCOBRA+THGEM and FR-THCOBRA+THGEM or even in triple-structure cascaded configuration should be performed in order to evaluate the THCOBRA IBF reduction capability in real detector working conditions.

Bibliography

[1] J. T. Bushberg et al., "*The essential physics of medical imaging*", Lippincott Williams & Wilkins, 2002.

[2] W. R. Hendee and E. R. Ritenour, "*Medical Imaging Physics*", Wiley-Liss, 2002.

[3] K. Iniewski, "*Medical imaging principles, detectors, and electronics*", John Wiley & Sons, Inc., 2009.

[4] M. I. Lopes and V. Chepel, "*Detectors for medical radioisotope imaging: demands and perspectives*", Radiat. Phys. Chem., vol. 71, no. 3-4, pp. 683 - 692, 2004.

[5] A. Celler, Nuclear Medicine: SPECT and PET Imaging Principles, Chapter 5, pp. 103-126, in *Medical Imaging Principles, Detectors, and Electronics*, John Wiley & Sons, Inc., 2009.

[6] G. F. Knoll, "*Radiation detection and measurement*", John Wiley & Sons, 2000.

[7] A. Passeri and A. R. Formiconi, SPECT and Planar Imaging in Nuclear Medicine, Chapter 7, pp. 235-285, in *Ionizing Radiation Detectors for Medical Imaging*, World Scientific, 2004.

[8] A. D. Guerra and N. Belcari, "*State-of-the-art of PET, SPECT and CT for small animal imaging*", Nucl. Instrum. Meth. A, vol. 583, no. 1, pp. 119 - 124, 2007.

[9] L. Verger et al., "*Characterization of CdTe and CdZnTe detectors for gamma-ray imaging applications*", Nucl. Instrum. Meth. A, vol. 458, no. 1-2, pp. 297 - 309, 2001.

[10] M. Squillante, L. Cirignano and R. Grazioso, "*Room-temperature semiconductor device and array configurations*", Nucl. Instrum. Meth. A, vol. 458, no. 1-2, pp. 288 - 296, 2001.

[11] C. Scheiber and G. C. Giakos, "*Medical applications of CdTe and CdZnTe detectors*", Nucl. Instrum. Meth. A, vol. 458, no. 1-2, pp. 12 - 25, 2001.

[12] E. Bertolucci et al., "*Preliminary test of an imaging probe for nuclear medicine using hybrid pixel detectors*", Nucl. Instrum. Meth. A, vol. 487, no. 1-2, pp. 193 - 201, 2002.

[13] V. Solovov et al., "*Liquid-xenon γ-camera with ionisation readout*", Nucl. Instrum. Meth. A, vol. 478, no. 1-2, pp. 435 - 439, 2002.

[14] V. Egorov et al., "*Electroluminescence emission gamma-camera*", Nucl. Instrum. Meth. A, vol. 205, no. 1-2, pp. 373 - 374, 1983.

[15] H. N. Ngoc et al., "*A xenon high-pressure proportional scintillation-camera for X and γ-ray imaging*", Nucl. Instrum. Meth. A, vol. 172, no. 3, pp. 603 - 608, 1980.

[16] A. Bolozdynya et al., "*A high pressure xenon self-triggered scintillation drift chamber with 3D sensitivity in the range of 20-140 keV deposited energy*", Nucl. Instrum. Meth. A, vol. 385, pp. 225-238, 1997.

[17] C. D. R. Azevedo, "*Desenvolvimento de um Detector de Raios-γ com Vista à Aplicação em Medicina Nuclear*", MSc Thesis, Universidade de Aveiro (Departamento de Física), Aveiro, Portugal, 2007.

[18] E. Aprile et al., "*Noble Gas Detectors*", Wiley-VCH, 2006.

[19] S. D. Torre, "*Status and perspectives of gaseous photon detectors*", Nucl. Instrum. Meth. A, vol. 639, no. 1, pp. 111 - 116, 2011.

[20] E. D. C. Freitas et al., "*Micro-hole and strip plate-based photosensor*", Nucl. Instrum. Meth. A, vol. 580, pp. 214-217, 2007.

[21] C. D. R. Azevedo et al., "*Gas VUV photosensors operating face to face*", Nucl. Instrum. Meth. A, vol. 610, pp. 238-241, 2009.

[22] C. Azevedo et al., "*HpXe gas VUV photosensors operating face-to-face*", In *Nuclear Science Symposium Conference Record, 2008. NSS'08. IEEE*, 2008.

[23] F. D. Amaro et al., "*Operation of MHSP multipliers in high pressure pure noble-gas*", 2006 JINST 1 P04003.

[24] A. Buzulutskov, "*Physics of multi-GEM structures*", Nucl. Instrum. Meth. A, vol. 494, pp. 148-155, 2002.

[25] L. C. C. Coelho et al., "*High-pressure operation of a xenon-GPSC/MSGC hybrid detector for hard X-ray spectrometry*", Nucl. Instrum. Meth. A, vol. 569, pp. 796-802, 2006.

[26] T. Meinschad, L. Ropelewski and F. Sauli, "*Detection of primary and field-enhanced scintillation in xenon with a CsI-coated GEM detector*", Nucl. Instrum. Meth. A, vol. 547, pp. 342-345, 2005.

[27] G. J. Mahler et al., "*A portable gamma-ray spectrometer using compressed xenon*", IEEE Trans. Nucl. Sci., vol. 45, pp. 1029-1033, 1998.

[28] C. D. R. Azevedo et al., "*Development of a HpXe hybrid gamma detector aiming scintigraphy*", In *Nuclear Science Symposium Conference Record, 2007. NSS '07. IEEE*, 2007.

[29] F. D. Amaro et al., "*High Pressure Operation of the Photon-Assisted Cascaded Electron Multiplier*", IEEE Trans. Nucl. Sci., vol. 56, pp. 1097-1101, 2009.

[30] H. N. Luz et al., "*Single Photon Counting X-Ray Imaging System Using a Micro Hole and Strip Plate*", IEEE Trans. Nucl. Sci., vol. 55, pp. 2341-2345, 2008.

[31] F. P. Santos et al., "*3-Dimensional Monte-Carlo Calculation of the Vuv Electroluminescence and Other Electron-Transport Parameters in Xenon*", J. Phys. D, vol. 27, pp. 42-48, 1994.

[32] C. M. B. Monteiro et al., "*Secondary scintillation yield in pure xenon*", 2007 JINST 2 P05001.

[33] C. D. R. Azevedo et al., "*2D-sensitive HpXe gas proportional scintillation counter*", In *Nuclear Science Symposium Conference Record (NSS/MIC), 2009 IEEE*, 2009.

[34] C. D. R. Azevedo et al., "*2D-sensitive hpxe gas proportional scintillation counter concept for nuclear medical imaging purposes*", 2011 JINST 6 C01067.

[35] K. Saito et al., "*Absolute number of scintillation photons emitted by alpha particles in rare gases*", IEEE Trans. Nucl. Sci., vol. 49, pp. 1674-1680, 2002.

[36] M. Heppener, H. Aarts and D. Simons, "*The driftless gas scintillation proportional counter*", Adv. Space Res., vol. 10, no. 2, pp. 317 - 321, 1990.

[37] M. Suzuki and S. Kubota, "*Mechanism of proportional scintillation in argon, krypton and xenon*", Nucl. Instrum. Meth. A, vol. 164, no. 1, pp. 197 - 199, 1979.

[38] J. F. C. A. Veloso et al., "*A microstrip gas chamber as a VUV photosensor for a xenon gas proportional scintillation counter*", IEEE Trans. Nucl. Sci., vol. 43, no. 3, pp. 1232-1236, 1996.

[39] P. C. P. S. Simões et al., "*A new method for pulse analysis of driftless-gas proportional scintillation counters*", Nucl. Instrum. Meth. A, vol. 505, no. 1-2, pp. 247 - 251, 2003.

[40] C. A. B. Oliveira et al., "*Simulation Method for Position and Energy Corrections in Scintillation Detectors*", In *WMISI'07 - Workshop on Medical Instrumentation Signal and Imaging*, 2007.

[41] J. Fraden, "*Handbook of Modern Sensors - Physics, Designs and Applications*", Springer, 2004.

[42] D. Mormann et al., "*Operation principles and properties of the multi-GEM gaseous photomultiplier with reflective photocathode*", Nucl. Instrum. Meth. A, vol. 530, pp. 258-274, 2004.

[43] A. Breskin, "*CsI UV photocathodes: History and mystery*", Nucl. Instrum. Meth. A, vol. 371, pp. 116-136, 1996.

[44] J. Almeida et al., "*Microanalysis surface studies and photoemission properties of CsI photocathodes*", Nucl. Instrum. Meth. A, vol. 367, no. 1-3, pp. 337-341, 1995.

[45] M. A. Nitti et al., "*Progress in the production of CsI and diamond thin film photocathodes*", Nucl. Instrum. Meth. A, vol. 553, no. 1-2, pp. 157-164, 2005.

[46] T. Boutboul et al., "*On the surface morphology of thin alkali halide photocathode films*", Nucl. Instrum. Meth. A, vol. 438, no. 2-3, pp. 409-414, 1999.

[47] M. A. Nitti et al., "*Influence of the film deposition rate and humidity on the properties of thin CsI photocathodes*", Nucl. Instrum. Meth. A, vol. 523, no. 3, pp. 323-333, 2004.

[48] A. Morozov et al., "*Conversion efficiencies of electron beam energy to vacuum ultraviolet light for Ne, Ar, Kr, and Xe excited with continuous electron beams*", J. Appl. Phys., vol. 103, no. 10, pp. 103301, 2008.

[49] A. Breskin et al., "*Advances in gas avalanche photomultipliers*", Nucl. Instrum. Meth. A, vol. 442, no. 1-3, pp. 58-67, 2000.

[50] A. Braem et al., "*The current progress of the ALICE ring Imaging Cherenkov detector*", Nucl. Instrum. Meth. A, vol. 580, pp. 1144-1147, 2007.

[51] P. Abbon et al., "*The COMPASS RICH-1 fast photon detection system*", Nucl. Instrum. Meth. A, vol. 595, pp. 23-26, 2008.

[52] L. Fabbietti et al., "*Photon detection efficiency in the CsI based HADES RICH*", Nucl. Instrum. Meth. A, vol. 502, no. 1, pp. 256 - 260, 2003.

[53] B. Lasiuk et al., "*The STAR-RICH detector*", Nuclear Physics A, vol. 698, pp. 452c-455c, 2002.

[54] Z. Fraenkel et al., "*A hadron blind detector for the PHENIX experiment at RHIC*", Nucl. Instrum. Meth. A, vol. 546, no. 3, pp. 466 - 480, 2005.

[55] J. F. C. A. Veloso et al., "*Energy resolved X-ray fluorescence imaging based on a micropattern gas detector*", Spectrochim. Acta B, vol. 65, pp. 241-247, 2010.

[56] F. Sauli, "*GEM: A new concept for electron amplification in gas detectors*", Nucl. Instrum. Meth. A, vol. 386, pp. 531-534, 1997.

[57] A. Oed, "*Position-Sensitive Detector with Microstrip Anode for Electron Multiplication with Gases*", Nucl. Instrum. Meth. A, vol. 263, pp. 351-359, 1988.

[58] J. P. Cussonneau et al., "*2D localization using resistive strips associated to the Micromegas structure*", Nucl. Instrum. Meth. A, vol. 492, pp. 26-34, 2002.

[59] J. Bateman et al., "*A gas microstrip detector for X-ray imaging with readout of the anode by resistive division*", Nucl. Instrum. Meth. A, vol. 477, no. 1-3, pp. 29 - 36, 2002.

[60] H. N. Luz, "*Development of neutron and X-ray imaging detectors based on MHSP*", PhD Thesis, Universidade de Aveiro (Departamento de Física), Aveiro, Portugal, 2009.

[61] H. N. Luz et al., "*MHSP operation in pure xenon*", Nucl. Instrum. Meth. A, vol. 552, no. 3, pp. 259-262, 2005.

[62] J. F. C. A. Veloso et al., "*High-rate operation of the Micro-Hole and Strip Plate gas detector*", Nucl. Instrum. Meth. A, vol. 580, pp. 362-365, 2007.

[63] J. M. Maia et al., "*Advances in the Micro-Hole & Strip Plate gaseous detector*", Nucl. Instrum. Meth. A, vol. 504, no. 1-3, pp. 364-368, 2003.

[64] C. D. R. Azevedo et al., "*Towards THGEM UV-photon detectors for RICH: on single-photon detection efficiency in Ne/CH_4 and Ne/CF_4*", 2010 JINST 5 P01002.

[65] C. Richter et al., "*On the efficient electron transfer through GEM*", Nucl. Instrum. Meth. A, vol. 478, pp. 538-558, 2002.

[66] L. C. C. Coelho et al., "*Measurement of the photoelectron-collection efficiency in noble gases and methane*", Nucl. Instrum. Meth. A, vol. 581, pp. 190-193, 2007.

[67] A. Breskin, A. Buzulutskov and R. Chechik, "*GEM photomultiplier operation in CF4*", Nucl. Instrum. Meth. A, vol. 483, pp. 670-675, 2002.

[68] A. Buzulutskov et al., "*The GEM photomultiplier operated with noble gas mixtures*", Nucl. Instrum. Meth. A, vol. 443, no. 1, pp. 164 - 180, 2000.

[69] J. Escada et al., "*A Monte Carlo study of backscattering effects in the photoelectron emission from CsI into CH4 and Ar-CH4 mixtures*", 2007 JINST 2 P08001.

[70] J. Escada et al., "*Measurements of photoelectron extraction efficiency from CsI into mixtures of Ne with CH4, CF4, CO2 and N-2*", 2009 JINST 4 P11025.

[71] L. Coelho et al., "*Photoelectron transmission efficiency in Ar-CH4 and Xe-CH4 mixtures: Experimental results*", Nucl. Instrum. Meth. A, vol. 607, no. 3, pp. 587 - 590, 2009.

[72] J. Escada et al., "*A Monte Carlo study of photoelectron extraction efficiency from CsI photocathodes into Xe-CH 4 and Ne-CH 4 mixtures*", J. Phys. D Appl. Phys., vol. 43, no. 6, pp. 065502, 2010.

[73] P. Rachinhas et al., "*Dependence of the photoelectron collection efficiency in noble gases on the incident VUV photon energy*", In *Nuclear Science Symposium Conference Record, 2002 IEEE*, 2002.

[74] A. Bondar et al., "*First results of the two-phase argon avalanche detector performance with CsI photocathode*", Nucl. Instrum. Meth. A, vol. 581, no. 1-2, pp. 241 - 245, 2007.

[75] E. Aprile and T. Doke, "*Liquid xenon detectors for particle physics and astrophysics*", Rev. Mod. Phys., vol. 82, no. 3, pp. 2053-2097, 2010.

[76] E. Aprile et al., "*First Dark Matter Results from the XENON100 Experiment*", Phys. Rev. Lett., vol. 105, no. 13, pp. 131302, 2010.

[77] D. Akimov et al., "*The ZEPLIN-III dark matter detector: Instrument design, manufacture and commissioning*", Astropart. Phys., vol. 27, no. 1, pp. 46 - 60, 2007.

[78] P. Benetti et al., "*First results from a dark matter search with liquid argon at 87 K in the Gran Sasso underground laboratory*", Astropart. Phys., vol. 28, no. 6, pp. 495 - 507, 2008.

[79] J. Díaz et al., "*The NEXT experiment*", Journal of Physics: Conference Series, vol. 179, no. 1, pp. 012005, 2009.

[80] D. Covita et al., "*Photoelectron extraction efficiency from cesium iodide photocathodes in a pressurized atmosphere of argon and xenon up to 10 bar*", Phys. Lett. B, vol. 701, no. 2, pp. 151 - 154, 2011.

[81] B. Singh et al., "*Ageing of CsI thin film photocathodes induced by UV photons*", Nucl. Instrum. Meth. A, vol. 581, no. 3, pp. 651 - 655, 2007.

[82] B. K. Singh et al., "*CsBr and CsI UV photocathodes: new results on quantum efficiency and aging*", Nucl. Instrum. Meth. A, vol. 454, no. 2-3, pp. 364 - 378, 2000.

[83] D. Mormann et al., "*On the efficient operation of a CsI-coated GEM photon detector*", Nucl. Instrum. Meth. A, vol. 471, pp. 333-339, 2001.

[84] G. Malamud et al., "*Quantum Efficiency and Radiation-Resistance of Bulk and Porous Csi Photocathodes in Vacuum and Methane*", Nucl. Instrum. Meth. A, vol. 335, pp. 136-145, 1993.

[85] A. Buzulutskov, A. Breskin and R. Chechik, "*Field enhancement of the photoelectric and secondary electron emission from CsI*", J. Appl. Phys., vol. 77, no. 5, pp. 2138-2145, 1995.

[86] A. F. Buzulutskov, "*Gaseous Photodetectors with Solid Photocathodes*", Physics of Particles and Nuclei, vol. 39, pp. 424-453, 2008.

[87] T. Boutboul et al., "*An improved model for ultraviolet- and x-ray-induced electron emission from CsI*", J. Appl. Phys., vol. 86, no. 10, pp. 5841-5849, 1999.

[88] T. H. V. T. Dias et al., "*The transmission of photoelectrons emitted from CsI photocathodes into Xe, Ar, Ne and their mixtures: a Monte Carlo study of the dependence on E/N and incident VUV photon energy*", vol. 37, pp. 540-549, 2004.

[89] A. DiMauro et al., "*Photoelectron backscattering effects in photoemission from CsI into gas media*", Nucl. Instrum. Meth. A, vol. 371, pp. 137-142, 1996.

[90] T. H. V. T. Dias et al., "*Monte-Carlo Simulation of X-Ray-Absorption and Electron-Drift in Gaseous Xenon*", Phys. Rev. A, vol. 48, pp. 2887-2902, 1993.

[91] V. T. Jordanov and G. F. Knoll, "*Digital synthesis of pulse shapes in real time for high resolution radiation spectroscopy*", Nucl. Instrum. Meth. A, vol. 345, no. 2, pp. 337 - 345, 1994.

[92] D. S. Covita et al., "*The X-ray performance of a driftless gas proportional scintillation counter using short shaping-time constants for pulse analysis*", Nucl. Instrum. Meth. A, vol. 516, no. 1, pp. 134 - 142, 2004.

[93] R. A. Austin et al., "*A high-pressure gas-scintillation-proportional counter for the focus of a hard-x-ray telescope*", Proc. SPIE, vol. 3765, pp. 714-720, 1999.

[94] C. A. N. Conde and A. J. P. L. Policarpo, "*A gas proportional scintillation counter*", Nucl. Instrum. Meth. A, vol. 53, pp. 7-12, 1967.

[95] J. M. F. Dos Santos et al., "*The Performance of a Compact Gas Proportional Scintillation-Counter for Hard X-Ray Spectrometry*", Nucl Instrum Meth A, vol. 353, no. 1-3, pp. 195-200, 1994.

[96] W. R. Hendee and E. R. Ritenour, ANALYTIC DESCRIPTION OF IMAGE QUALITY, Chapter 17, pp. 281-286, in *Medical Imaging Physics*, Wiley-Liss, 2002.

[97] S. W. Smith, Special Imaging Techniques, Chapter 25, pp. 423-429, in *The Scientist and Engineer's Guide to Digital Signal Processing*, Elsevier Science, 1999.

[98] J. T. Bushberg et al., Spatial Resolution, Chapter 10.2, pp. 263-273, in *The Essential Physics of Medical Imaging*, Lippincott Williams & Wilkins, 2002.

[99] M. Cortesi et al., "*Investigations of a THGEM-based imaging detector*", 2007 JINST 2 P09002.

[100] J. Lehr, J. B. Sibarita and J. M. Chassery, "*Image restoration in X-ray microscopy: PSF determination and biological applications*", IEEE Trans. Image Process., vol. 7, no. 2, pp. 258 -263, 1998.

[101] A. I. Bolozdynya and V. L. Morgunov, "*Multilayer Electroluminescence Camera: Concept and Monte Carlos Study*", IEEE Trans. Nucl. Sci., vol. 45, pp. 1646-1655, 1998.

[102] G. C. Smith, J. Fischer and V. Radeka, "*Photoelectron Range Limitations to the Spatial Resolution for X-Rays in Gas Proportional Chambers*", IEEE Trans. Nucl. Sci., vol. 31, no. 1, pp. 111 -115, 1984.

[103] L. Shekhtman, "*Novel position-sensitive gaseous detectors for X-ray imaging*", Nucl. Instrum. Meth. A, vol. 522, no. 1-2, pp. 85 - 92, 2004.

[104] J. Fischer, V. Radeka and G. Smith, "*X-ray position detection in the region of 6 [mu]m RMS with wire proportional chambers*", Nucl. Instrum. Meth. A, vol. 252, no. 2-3, pp. 239 - 245, 1986.

[105] T. J. Shin, S. B. Dierker and G. C. Smith, "*Two-dimensional multiwire gas proportional detector for X-ray photon correlation spectroscopy of condensed matter*", Nucl. Instrum. Meth. A, vol. 587, no. 2-3, pp. 434 - 440, 2008.

[106] M. Cortesi et al., "*THGEM operation in Ne and Ne/CH4*", 2009 JINST 4 P08001.

[107] S. N. Ahmed, "*Physics and Engineering of Radiation Detection*", Elsevier, 2007.

[108] A. Das and T. Ferbel, "*Introduction to Nuclear and Particle Physics*", World Scientific Publishing, 2003.

[109] W. R. Leo, "*Techniques for Nuclear and Particle Physics Experiments*", Springer-Verlag, 1987.

[110] B. B. Govorkov, "*Cherenkov detectors in Cherenkov's laboratory*", Nucl. Instrum. Meth. A, vol. 553, no. 1-2, pp. 9 - 17, 2005.

[111] J. Seguinot and T. Ypsilantis, "*Photo-ionization and Cherenkov ring imaging*", Nucl. Instrum. Meth. A, vol. 142, no. 3, pp. 377 - 391, 1977.

[112] T. Ypsilantis and J. Seguinot, "*Theory of ring imaging Cherenkov counters*", Nucl. Instrum. Meth. A, vol. 343, no. 1, pp. 30 - 51, 1994.

[113] P. Abbon et al., "*Particle identification with COMPASS RICH-1*", Nucl. Instrum. Meth. A, vol. 631, no. 1, pp. 26 - 39, 2011.

[114] J. Seguinot and T. Ypsilantis, "*A historical survey of ring imaging Cherenkov counters*", Nucl. Instrum. Meth. A, vol. 343, no. 1, pp. 1 - 29, 1994.

[115] I. Tserruya, "*Cherenkov counters in heavy-ion physics*", Nucl. Instrum. Meth. A, vol. 553, no. 1-2, pp. 196 - 204, 2005.

[116] E. Nappi, "*CsI RICH detectors in high energy physics experiments*", Nucl. Instrum. Meth. A, vol. 471, no. 1-2, pp. 18 - 24, 2001.

[117] A. Braem et al., "*Results from the ageing studies of large CsI photocathodes exposed to ionizing radiation in a gaseous RICH detector*", Nucl. Instrum. Meth. A, vol. 553, no. 1-2, pp. 187 - 195, 2005.

[118] M. Alexeev et al., "*The quest for a third generation of gaseous photon detectors for Cherenkov imaging counters*", Nucl. Instrum. Meth. A, vol. In press, 2009.

[119] V. Peskov et al., "*Further evaluation of a THGEM UV-photon detector for RICH - comparison with MWPC*", 2010 JINST 5 P11004.

[120] E. Albrecht et al., "*Status and characterisation of COMPASS RICH-1*", Nucl. Instrum. Meth. A, vol. 553, no. 1-2, pp. 215 - 219, 2005.

[121] E. Nappi, "*Advances in the photodetection technologies for Cherenkov imaging applications*", Nucl. Instrum. Meth. A, vol. 604, no. 1-2, pp. 190 - 192, 2009.

[122] R. Chechik et al., "*Thick GEM-like hole multipliers: properties and possible applications*", Nucl. Instrum. Meth. A, vol. 535, pp. 303-308, 2004.

[123] C. Shalem et al., "*Advances in Thick GEM-like gaseous electron multipliers - Part I: atmospheric pressure operation*", Nucl. Instrum. Meth. A, vol. 558, pp. 475-489, 2006.

[124] A. Breskin et al., "*A concise review on THGEM detectors*", Nucl. Instrum. Meth. A, vol. 598, pp. 107-111, 2009.

[125] R. Chechik, A. Breskin and C. Shalem, "*Thick GEM-like multipliers - a simple solution for large area UV-RICH detectors*", Nucl. Instrum. Meth. A, vol. 553, pp. 35-40, 2005.

[126] R. Alon et al., "*Time resolution of a Thick Gas Electron Multiplier (THGEM)-based detector*", 2008 JINST 3 P11001.

[127] M. Alexeev et al., "*Progress towards a THGEM-based detector of single photons*", Nucl. Instrum. Meth. A, vol. 639, no. 1, pp. 130 - 133, 2011.

[128] A. Di Mauro, "*Recent CsI-RICH developments*", Nucl. Instrum. Meth. A, vol. 525, no. 1-2, pp. 173 - 177, 2004.

[129] R. Alon et al., "*Operation of a thick gas electron multiplier (THGEM) in Ar, Xe and Ar-Xe*", 2008 JINST 3 P01005.

[130] V. Peskov et al., "*Progress in the development of photosensitive GEMs with resistive electrodes manufactured by a screen printing technology*", Nucl. Instrum. Meth. A, vol. In press, 2009.

[131] L. Periale et al., "*Detection of the primary scintillation light from dense Ar, Kr and Xe with novel photosensitive gaseous detectors*", Nucl. Instrum. Meth. A, vol. 478, pp. 377-383, 2002.

[132] M. Alexeev et al., "*Development of THGEM-based photon detectors for Cherenkov Imaging Counters*", JINST, vol. 5, no. 03, pp. P03009, 2010.

[133] R. Oliveira et al., "*First tests of thick GEMs with electrodes made of a resistive kapton*", Nucl. Instrum. Meth. A, vol. 576, pp. 362-366, 2007.

[134] D. Mormann, "*Study of novel gaseous photomultipliers for UV and visible light*", PhD Thesis, Weizmann Institute of Science, Rehovot, Israel, 2005.

[135] MAXWELL 3D, ANSOFT Co, Pittsburgh, PA, U.S.A.

[136] S. D. Torre, Private communication.

[137] Abraham and Gallas, "*Experience from the construction and installation of the HMPID CsI-RICH detector in ALICE*", Nucl. Instrum. Meth. A, vol. 581, no. 1-2, pp. 402 - 405, 2007.

[138] P. Martinengo et al., "*R&D results on a CsI-coated triple thick GEM-based photodetector*", Nucl. Instrum. Meth. A, vol. 639, no. 1, pp. 126 - 129, 2011.

[139] A. V. Lyashenko et al., "*Advances in ion back-flow reduction in cascaded gaseous electron multipliers incorporating R-MHSP elements*", JINST, vol. 1, no. 10, pp. P10004, 2006.

[140] A. Buzulutskov et al., "*Further studies of the GEM photomultiplier*", Nucl. Instrum. Meth. A, vol. 442, no. 1-3, pp. 68 - 73, 2000.

[141] A. Breskin et al., "*Sealed GEM photomultiplier with a CsI photocathode: ion feedback and ageing*", Nucl. Instrum. Meth. A, vol. 478, no. 1-2, pp. 225 - 229, 2002.

[142] A. Breskin et al., "*Ion-induced effects in GEM and GEM/MHSP gaseous photomultipliers for the UV and the visible spectral range*", Nucl. Instrum. Meth. A, vol. 553, pp. 46-52, 2005.

[143] J. M. Maia et al., "*Avalanche-ion back-flow reduction in gaseous electron multipliers based on GEM/MHSP*", Nucl. Instrum. Meth. A, vol. 523, no. 3, pp. 334 - 344, 2004.

[144] D. Friedrich et al., "*Positive ion effects in large-volume drift chambers*", Nucl. Instrum. Meth. A, vol. 158, pp. 81 - 88, 1979.

[145] D. Mormann et al., "*Evaluation and reduction of ion back-flow in multi-GEM detectors*", Nucl. Instrum. Meth. A, vol. 516, no. 2-3, pp. 315 - 326, 2004.

[146] A. Bondar et al., "*Study of ion feedback in multi-GEM structures*", Nucl. Instrum. Meth. A, vol. 496, no. 2-3, pp. 325 - 332, 2003.

[147] R. Chechik and A. Breskin, "*Advances in gaseous photomultipliers*", Nucl. Instrum. Meth. A, vol. 595, no. 1, pp. 116 - 127, 2008.

[148] M. Balcerzyk et al., "*Methods of preparation and performance of sealed gas photomultipliers for visible light*", IEEE Trans. Nucl. Sci., vol. 50, no. 4, pp. 847 - 854, 2003.

[149] J. Veloso et al., "*MHSP in reversed-bias operation mode for ion blocking in gas-avalanche multipliers*", Nucl. Instrum. Meth. A, vol. 548, no. 3, pp. 375 - 382, 2005.

[150] A. V. Lyashenko et al., "*Further progress in ion back-flow reduction with patterned gaseous hole-multipliers*", 2007 JINST 2 P08004.

[151] A. Lyashenko et al., "*Efficient ion blocking in gaseous detectors and its application to gas-avalanche photomultipliers sensitive in the visible-light range*", Nucl. Instrum. Meth. A, vol. 598, no. 1, pp. 116 - 120, 2009.

[152] J. F. C. A. Veloso et al., "*PACEM: a new concept for high avalanche-ion blocking*", Nucl. Instrum. Meth. A, vol. 581, pp. 261-264, 2007.

[153] F. D. Amaro et al., "*The Thick-COBRA: a new gaseous electron multiplier for radiation detectors*", 2010 JINST 5 P10002.

[154] J. Veloso et al., "*THCOBRA: Ion back flow reduction in patterned THGEM cascades*", Nucl. Instrum. Meth. A, vol. 639, no. 1, pp. 134 - 136, 2011.

[155] C. Aidala et al., "*A Hadron Blind Detector for PHENIX*", Nucl. Instrum. Meth. A, vol. 502, pp. 200-204, 2003.